MINISTRY OF EDUCATION

THE ANNALS OF "DUNAREA DE JOS" UNIVERSITY OF GALATI

Fascicle IX
METALLURGY AND MATERIALS SCIENCE

YEAR XXXIX (XLIV)
March 2021, no. 1

ISSN 2668-4748; e-ISSN 2668-4756

2021
GALATI UNIVERSITY PRESS

EDITORIAL BOARD

THE ANNALS OF "DUNAREA DE JOS" UNIVERSITY OF GALATI
FASCICLE IX. METALLURGY AND MATERIALS SCIENCE
Nº. 1 - 2021, ISSN 2668-4748; e-ISSN 2668-4756
Volume DOI: https://doi.org/10.35219/mms.2021.1

Table of Contents

THE ANNALS OF "DUNAREA DE JOS" UNIVERSITY OF GALATI
FASCICLE IX. METALLURGY AND MATERIALS SCIENCE
Nº. 1 - 2021, ISSN 2668-4748; e-ISSN 2668-4756
Volume DOI: https://doi.org/10.35219/mms.2021.1

THE ANNALS OF "DUNAREA DE JOS" UNIVERSITY OF GALATI
FASCICLE IX. METALLURGY AND MATERIALS SCIENCE
No. 1 - 2021, ISSN 2668-4748; e-ISSN 2668-4756
Article DOI: https://doi.org/10.35219/mms.2021.1.01

STRUCTURAL EFFECTS OF HEAT TREATMENT HOLDING-TIME ON DYNAMIC AND DAMPING BEHAVIOUR OF AN Fe-28Mn-6Si-5Cr SHAPE MEMORY ALLOY

Mihai POPA[1], Bogdan PRICOP[1], Bogdan ISTRATE[2], Florin POPA[3], Viorel GOANȚĂ[2], Leandru Gheorghe BUJOREANU[1]*

[1]"Gheorghe Asachi" Technical University of Iași, Faculty of Materials Science and Engineering, Blvd. Dimitrie Mangeron 61A, 700050 Iași, Romania

[2]"Gheorghe Asachi" Technical University of Iași, Faculty of Mechanical Engineering, Blvd. Dimitrie Mangeron 61-63, 700050 Iași, Romania

[3]Technical University of Cluj-Napoca, Faculty of Materials and Environmental Engineering, 400461 Cluj-Napoca, Romania

*e-mail: leandru-gheorghe.bujoreanu@academic.tuiasi.ro

ABSTRACT

The paper reports the structural effects of holding time period, during heat treatment, on the dynamic and damping behavior of a Fe-28Mn-6Si-5Cr (mass. %) shape memory alloy. After casting and hot rolling, solution treatment at 1050 °C was applied for five holding times, 2, 4, 6, 8 and 10 hours, followed by water quenching. The specimens were analyzed by scanning electron microscopy and X-ray diffraction which emphasized that only the 2-hours solution treated specimens contained ε-hexagonal close packed (hcp) martensite and experienced the highest internal friction value. These specimens were tested on a special device which transformed both tension and compression into tensile strain applied to the specimens and proved to be a promising solution for anti-seismic damper.

KEYWORDS: FeMnSiCr shape memory alloys, martensite, strain sweep dynamic mechanical analysis, internal friction, anti-seismic damper

1. Introduction

Fe-based shape memory alloys (SMAs) are less expensive [1], can develop higher recovery stresses [2] by constrained recovery shape memory effect (SME) [3] and are more easily processable [4] as compared to well-known NiTi SMAs, while achieving comparable corrosion resistance [5]. Polycrystalline Fe-(28-34)Mn-(4-6.5)Si (mass. %, as all chemical compositions will be listed hereinafter) SMAs were reported ever since 1987 as experiencing an almost perfect SME [6].

The microstructural phenomenon that governs SME is the reversion of ε-hexagonal close-packed (hcp) stress induced martensite to γ-face centered cubic (fcc) austenite, during heating [7]. Besides ε-hcp, a (body centered cubic, bcc) martensite, designated as α', can be thermally induced at low Mn contents [8] or stress induced at high deformation levels [9]. The common conviction is that α' bcc martensite delays the reverse martensitic transformation ε-hcp → γ-fcc, which diminishes SME magnitude in Fe-Mn-Si-based [10]. The most popular commercial applications of these alloys comprise: lock rings for bicycle frame pipes [11], pipe coupling rings [12], crane rail fasteners [13], concrete pre-straining rods [14], embedded stripes for concrete beam curvature control [15], anti-seismic dampers for very tall buildings [16].

It is one special grade of commercial use, Fe-28Mn-6Si-5Cr [17], that has been mainly used in vibration mitigation applications [18], as it belongs to the inter-phase boundary type high-damping materials, in which internal friction (IF) is caused by the hysteretic movement of interfaces during the stress induced transformations [19]. Since both SME and IF are based on the reverse movement of γ/ε interface [7], the relationship between these two phenomena, on one hand and stress-induced formation of ε-hcp martensite from γ-fcc austenite, on the other hand, has been intensely studied, in Fe-Mn based SMAs [20].

In a previous paper, a preliminary evaluation of holding time effects, during solution treatment, was

THE ANNALS OF "DUNAREA DE JOS" UNIVERSITY OF GALATI
FASCICLE IX. METALLURGY AND MATERIALS SCIENCE
Nº. 1 - 2021, ISSN 2668-4748; e-ISSN 2668-4756
Article DOI: https://doi.org/10.35219/mms.2021.1.01

performed and an exothermic precipitation phenomenon was observed around 500 ºC, especially after long holding periods. In addition, dynamic strain sweeps, performed by three-point-bending, caused fine shearing of martensite bands, associated with a noticeable decrease of internal friction [21].

The present paper aims to further investigate the connection between holding periods and dynamic and damping behavior of a Fe-28Mn-6Si-5Cr SMA, which will be tested on an experimental anti-seismic damper.

2. Experimental procedure

An Fe-28Mn-6Si-5Cr SMA alloy was melt in a levitation induction furnace, cast into ingots, longitudinally cut by wire spark erosion, hot rolled (1050 ºC) and solution treated at 1050 ºC for five holding times: 2, 4, 6, 8 and 10 h, with final water quenching.

Different specimens were cut with rectangular (4 × 25 mm) and "dog-bone" (4 × 30 mm-gauge) geometries. The former was used for dynamic mechanical analysis (DMA) and structural investigations while the latter was used for damping tests on an anti-seismic damper.

DMA was performed, during five cycles, in the three-point-bending strain sweep mode (DMA-SS-3PB), by means of DMA 242 Artemis NETZSCH device, using a frequency of 1 Hz and a strain amplitude increasing between 0.01 and 0.09 %. Considering that the first cycle usually corresponds to a transient phenomenon, it was removed from the diagrams and an averaging was performed, by PROTEUS software the DMA device has been equipped with.

The structural effects were examined using an Expert PRO MPD diffractometer with Cu Kα radiation and a scanning electron microscope (SEM) JEOL JSM-5600LV device, equipped with an Oxford Instruments EDX (Energy dispersive X-ray spectrometry) detector (INCA 200 software). XRD patterns were recorded on the significance region 2θ = 40-100°. XRD maxima identification of γ-fcc, ε-hcp and α′-bcc phases was done using crystallographic databases 01-071-8288, 01-071-8285 and 00-034-0396, respectively. SEM micrographs were recorded on specimens etched with a solution of 1.2% $K_2S_2O_5$+1% NH_4HF_2 in 100 mL distilled water.

In order to test the damping behavior of differently processed Fe-28Mn-6Si-5Cr SMA specimens, a special anti-seismic damper was designed and manufactured, based on a concept developed by Dolce *et al.* In Figure 1(a) the functioning principle of Dolce's damper is illustrated. It shows that, both during assembly's elongation and compression, the two specimens, fastened between the two transversal rods, are subjected to tensile strains. Considering that Dolce's damper was designed for NiTi wires [22], with small mechanical hysteresis, meant to dissipate seismic energy, the device was adapted for an even number of flat "dog-bone" specimens that have larger mechanical hysteresis (therefore are able to dissipate larger amounts of energy). In addition, Fe-28Mn-6Si-5Cr SMA experienced an excellent low-cycle fatigue life, exceeding 28,000 cycles at a tensile dynamic stress of 773 ± 193 MPa [23].

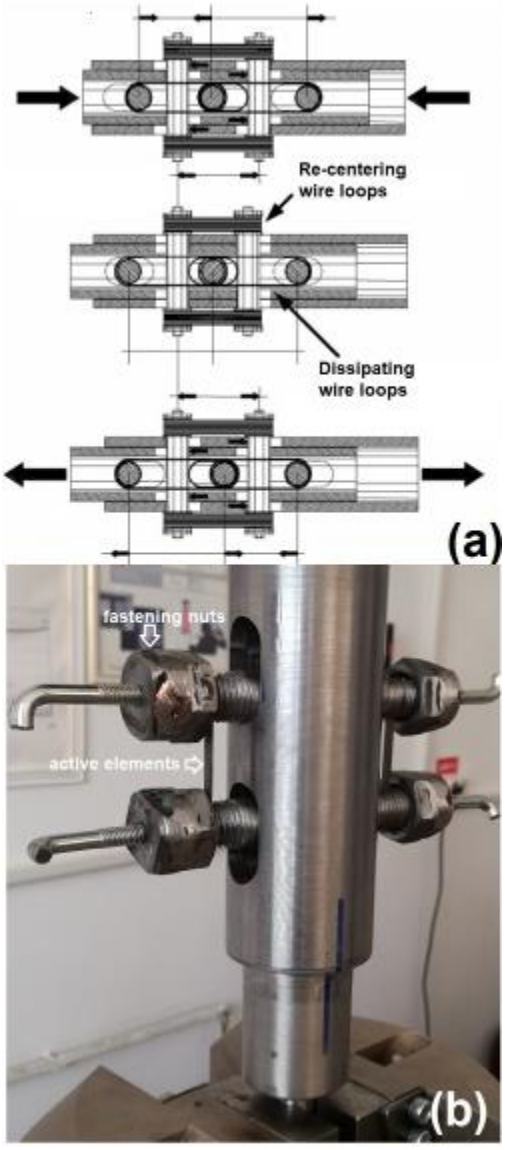

Fig. 1. *Experimental setup for testing anti-seismic damping capacity. (a) functioning scheme of a complete device developed by Dolce et al.* [22]*; (b) prototype of re-centering anti-seismic damper using 2 flat specimens instead of wire loops*

THE ANNALS OF "DUNAREA DE JOS" UNIVERSITY OF GALATI
FASCICLE IX. METALLURGY AND MATERIALS SCIENCE
N°. 1 - 2021, ISSN 2668-4748; e-ISSN 2668-4756
Article DOI: https://doi.org/10.35219/mms.2021.1.01

Figure 1 illustrates both the functioning principle of Dolce's damper that converts either tensile or compressive external solicitations into tensile stresses, or the experimental device, itself, where flat "dog-bone" specimens, representing the active elements, are fixed into the transversal rods, by means of fastening nuts. For damping tests performance, the anti-seismic damper, with a couple of "dog bone" specimens, was fastened in an INSTRON 8801 testing machine and subjected to tension-compression tests, with a frequency of 1 Hz, up to three maximum forces: 3 kN, 4.4 kN and 5.8 kN.

Couples of "dog-bone" specimens were fastened within the experimental anti-seismic damper and subjected to dynamic tensile-compressive cycles, at the frequency of 1 Hz, which is characteristic to earthquakes.

On the recorded strains-stress curves, the area between loading and unloading curves was calculated for each dynamic cycle and, since it represents mechanical hysteresis, was plotted against the number of cycles and maximum applied force.

3. Experimental results and discussion

In order to discuss the effects of solution treatment time on the dynamic response of heat-treated specimens, the DMA-SS-3PB strain sweep diagrams, illustrating the variations of internal friction with strain amplitude, recorded with the frequency of 1 Hz, were summarized in Figure 2.

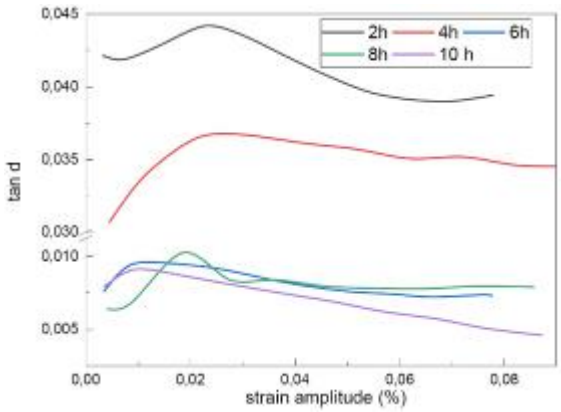

Fig. 2. *Strain sweeps three-point-bending DMA diagrams illustrating the variation of average values of internal friction (tan d) with strain amplitude for specimens solution treated for different holding periods*

It is noticeable that internal friction (tan d) is only slightly influenced by strain amplitude increase for all the specimens. In addition, the specimens solution treated for 2 and 4 hours experienced the largest tan d values, reaching almost 0.045. Another important point is that the specimens that were solution treated for 6, 8 and 10 hours experience very low values of internal friction, typically less than 0.01. It is obvious that the solution treatments for 2 and 4 hours caused different structural changes as compared to those applied for 6, 8 and10 hours. It follows that solution treatment for 2 and 4 hours caused microstructures that enable high mobility of the interfaces while the three others did not. These results recommended the use of specimens solution treated with 2 h-holding at 1050 °C for further experiments.

In order to identify the particularities of the structure of these specimens, XRD patterns were recorded, as summarized in Figure 3. The specimens solution treated for 2 hours had different structure, as compared to the other ones. Phase indexing was performed based on the crystallographic databases and the results are displayed in Figure 3. The specimen solution treated for 2 hours contains ε-hcp martensite, under the form of (101) variant. The rest of the structure comprises small amounts of α'-bcc martensite plate variants.

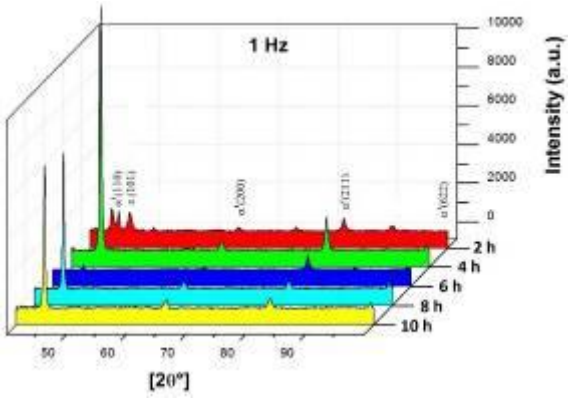

Fig. 3. *XRD patterns of Fe-28Mn-6Si-5Cr SMA specimens solution treated at 1050 °C for different holding periods*

The low values of internal friction can be associated with the presence of at several martensite plate variants of α'-bcc martensite, namely (110), (200), (211) and (622). The high mobility of the interfaces of ε-hcp martensite causes elevated mean values of internal friction, as reported by Chung et al. [24]. The typical morphology of ε-hcp martensite is shown by the SEM in Figure 4.

ε-hcp martensite is very narrow and long and develop the so-called "triangular morphology" due to the orientation along <111>γ close-packed planes.

Three couples of specimens solution treated for 2 hours were tested by means of the anti-seismic

THE ANNALS OF "DUNAREA DE JOS" UNIVERSITY OF GALATI
FASCICLE IX. METALLURGY AND MATERIALS SCIENCE
Nº. 1 - 2021, ISSN 2668-4748; e-ISSN 2668-4756
Article DOI: https://doi.org/10.35219/mms.2021.1.01

damper, subjected to tension-compression cycles at the frequency of 1 Hz. Each couple was tested up to different maximum forces. The stress-strain diagrams are shown in Figure 5.

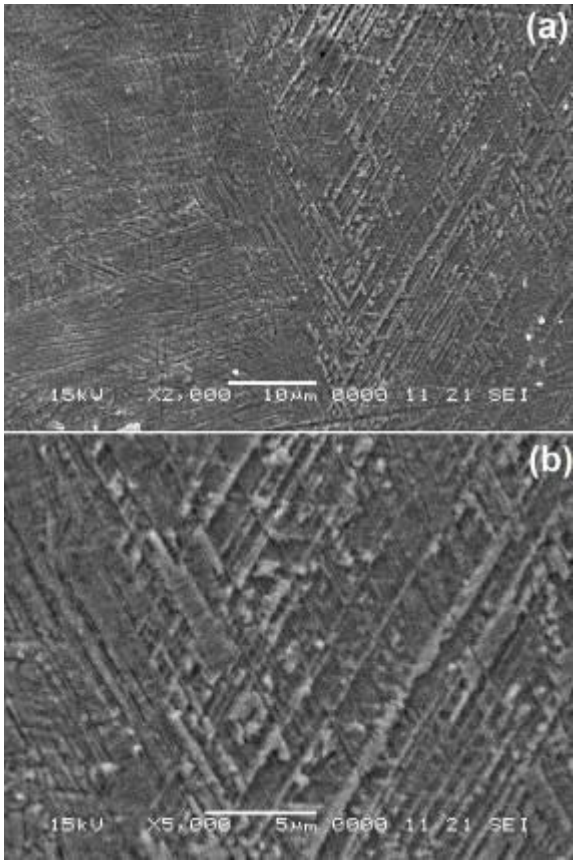

Fig. 4. *SEM micrographs of Fe-28Mn-6Si-5Cr SMA specimens solution treated at 1050 °C for 2 hours: (a) general aspect; (b) detail of ε-hcp martensite plates with triangular morphology*

It is obvious that both strain and stress increased with the maximum applied force. During dynamic testing, the specimens became more and more elongated, but strain increase/ cycle diminished with increasing the number of cycles. Unlike DMA-SS-3PB tests, the largest amount of energy was absorbed during the first cycle, so it was considered for damping analysis. Since internal friction is proportional with mechanical hysteresis, the area between loading and unloading portions of the curves can determine the amount of absorbed energy. These values, determined by integration, are summarized in Figure 6.

The largest amount of energy, over 108 mJ/mm^3, was absorbed in the first cycle applied up to 5.8 kN. Subsequently, the amount of absorbed energy became less and less, thus that in the fifth cycle the three couple of specimens experienced similar damping behaviors.

The anti-seismic damper was tested up to 4 kN for a number of 40,000 cycles, which would correspond to an earthquake lasting for more than 11 hours (at 1 Hz frequency). Figure 7 shows the load-displacement curves of the last cycles.

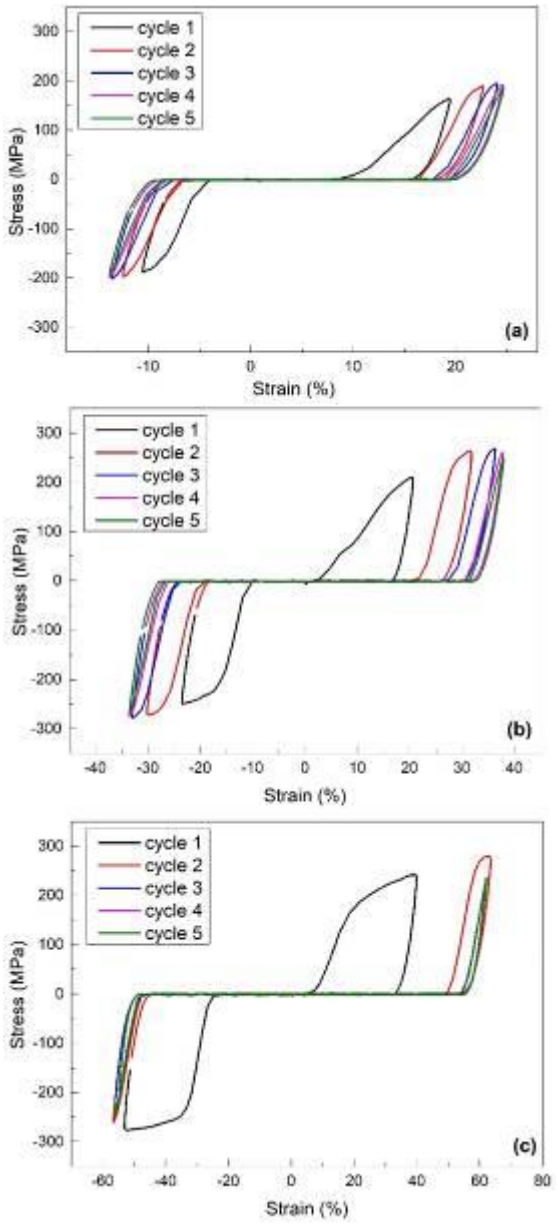

Fig. 5. *Stress-strain curves recorded by the tensile testing machine during elongation-compression tests of two Fe-28Mn-6Si-5Cr SMA specimens solution treated at 1050 °C for 2 hours, fastened on the anti-seismic damper, from Figure 1. Each couple of specimens was tested at 1 Hz for different maximum forces: (a) 3 kN; (b) 4.4 kN; (c) 5.8 kN*

THE ANNALS OF "DUNAREA DE JOS" UNIVERSITY OF GALATI
FASCICLE IX. METALLURGY AND MATERIALS SCIENCE
Nº. 1 - 2021, ISSN 2668-4748; e-ISSN 2668-4756
Article DOI: https://doi.org/10.35219/mms.2021.1.01

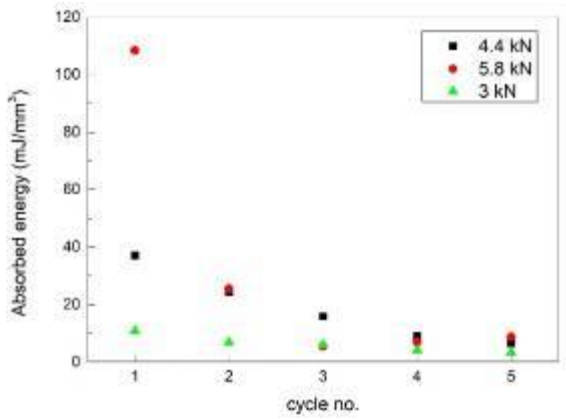

Fig. 6. *Variation of absorbed energy during the first five elongation-compression cycles illustrated in Figure 5*

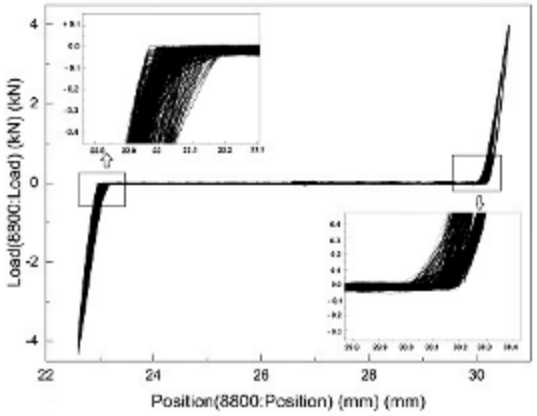

Fig. 7. *Load-displacement records during the last part of 40,000 cycles, up to 4 kN, with details of the beginning and the end of load plateaus*

As expected, the curves resemble those of the fifth cycles from Figure 5. The magnified details of the two ends of the load plateau show that mechanical hysteresis was reduced due to the initial elongation of the specimens. In addition, if an elongated couple of specimens is tested for the second time, no differences were noticed between the first, the tenth and the hundredth cycles.

4. Conclusions

The results have shown that Fe-28Mn-6Si-5Cr SMA experienced internal friction as high as 0.045, determined by DMA-SS-3PB after solution treatment for 2 hours at 1050 ºC. This behavior was associated, by means of XRD pattern, with the presence of ε-hcp martensite, which has, on SEM micrographs, a morphology consisting of long narrow plate variants which enable their reversible movement during stress induced martensitic transformation. These couples of specimens were tested on an anti-seismic damper and three main results were obtained:

(1) over 108 mJ/mm^3 were absorbed, in the first cycle, applied up to 5.8 kN;

(2) up to 40,000 cycles were applied at a maximum force of 4 kN;

(3) once elongated, the specimens do not develop additional strains, in a new test, in such a way that their stress-strain response remains unchanged.

These conclusions recommend Fe-28Mn-6Si-5Cr SMA solution treated for 2 hours at 1050 ºC as a potential candidate for the development of active elements for anti-seismic dampers.

References

[1]. Maki T., *Ferrous shape memory alloys, in Shape Memory Materials*, (Otsuka, K. and Wayman, C.M., eds.), Cambridge University Press, p. 117-132, 1998.

[2]. Dong Z. Z., Kajiwara S., Kikuchi T., Sawaguchi T., *Effect of pre-deformation at room temperature on shape memory properties of stainless type Fe-15Mn-5Si-9Cr-5Ni-(0.5-1.5)NbC alloys*, Acta Mater., 53, p. 4009-4018, 2005.

[3]. Bujoreanu L. G., Dia V., Stanciu S., Susan M., Baciu C., *Study of the tensile constrained recovery behavior of a Fe-Mn-Si shape memory alloy*, Eur. Phys. J. Special Topics, 158, p. 15-20, 2008.

[4]. James R. D., Hane K. F., *Martensitic transformations and shape-memory materials*, Acta Mater., 48, p. 197-222, 2000.

[5]. Bergeon N., Guenin G., Esnouf C., *Microstructural analysis of the stress-induced ε martensite in a Fe-Mn-Si-Cr-Ni shape memory alloy: Part II: Transformation reversibility*, Mater. Sci. Eng. A, 242, p. 87-95, 1998.

[6]. Murakami M., Suzuki H., Nakamura Y., *Effect of silicon on the shape memory effect of polycrystalline Fe-Mn-Si alloys*, Trans. ISIJ 27:B87, 1987.

[7]. Kajiwara S., *Characteristic features of shape memory effect and related transformation behavior in Fe-based alloys*, Mat. Sci. Eng. A, 273-275, p. 67-88, 1999.

[8]. Bracke L., Mertens G., Penning J., De Cooman B. C., Liebherr M., Akdut N., *Influence of phase transformations on the mechanical properties of high-strength austenitic Fe-Mn-Cr steel*, Metall. Mater. Trans. A, 37A, p. 307-317, 2006.

[9]. Arruda G. J., Buono V. T. L., Andrade M. S., *The influence of deformation on the microstructure and transformation temperatures of Fe-Mn-Si-Cr-Ni shape memory alloys*, Mater. Sci. Eng. A, 273-275, p. 528-532, 1999.

[10]. Li J. C., Zhao M., Jiang Q., *Alloy design of Fe-Mn-Si-Cr-Ni shape-memory alloys related to stacking-fault energy*, Metall. Mater. Trans. A, 31(3), p. 581-584, 2000.

[11]. Otsuka H., *Fe-Mn-Si Based Shape Memory Alloys*, MRS Proceedings, 246, 309, doi:10.1557/PROC-246, p. 309-320, 1991.

[12]. Druker A. V., Perotti A., Esquivel I., Malarría J., *A manufacturing process for shaft and pipe couplings of Fe-Mn-Si-Ni-Cr shape memory alloy*, Mater. Design, 56, p. 878-888, 2014.

[13]. Maruyama T., Kurita T., Kozaki S., Andou K., Farjami S., Kubo H., *Innovation in producing crane rail fishplate using Fe-Mn-Si-Cr based shape memory alloy*, Mater. Sci. Technol., 24, p. 908-912, 2008.

[14]. Sawaguchi T., Kikuchi T., Ogawa K., Kajiwara S., Ikeo Y., Kojima M., Ogawa T., *Development of prestressed concrete using Fe-Mn-Si-based shape memory alloys containing NbC*, Mater. Trans. 47, p. 580-583, 2006.

[15]. Shahverdi M., Czaderski C., Motavalli M., *Iron-based shape memory alloys for prestressed near surface mounted strengthening of reinforced concrete beams*, Constr. Build. Mater. P. 11228-11238, 2016.

[16]. Sawaguchi T., Maruyama T., Otsuka H., Kushibe A., Inoue Y., Tsuzaki K., *Design Concept and Applications of FeMnSi-Based Alloys from Shape-Memory to Seismic Response Control*, Mater. Trans., 57(3), p. 283-293, 2016.

[17]. Otsuka H., Yamada H., Maruyama T., Tanahashi H., Matsuda S., Murakami M., *Effects of alloying additions on Fe-Mn-Si shape memory alloys*, Trans. ISIJ 30, p. 674-679, doi: 10.2355/isijinternational. 30.674, 1990.

[18]. Sawaguchi T., Sahu P., Kikuchi T., Ogawa K., Kajiwara S., Kushibe A., Higashino M., Ogawa T., *Vibration mitigation by the reversible fcc/hcp martensitic transformation during cyclic tension-compression loading of an Fe-Mn-Si-based shape memory alloy*, Scripta Mater., 54, p. 1885-1890, 2006.

[19]. Bidaux J.-E., Schaller R., Benoit W., *Study of hcp-fcc phase transition in Cobalt by acoustic measurements*, Acta Metall., 37(3), p. 803-811, 1989.

[20]. De A. K., Cabanas N., De Cooman B. C., *Fcc-hcp Transformation-Related Internal Friction in Fe-Mn Alloys*, Z. Metallkd., 93, p. 228-235, 2002.

[21]. Popa M., Lohan N. M., Popa F., Pricop B., Bujoreanu L. G., *Holding-temperature effects on thermally and stress insudec martensitic tranasformations in an FeMnSiCrNi SMA*, Mater. Today Proced., 19, p. 956-962, 2019.

[22]. Dolce M., Cardone D., Marnetto R., *Implementation and testing of passive control devices based on shape memory alloys*, Earthquake Engng Struct Dyn 29, p. 945-968, 2000.

[23]. Paleu V., Gurău G., Comăneci R. I., Sampath V., Gurău C., Bujoreanu L. G., *A new application of Fe-28Mn-6Si-5Cr (mass%) shape memory alloy, for self-adjustable axial preloading of ball bearings*, Smart Materials and Structures, 27(7), 075026, (11pp), 2018.

[24]. Chung C. Y., Chen Shuchuan, Hsu T. Y., *Thermomechanical training behavior and its dynamic mechanical analysis in an Fe-Mn-Si shape memory alloy*, Materials Characterization, 37(4), p. 227-236, 1996.

THE ANNALS OF "DUNAREA DE JOS" UNIVERSITY OF GALATI
FASCICLE IX. METALLURGY AND MATERIALS SCIENCE
Nº. 1 - 2021, ISSN 2668-4748; e-ISSN 2668-4756
Article DOI: https://doi.org/10.35219/mms.2021.1.02

ANALYSIS OF THE BEHAVIOR IN THE WIND TUNNEL OF AN EXPERIMENTAL MODEL OF SAVONIUS WITH INTERLOCKING CUPS WITH THE CLASSIC ONES WITH 2, 3 AND 4 SEMI-CYLINDRICAL CUPS

Nelu CAZACU
"Dunărea de Jos" University of Galaţi, Romania
e-mail: nelu.cazacu@ugal.ro

ABSTRACT

The paper is based on experiments conducted on the wind tunnel at low wind speeds (<9.5 m/s), on an experimental model of S-rotor wind turbine type with four blades and a D/H ratio of 1. Semi-cylindrical cups opposite 180 degrees are aerodynamically coupled by overlap and with an air passage gap to equalize the pressures. The formed channel is shaped to allow the same for pairs of blades at 90 degrees. The experimental model has an area of 0.025 m^2 which represents 10% of the surface of the measuring section of the wind tunnel (0.25 m^2). The behavior of the experimental model was compared with the experimental models of S-rotor with 2, 3 and 4 semi-cylindrical cups, with the same interception surface. The results confirm the better start of the experimental model by reducing dead zones and operating more evenly and stably over a longer range of wind speeds. The results confirm the validity of the proposed concept of interwoven aerodynamic coupling of semi-cylindrical cups.

KEYWORDS: Savonius rotor, S-rotor, low wind, experimental model

1. Introduction

The work is part of the concerns to design and build a Savonius type wind turbine to be characterized by: operation at low wind speeds, independence of wind direction, uniform torque at the shaft, the ability to take wind gusts specific to the urban area. Such a turbine could be integrated in the polygeneration system described in [1, 2]. But in the SE region of Romania there are areas for which the wind has average annual speeds higher than 9 m/s, which makes it possible to include a wind turbine with a vertical axis of Savonius type as an alternative energy source. Also, a very strong wind protection system is needed, a system that is not part of this work.

In the paper [3] were presented the experimental conditions, the results of the experiments performed in the wind tunnel from the laboratory's laboratory of materials for alternative energy sources. The results show that the number of semi-cylindrical buckets used to make experimental models of vertical axis wind turbines (VAWT) of S-rotor type (Savonius) have an important influence on the behavior of experimental models. Important differences are for the situations when the experimental model had 2, 3 or 4 cups. The use of 5 or 6 buckets is no longer of interest due to the increase of the intersection surface of the boom without producing useful torque to the shaft. We mention that the tests performed in the wind tunnel were made in the conditions in which there were no mechanical loads, other than the friction in the bearing bearings.

Fig. 1. *Image with the experimental model S2PCiNL*

THE ANNALS OF "DUNAREA DE JOS" UNIVERSITY OF GALATI
FASCICLE IX. METALLURGY AND MATERIALS SCIENCE
N°. 1 - 2021, ISSN 2668-4748; e-ISSN 2668-4756
Article DOI: https://doi.org/10.35219/mms.2021.1.02

The increase of the number of blades from minimum 2 to VAWT of Savonius type aims to avoid the situation of blocking the wind turbine in the position with the basic plane of the buckets in the wind direction and the uniformity of the torque [4]. Savonius-type VAWT starters with two semi-cylindrical buckets can also be cumbersome if the buckets are in a different position than the maximum torque. Various methods to improve torque uniformity and starting have been tried as is the paper [5].

Fig. 2. *Image with the S2CNL experimental model*

Fig. 3. *Image with the S3CNL experimental model*

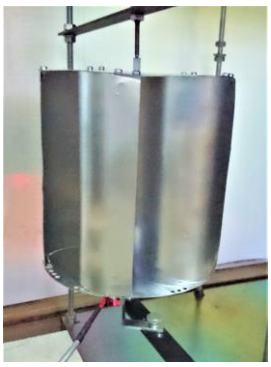

Fig. 4. *Image with the S4CNL experimental model*

Notations:

λ_e - specific speed (TSR – tip speed ratio);
v - wind speed, m/s;
D - Diameter, m;
H - Height, m.

Abbreviations:

RES - Renewable Energy Sources;
HAWT - Vertical Axis Wind Turbine;
EM - Experimental Model;
S2PCiNL - Savonius 1 pair of Cups Interlaced No Load;
S2CNL - Savonius 2 Cups No Load;
S3CNL - Savonius 2 Cups No Load;
S4CNL - Savonius 2 Cups No Load.

Under these conditions, an experimental model of VAWT was proposed (see previous paper [3]) in which the deficiencies of using two diametrical cylindrical cups can be eliminated by using 4 cups, two by two diameters and their aerodynamic coupling by overlap and gap. This creates a channel for equalizing the pressures on the buckets in the maximum torque position, reducing the resistant torque on the return stroke. The practical realization of these channels for the pairs of coupled blades was done by dividing the height of the model and interweaving the coupled blades (Fig. 1).

The same mathematical model of wind energy [6] generated in the tunnel and the same mathematical model of the conversion of wind energy into mechanical work as in the paper are used [3, 5, 7].

The limits of the efficiency of converting wind energy into mechanical work on the shaft are taken into account, a situation specific to Savonius type vertical shaft wind turbines, which leads to a Betz limit of 14.81%.

Although it has a low value of efficiency, this type of wind turbines has a constructive simplicity, a situation that is corroborated and with the increase of the use of electricity obtained can lead to independent sources in important but isolated areas.

2. Experiments

The resulting experimental model (EM) has the same wind interception area (maximum 10% of the cross-sectional area of the wind tunnel measurement area) respectively 0.025 m^2. Dimensions of the model: diameter D = 0.157 m, height H = 0.157 m.

The experiments were performed in a wind tunnel with an adjustable speed between 0-10.5 m/s, which has a measuring section of 0.5 m x 0.5 m x 1.25 m. The wind speed was measured with an LCA6000 anemometer. The experimental model was fixed in point bearings (peaks) and the speed of the experimental model was taken with IR sensor and

THE ANNALS OF "DUNAREA DE JOS" UNIVERSITY OF GALATI
FASCICLE IX. METALLURGY AND MATERIALS SCIENCE
Nº. 1 - 2021, ISSN 2668-4748; e-ISSN 2668-4756
Article DOI: https://doi.org/10.35219/mms.2021.1.02

slotted disk with the ATMEL 328U Microprocessor and recorded with SerialPlot.

The experimental regimes involved a gradual change in the speed of the wind tunnel fan and a decrease in the wind speed from the maximum value to the value at which the model no longer rotates.

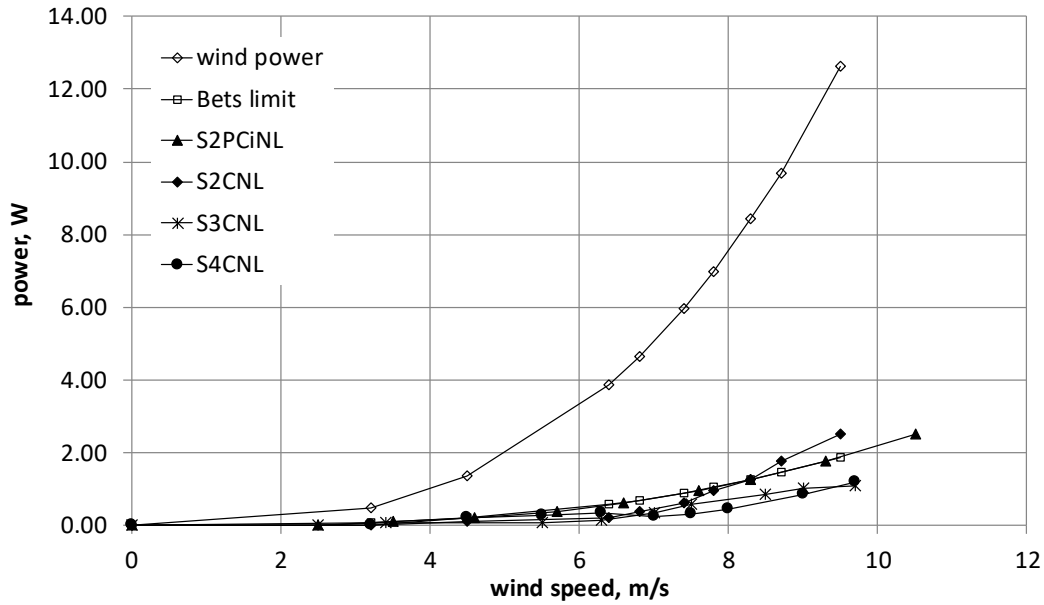

Fig. 5. *Wind power, Betz limit and shaft powers of the considered and reference model*

3. Results and discussions

The results of the tests performed in laboratory conditions on the wind tunnel are shown in Figures 5-14.

Figure 5 shows the wind power, the Betz limit and the axis powers of the considered model and the reference ones. It is observed that the Betz limit for this type of wind turbine based on drag force is according to theory 14.81%. At high wind speeds the S2PCiNL exceeds this limit, which implies the appearance of other mechanisms besides Drag force.

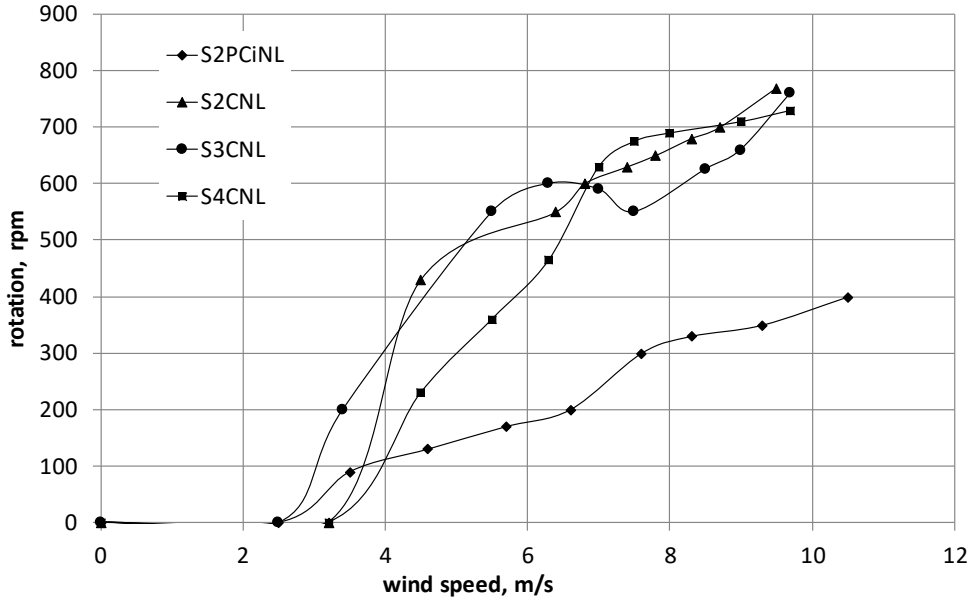

Fig. 6. *Rotation speed variation for S2PCiNL and experimental S-rotor reference models*

THE ANNALS OF "DUNAREA DE JOS" UNIVERSITY OF GALATI
FASCICLE IX. METALLURGY AND MATERIALS SCIENCE
N°. 1 - 2021, ISSN 2668-4748; e-ISSN 2668-4756
Article DOI: https://doi.org/10.35219/mms.2021.1.02

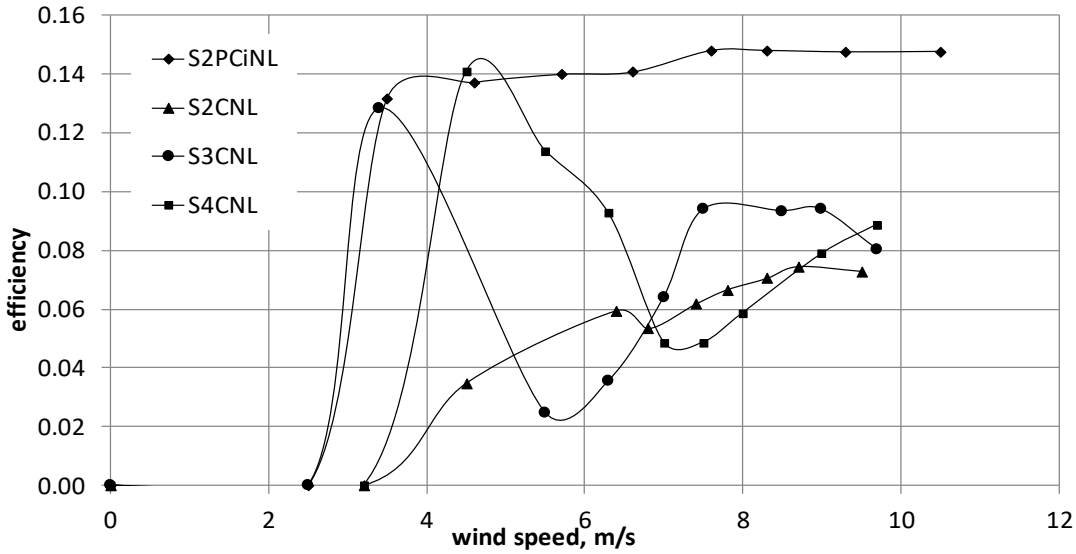

Fig. 7. *Variation of conversion efficiency for S2PCiNL and reference S-rotor experimental models*

The studied experimental model (S2PCiNL) has a good sensitivity regarding the minimum speed at which the rotation starts (2.5 m/s) compared to the Savonius models taken as reference (Fig. 6). A similar behavior has EM Savonius with 3 semi-cylindrical cups, but it has a different behavior from other points of view. Even in terms of wind speed rotation. EM Savonius has an oscillating behavior even if it has a higher rotational speed than the model considered at the same wind speed. The S2PCiNL speed increases approximately linearly from 0-400 rpm for wind speed 2.5 to 10.5 m/s (Fig. 6).

In Fig. 7 is showing variation of conversion efficiency for S2PCiNL and reference S-rotor experimental models.

An important observation (Fig. 7) is regarding the efficiency of the conversion of wind energy into mechanical work which has a narrow range of variation between 0.14 and 0.148 for values of wind speed from 3 m/s to 10 m/s.

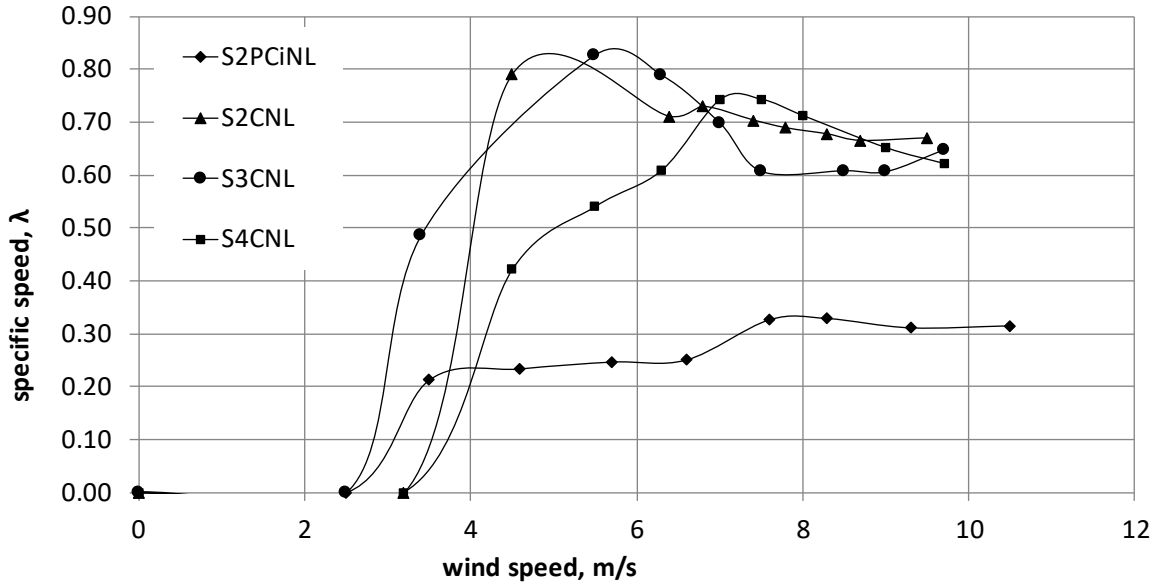

Fig. 8. *Wind speed specific speed variation for S2PCiNL and experimental S-rotor reference models*

THE ANNALS OF "DUNAREA DE JOS" UNIVERSITY OF GALATI
FASCICLE IX. METALLURGY AND MATERIALS SCIENCE
N°. 1 - 2021, ISSN 2668-4748; e-ISSN 2668-4756
Article DOI: https://doi.org/10.35219/mms.2021.1.02

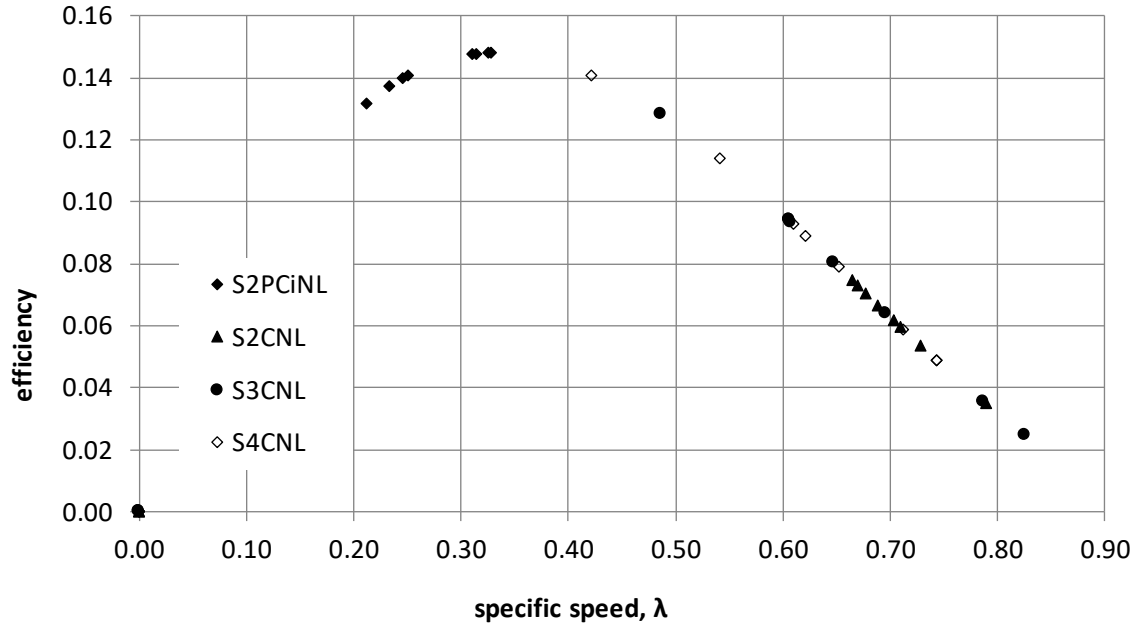

Fig. 9. *Efficiency variation with specific speed for S2PCiNL and for experimental S-rotor reference models*

A very important parameter regarding the operation of wind turbines is the specific or relative speed.

In Fig. 8 is showing specific wind speed variation for S2PCiNL and for the reference S-rotor experimental models. The very different behavior of the experimental model S2PCiNL towards dew references is observed. Thus, the specific speed is lower 0.22-0.32 but remains almost constant over a range of wind speed variation from 3.5 m/s to 10.5 m/s

It is observed (Fig. 9) that the efficiency of the considered experimental model (S2PCiNL) is close to the maximum value of this type of wind turbine but is obtained at low speeds of the specific speed (0.2-0.3) which shows the special behavior of this type of experimental model. For the other Savonius turbine models taken as a reference, the efficiency is deviated from the maximum value.

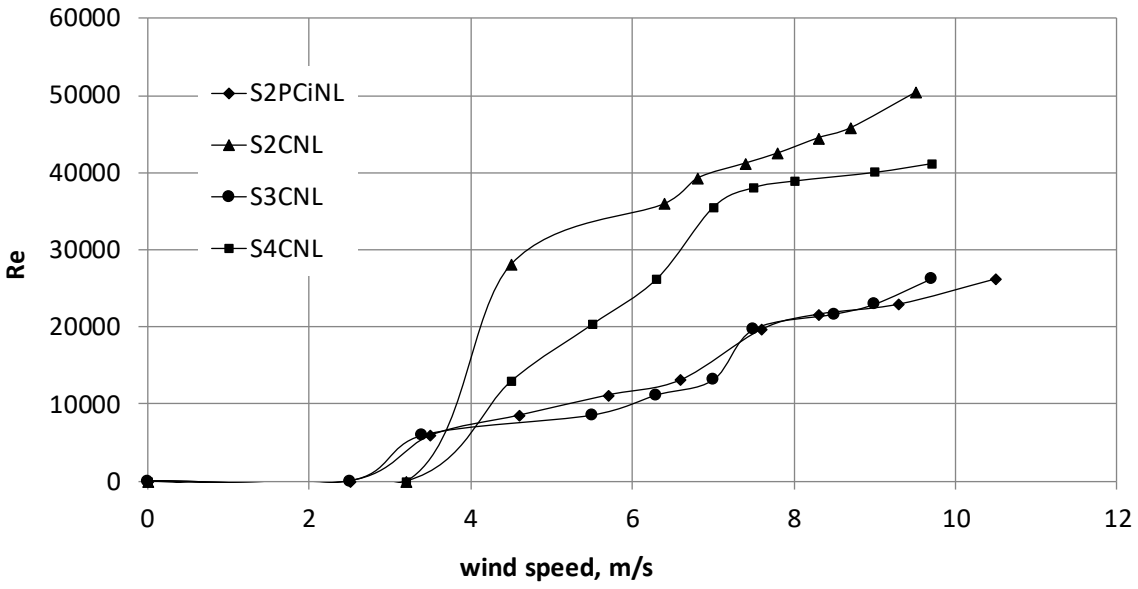

Fig. 10. *Re number variation with wind speed for S2PCiNL and for experimental S-rotor reference models*

THE ANNALS OF "DUNAREA DE JOS" UNIVERSITY OF GALATI
FASCICLE IX. METALLURGY AND MATERIALS SCIENCE
Nº. 1 - 2021, ISSN 2668-4748; e-ISSN 2668-4756
Article DOI: https://doi.org/10.35219/mms.2021.1.02

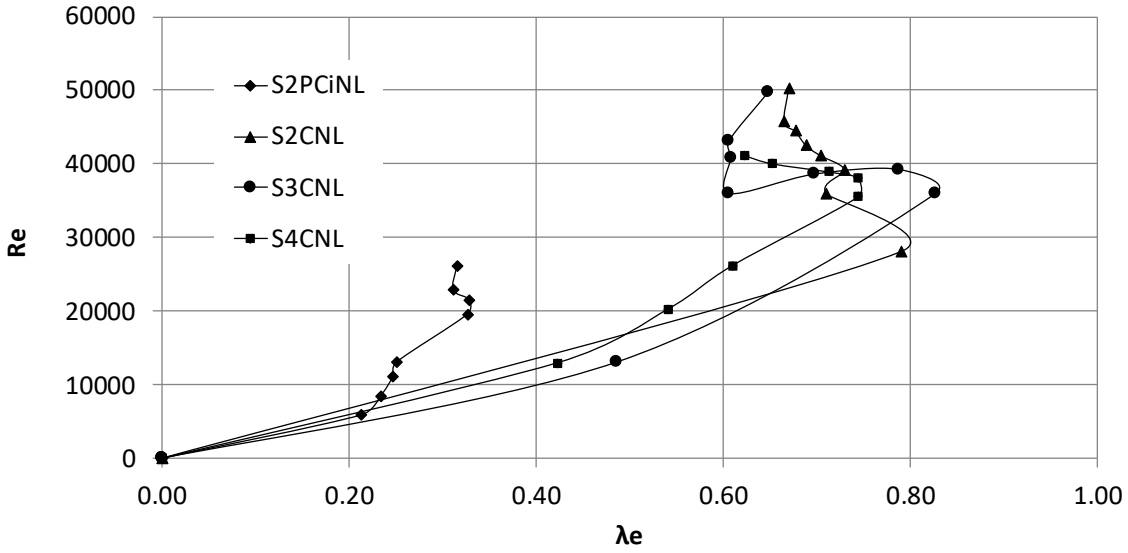

Fig. 11. *Specific speed Re number variation (TSR) for S2PCiNL and S-Rotor experimental reference models*

From the point of view of the variation Re number for S2PCiNL it is observed in Fig. 10. The behavior is very close to S3CNL and very different from S2CNL and S4CNL. For the considered model RE number varies almost linearly from 0-25000 for wind speed between 2.5 and 10 m/s.

Compared to their equivalent speed, Re number has a much different variation than for the experimental S-rotor models taken as reference (Fig. 11). Thus, if for the experimental models S-rotor reference with 2, 3 and 4 cups Re number have maximum values between 30000-50000 for the specific speed 0.6-0.8 for the experimental model Re number does not exceed 25000 for a narrower speed range around 0.3.

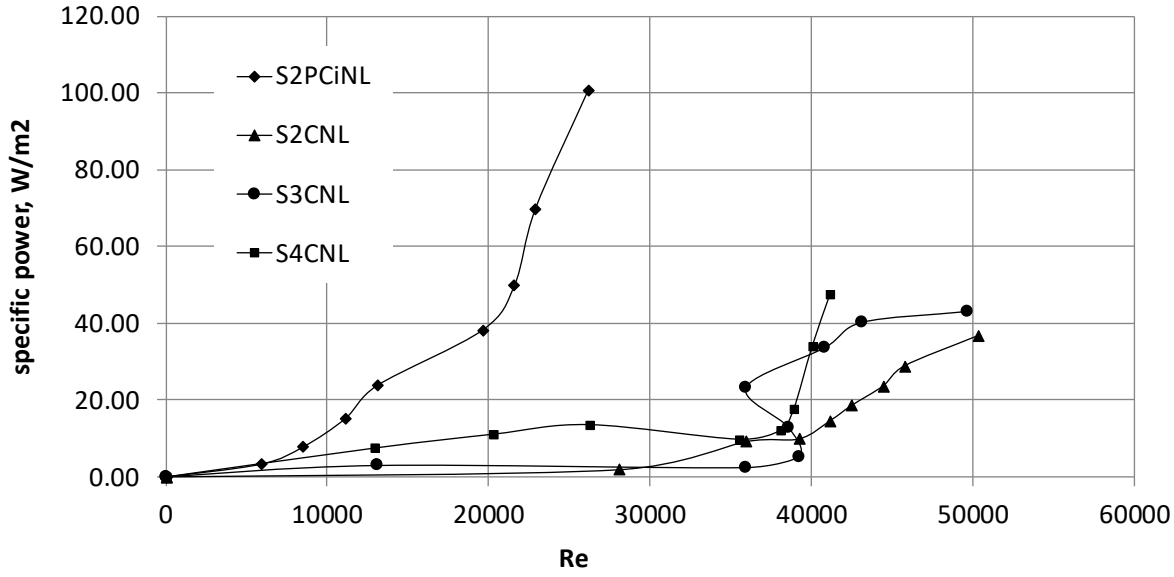

Fig. 12. *Shaft specific power according to Re number for S2PCiNL and for experimental S-rotor reference models*

THE ANNALS OF "DUNAREA DE JOS" UNIVERSITY OF GALATI
FASCICLE IX. METALLURGY AND MATERIALS SCIENCE
Nº. 1 - 2021, ISSN 2668-4748; e-ISSN 2668-4756
Article DOI: https://doi.org/10.35219/mms.2021.1.02

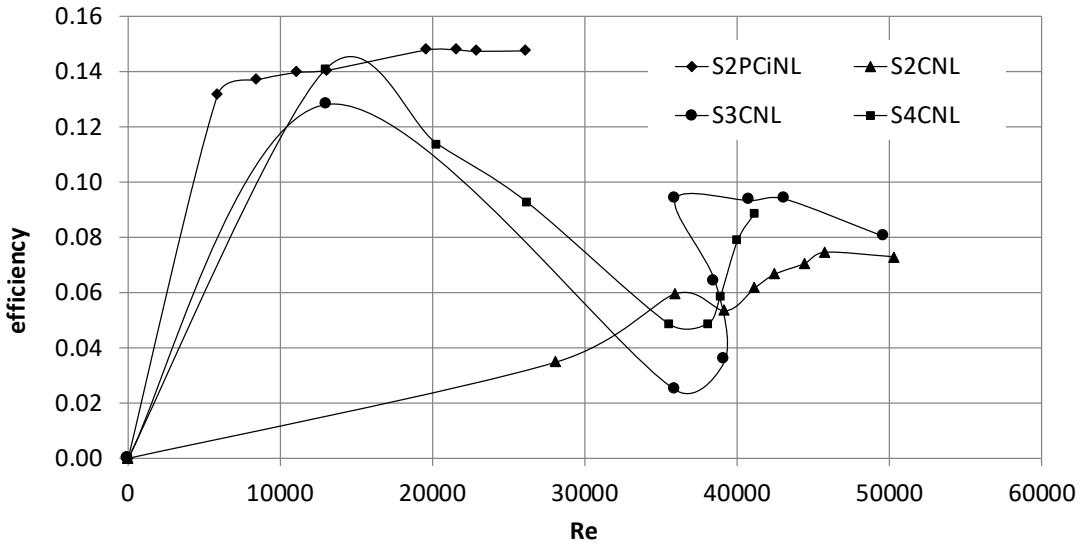

Fig. 13. *Efficiency of the experimental model S2PCiNL and for experimental models S-rotor reference function Re number*

Fig. 12 shows the specific shaft power depending on the Re number for S2PCiNL and for the experimental S-rotor reference models. The different behavior of the S2PCiNL experimental model is observed which has a specific power at the shaft that exceeds 2.5 times at Re number by half.

And the efficiency of the studied experimental model (S2PCiNL) with Re Number shows different behavior than for the reference S-rotor experimental models (Fig. 13). It is close to the maximum value of the Betz limit, but more importantly it has a high value on a line that increases in a range of Re number from 5000 to 25000. In Fig. 14 show the variation of the specific shaft power with wind speed for S2PCiNL and for the experimental reference S-rotor models. It is observed that the specific power at the shaft is the highest of the models considered, which is an important premise regarding the experiments that will be performed on this model with mechanical and electrical loads.

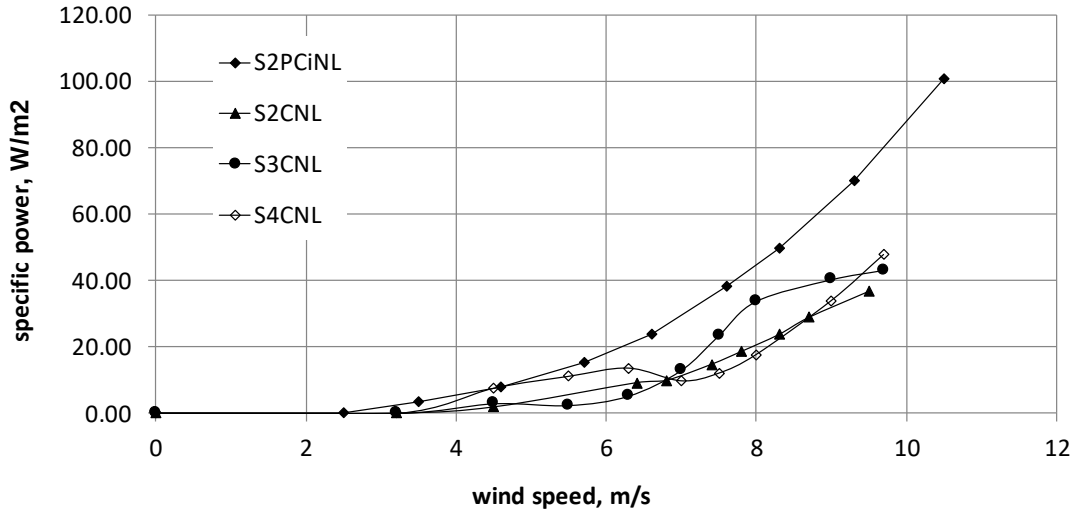

Fig. 14. *Shaft specific wind power variation for S2PCiNL and reference S-rotor experimental models*

4. Conclusions

The experimental model (Fig. 1) studied in the wind tunnel up to speeds of 10.5 m/s falls within the Betz limit up to WIND speeds lower than 8.5 m/s then exceeds this limit, which shows the existence of other mechanisms which produce the rotational motion other than drag force D (Fig. 5). The rotation speed increases linearly from 2.5 m/s to 10.5 m/s (Fig. 6) but is lower than the experimental models of

Savonius turbine with 2, 3 and 4 semi-cylindrical buckets (Fig. 2, Fig. 3 and Fig. 4). The specific lambda speed (Fig. 8) has values between 0.2-0.3 for wind between 3.5-10.5 m/s, almost 2-3 times lower than the maximum value of the reference EMs. Due to the low rotation Re number has lowers values but increases linearly with wind speed (Fig. 10). This is also confirmed by the variation of Re number with the specific velocity λ_e (Fig. 11) which shows much lower values than the experimental models referred to. The conversion efficiency to mechanical work has values over 14% for wind speeds of 4-10.5 m/s. The experimental model S2PCiNL has the best efficiencies of conversion to mechanical work (Fig. 9) and for a wide range of Re number between 10000 and 25000 (Fig. 13). The specific power at the shaft (Fig. 12 and Fig. 13) shows maximum values of 100 W/m^2 at Re number 25000 and at wind speed of 10.5 m/s. Stable and uniform operation in a range of wind speeds and efficiency at no load are prerequisites for good performance in load tests.

References

[1]. Badea Nicolae, et al., *Sistem integrat de poligenerare descentralizata a energiei din surse regenerabile*, CBI A/00402/2011, 29 Aprilie 2011.

[2]. Cazacu Nelu, *Renewable Energy Sources for the mCCHP-SE-RES System*, [autorul cărții] Badea N (ed). Design for Micro-combined Cooling Heating and Power System, London: Springler, 2015.

[3]. ***, *Experimental Model of Wind turbime with Vertical Axis, Multy-Storey and with two Pairs of Blades on level Aerodynamic Coupled*, The Annals of "Dunarea de Jos" University of Galati, Fascicle IX, Metallurgy and Materials Science, vol. 2, p. 21-26, ISSN 2668-4748, e-ISSN 2668-4756, 2019.

[4]. Menet J. L., Bourabaa N., *Increase in a savonius rotor efficiency*.

[5]. Cazacu Nelu, *Improving the Powerful Behavior of an ExperimentaL model of Savonius Turbine (S-rotor) with Couple Aerodynamic Additional Blades*, The Annals of "Dunărea de Jos" University of Galati, Fascicle IX, Metallurgy and Materials Science, Galati University Press, vol. 2, p. 49-53, ISSN 1453 083X, 2018.

[6]. Hau Erich, *Wind Turbines, Fundamentals, Technologies, Applications, Economics*, s.l.: Springler, 2006.

[7]. Cazacu, Nelu, *Load Behavior of a Vertical Axle Wind Turbine Model with Four Blades Periodically Couple Aerodynamically*, The Annals of "Dunarea de Jos" University of Galati, Fascicle IX, Metallurgy and Materials Science, Galati University Press, vol. 3, p. 5-11, ISSN 2668-4748, e-ISSN 2668 4756, 2018.

THE ANNALS OF "DUNAREA DE JOS" UNIVERSITY OF GALATI
FASCICLE IX. METALLURGY AND MATERIALS SCIENCE
N°. 1 - 2021, ISSN 2668-4748; e-ISSN 2668-4756
Article DOI: https://doi.org/10.35219/mms.2021.1.03

NON-DESTRUCTIVE TESTING OF DISSIMILAR WELDED JOINTS

Maria-Cristina DIJMĂRESCU
Politehnica University of Bucharest, Romania
e-mail: maria.dijmarescu@upb.ro

ABSTRACT

This paper presents research's results of non-destructive examination of dissimilar welded samples. The samples were made using sheets of austenitic stainless steel and carbon steel welded through the method of MAG welding with tubular wire. The samples were subjected to non-destructive testing in order to analyse the integrity of the welded seam, heat affected zone and the adjacent area of the weld.

KEYWORDS: non-destructive testing, austenitic stainless steel, carbon steel, dissimilar welded join, MAG welding

1. Introduction

Quality assessment can be put into practice by knowing the quality characteristics that are linked to a system of indices, indicators and coefficients. The assessment is required by the complexity of products and processes, being able to synthetically express a number of aspects of quality [1, 2].

The quality inspection of welded joints is an extremely complex branch, with many methods, techniques, and analysis and evaluation tools available. In order to be able to understand and use the quality assessment methods, a study of the specialized terminology currently used in this field, a terminology to be used in this paper, was also carried out. Terminology have been defined as: welding, imperfection, etc. [2-4].

The inspection methods for welded joints were presented and their classification in the three categories - the production process, the integrity of the product under examination and the number of products checked [4].

The imperfections of welded joints represent any deviation from shape, size, continuity, structure, appearance, composition or properties prescribed for a particular seam in the technological documentation. These have the effect of reducing resistance and worsening behavior in the exploitation of a welded joint. [5, 6].

Because the nonconformities can affect the performance and longevity of welded joints, early detection and correction is essential to ensure that the welded structures meet their designing purpose. After detecting the nonconformities in welded joints, an assessment should be made to determine their severity and the appropriate measures to be taken. Even the hardest to detected imperfection may encounter an inadequate welded structure to achieve its intended purpose [6, 7].

Detection techniques must be sensitive enough to detect dangerous discontinuities. It is necessary to repair the defects that damage the structural integrity of the welded joint. Welds do not have to be perfect; they must be within the permissible work limits specified in the quality standards used during the welded structure inspection [4, 6, 7].

After analysing the specialty literature in order to highlight the welding processes used to obtain dissimilar welding joints the following processes were identified:

- gas metal arc welding, MIG/MAG, with normal and tubular wire [8-10];
- gas tungsten arc welding, WIG [11-13];
- friction welding [14];
- electron beam welding [15];
- fiber laser welding [16], etc.

The MIG/MAG process is the most used for manufacturing dissimilar joints and the combination between stainless steels and structural steels is widely used because of the economic benefits.

Examination of welded joints begins with the examination of the materials used in the welding process and ends with the final examination of the resulting joint. The final examination consists in checking the welded joint using different non-destructive methods. These methods are classified in two categories [17-19]: destructive and non-destructive examination.

The non-destructive examination methods used to examine the welded structure are chosen by taking

THE ANNALS OF "DUNAREA DE JOS" UNIVERSITY OF GALATI
FASCICLE IX. METALLURGY AND MATERIALS SCIENCE
Nº. 1 - 2021, ISSN 2668-4748; e-ISSN 2668-4756
Article DOI: https://doi.org/10.35219/mms.2021.1.03

into account the geometry of the part, the surface and the accessibility of the part to be examined.

The methods used to verify the structures are divided into two categories, and namely [17, 18]:

• Methods to highlight surface and near surface imperfections that are dependent on the surface area and accessibility to the examination. These include:

- Visual Testing (VT) - used to detect surface imperfections and also as an integrated part of the others non-destructive methods.
- Penetrant Testing (PT) - used to detect imperfections which are open to the surface of the tested material. It is applied on metallic materials, but also on non-metallic materials, e.g., ceramics.
- Magnetic Testing (MT) - used for the detection of surface imperfections and below the surface in ferromagnetic forgings, castings and welds including the heat affecting zones using the continuous Its sensitivity is reduced rapidly with the depth.
- Eddy Current Testing (ET) - used for the detection of surface breaking and near surface planar defects and it is applied on welds of almost any configuration.

• The methods used to identify inner imperfections are dependent on the geometric geometry of the part to be examined. Most commonly used are Ultrasound Testing (UT) and Radiographic Testing (RT), both used to detect inner and surface imperfections in welds. They can be applied on any type of material, taking into account the specific limitations for each method and the security norm for radiographic testing.

• In addition to the methods mentioned, the following method is also evaluated:

- leak Test (LT) - highlights fluid leaks.
- Infrared Thermography (TT) - allows the detection of defects in layered, coated, glued, composite materials; measuring the thickness of coatings or coatings; characterization of materials in terms of thermal behavior; evaluation of the structure of polymeric composite materials, analysis or measurement of the heat flux provided by the examined product (heat exists or is produced independently of the examination process).
- Acoustic Emission (AT)- allows monitoring the structures integrity, report losses through leakage, the early detection of cracks or even when they appear, characterizing the behavior of materials.

This paper presents the applications of different non-destructive methods in order to identify the imperfections in dissimilar welded joints. To achieve the proposed activities, the following steps were taken establishment of welding technology used for sample making, welded joints making, mechanical and chemical cleaning (degreasing) of samples, Visual Testing, Penetrant Testing, Ultrasound Testing, Radiographic Testing.

2. Experimental data

2.1. Sample description

At present, the joint between two dissimilar materials, steel carbon, S235JR + AR and a stainless steel austenitic, X2CrNiMo17-12-2, are often used, for this reason for making the experiments was chosen to perform a dissimilar welded joint.

Carbon steel and austenitic stainless steel were used as materials for the samples, the two steels being representative of the classes they belong to.

The experimental plan consists of the following steps: choice of the basic material, choice of the welding groove: type and geometry, choice of the welding process, selection of the filler material and execution of the welded joints.

The chemical composition and the mechanical proprieties of the base materials are presented in Table 1 and Table 2.

The selection of the filler material for making the dissimilar welded joint from the range of materials made available was done by means of an analysis. The analysis was made using the software Autodesk Inventor. This consisted of a series of stress and fatigue strength for the type of groove chosen at the previous point.

Table 1. *Chemical composition of the base materials* [20, 21]

Chemical Composition	C %	Cr %	Mn %	Mo %	N %	Ni %	P %	S %	Si %
X2CrNiMo17-12-2 EN ISO 100088-3	0.03	16-18	2	2-3	0.10	10-14	0.045	0.03	0.75
S235JR + AR EN10027-2	0.17	-	1.40	-	0.012	-	0.035	0.035	-

THE ANNALS OF "DUNAREA DE JOS" UNIVERSITY OF GALATI
FASCICLE IX. METALLURGY AND MATERIALS SCIENCE
N°. 1 - 2021, ISSN 2668-4748; e-ISSN 2668-4756
Article DOI: https://doi.org/10.35219/mms.2021.1.03

Table 2. *Mechanical proprieties of the base materials* [20, 21]

Properties	X2CrNiMo17-12-2 -Value	S235JR + AR - Value
Yield strength (R_{p02})	170 N/mm^2	Max. 235 N/mm^2
Tensile Strength (R_m)	485 N/mm^2	360-510 N/mm^2
Elongation (A_5)	min. 40%	Max. 26 %

As a result of the analysis, T 23 12 L PC / M 1 is the best choice for making the dissimilar welded joints between carbon steel S235JR + AR and austenitic stainless steel X2CrNiMo17-12-2.

Subsequently, the chemical composition of the wire used, and the mechanical properties of the melt metal are presented in Table 3, respectively Table 4.

Table 3. *Chemical composition of the filler material* [22]

Chemical Composition	C %	Cr %	Mn %	Mo %	N %	Ni %	P %	S %	Si %
T 23 12 LPC/M 1	0.04	22.85	0.60	0.162	0.0266	12.54	0.019	0.009	0.65

Table 4. *Mechanical proprieties of the filler material* [22]

Properties	T 23 12 LPC/M 1-Value
Yield strength (R_{p02})	460 N/mm^2
Tensile Strength (R_m)	610 N/mm^2
Elongation (A_5)	min. 31%

2.2. Welding process

The MAG process was chosen using the M21 protection gas (Ar + 18% CO_2) for welding the samples. The parameters of the welding regime used in the experiments were determined in accordance with the manufacturer's recommendations.

The following steps were taken to prepare the welding samples:

- Plate cutting to size - The base materials prepared for the experiment are the steels: S235JR+AR and X2CrNiMo17-12-2 in form of plates with the dimensions 350 mm x 225 mm x 15 mm. The cutting of the plates was performed using a Hypertherm Powermax 105 plasma cutting machine.

- The gripping of the parts for welding - The plates were fastened by using two steel plates, then placed on the welding table and subsequently the connecting to the table and to the welding source was made.

- The welding of the samples:

- Equipment used - a MIG / MAG TM 500 W Welding Machine was used to perform samples using the MAG process. For measuring the temperature between the layers, a Voltacraft IR900-30S Thermometer was used.

- The welding - The welding of the samples was conducted with a ceramic root using the MAG process. The groove configuration presented in Figure 1.

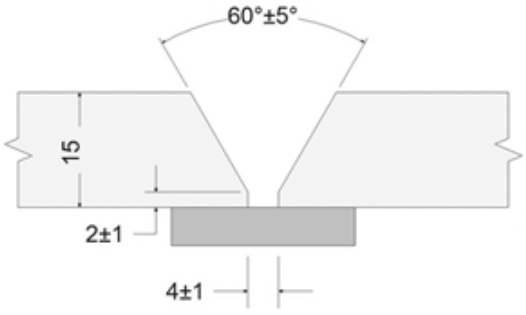

Fig. 1. *The groove configuration and the positioning of the ceramic support*

THE ANNALS OF "DUNAREA DE JOS" UNIVERSITY OF GALATI
FASCICLE IX. METALLURGY AND MATERIALS SCIENCE
N°. 1 - 2021, ISSN 2668-4748; e-ISSN 2668-4756
Article DOI: https://doi.org/10.35219/mms.2021.1.03

The set parameters were monitored during the entire welding process, ascertaining differences of maximum 3 A for the amperage and 1 V for the welding arc.

The welding parameters used are presented in Table 5.

Table 5. *Welding parameters*

Welding parameter	Values for the root layer	Values for the intermediate layers (3 layers)	Values for the surface layers
Welding current, I_s [A]	170 ±10	170 ±10	170 ±10
Welding arc voltage, U_a [V]	29 ±2	29 ±2	29 ±2
Welding speed, v_s [mm/s]	1.71	2.14 1.84. 1.79	4.8
Feed rate of welding wire, v_a [m/min]	4.8 ± 0.1	4.8 ± 0.1	4.8 ± 0.1
Gas flow (Ar 82% +18% CO_2), D_g [l/min]	18 ± 1	18 ± 1	18 ± 1

2.3. Non-destructive examination of the samples

In order to analyse the quality of the welded joint obtained a series of non-destructive examination methods were used, after which specimens were taken to carry out the destructive tests.

In order to highlight any imperfections, present in the welded structure obtained, the sample was subjected to Visual Testing, Penetrant Testing, Ultrasound Testing and Radiographic Testing.

Visual inspection of the welded structure was performed using the direct viewing method.

2.3.1. Dry Penetrant Testing

In order to highlight the small imperfections on the surface of the test sample (which cannot be detected visually) or in the immediate vicinity of the surface, the test with penetrant liquid was used.

Fig. 2. *Penetrant testing of the Miller etalon*

For the examination using Penetrant Testing the following were established: ambient temperature: 20 °C; set of penetrating liquids: penetrant PFINDER 860 type and developer PFINDER 870 type; calculation of geometric sensitivity using the Miller standard and penetration and development time: 10 min.

For calculation of geometric sensitivity, the Miller etalon was used, see Figure 2. After the calculations, a geometric sensitivity of 0.965 was obtained.

Steps followed:

a) Sample cleaning - the sample was chemically cleansed by degreasing: PFINDER 890 degreaser.

b) Drying of the surface - forced by a hot air jet.

c) Applying the PFINDER 860 penetrant:

- The penetrant has been applied to the contact surface by spraying.
- Dwell time used: 10 min.

d) Removing the excess of penetrant - the excess penetrant was removed by washing.

e) Surface drying - forced by a hot air jet.

f) Application of developer PFINDER 870:

- The developer was applied uniformly and thinly layer over the entire examined surface, only after being well agitated.
- After application of the developer, the surface examined was allowed to dry at room temperature.
- The development time begins immediately after surface drying; the development time was 10 minutes.

g) The interpretation of the results was achieved at the end of the development time.

- Upon examination with penetrating liquids, it was found that the piece had no detectable

THE ANNALS OF "DUNAREA DE JOS" UNIVERSITY OF GALATI
FASCICLE IX. METALLURGY AND MATERIALS SCIENCE
No. 1 - 2021, ISSN 2668-4748; e-ISSN 2668-4756
Article DOI: https://doi.org/10.35219/mms.2021.1.03

imperfections by this method on the surface under consideration.

The penetrant testing kit used it is presented in Figure 3, and the result obtained after the testing of the samples.

Upon examination with penetrating liquids, it was found that the piece had no detectable imperfections by this method on the surface under consideration.

Fig. 3. *Penetrant testing kit*

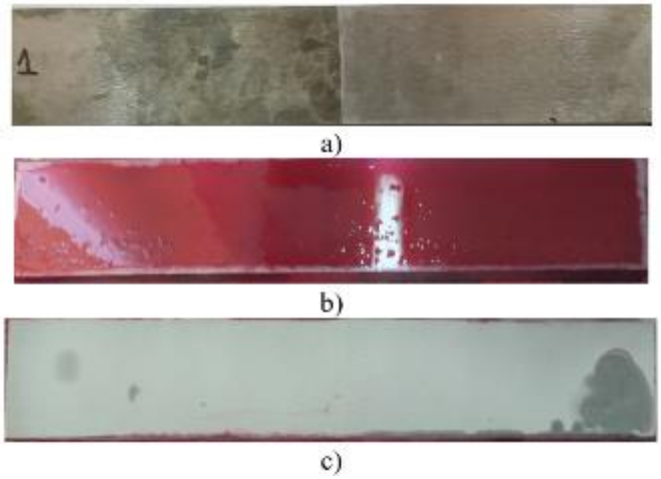

Fig. 4. *Penetrant testing of the samples: a - test sample, b - application of the penetrant layer; c - the result obtained after drying by the developer*

2.3.2. Ultrasound Testing

To perform the examination, an Olympus Defectoscope was used and two transducers with inclined incidence at the angles of 60^{O} and 70^{O}.

To see if the chosen equipment and technique can be applied to the type of joint performed, a specimen was debited from the samples, in which imperfections with a diameter of 3 mm were formed at a depth of 6 mm on the edge of the welding seam, in cross-section. The experimental stand used for the ultrasound testing; the reflected pulse method is presented in Figure 5.

Subsequently the welded joints were subjected to ultrasound examination by the TOFD technique. In Figure 6 and 7 one of the TOFD report is presented.

Fig. 5. *Ultrasound testing of the samples*

THE ANNALS OF "DUNAREA DE JOS" UNIVERSITY OF GALATI
FASCICLE IX. METALLURGY AND MATERIALS SCIENCE
Nº. 1 - 2021, ISSN 2668-4748; e-ISSN 2668-4756
Article DOI: https://doi.org/10.35219/mms.2021.1.03

Ultrasound Report

Report Date	Report Version	Data File Name	Inspection Date	Inspection Version	Hardware Type
2016 / 05 / 12	OmniscanConverter - 2.10R10	PROBA 1 ##	2016 / 05 / 11	MXU - 3.1R3	OMNI-M-UT-8C

Group 1

Setup

P1-R2 TOFD

Beam Delay	Start (Full Path)	Range (Full Path)	PRF	Type	Averaging Factor
10.28 us	10.85 us	5.28 us	6000	UT	1
Pretrig.	**Rectification**	**Band-Pass Filter**	**Voltage**	**Gain**	**Mode**
0.00 us	RF	Band-pass 2.00 MHz	50 V	42.00 dB	TOFD (Time-of-Flight Diffraction)
Wave Type	**Sound Velocity**	**Pulse Width**	**Scan Offset**	**Index Offset**	**Scan Type**
Longitudinal	5890.0 m/s	50.00 ns	0.00 mm	0.00 mm	Nonparallel
Conditional A-Scan	**Gate Saved**				
Off	Off				
PCS					
50.00 mm					

Gate	Start (Full Path)	Width (Full Path)	Threshold	Peak Selection	Link
I	0.00 us	6.79 us	20.00 %	Max. Peak	
A	6.79 us	10.18 us	25.00 %	Max. Peak	
B	13.58 us	6.79 us	30.00 %	Max. Peak	

Part

Material	Geometry	Thickness
STEEL, MILD	Plate	15.00 mm

Scan Area

Scan Start	Scan Length	Scan Resolution	Index Start	Index Length	Index Resolution
0.00 mm	280.00 mm	1.00 mm	0.00 mm	0.00 mm	1.00 mm
Synchro	**Max. Scan Speed**				
Encoder	6000.00 mm/s				

Axis	Encoder	Encoder Type	Encoder Resolution	Polarity
Scan	1	Quadrature	12.00 step/mm	Normal
Index	Off	Off	Off	Off

Fig. 6. *TOFD parameters*

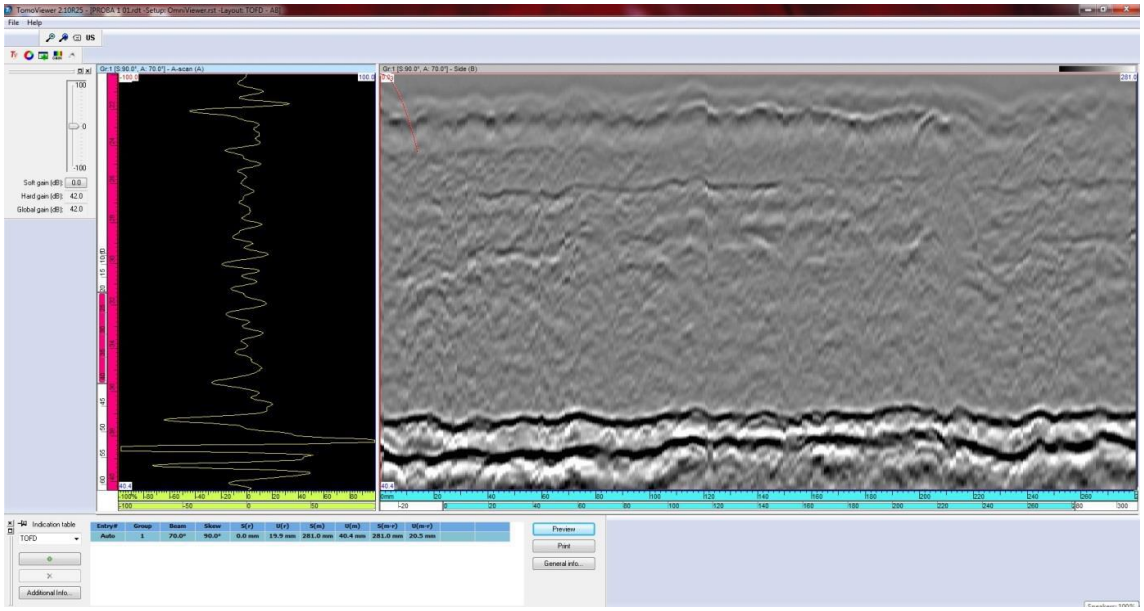

Fig. 7. *TOFD report results*

THE ANNALS OF "DUNAREA DE JOS" UNIVERSITY OF GALATI
FASCICLE IX. METALLURGY AND MATERIALS SCIENCE
N°. 1 - 2021, ISSN 2668-4748; e-ISSN 2668-4756
Article DOI: https://doi.org/10.35219/mms.2021.1.03

2.3.3. Radiographic Testing

Due to the fact that after the ultrasound examination the results were inconclusive, the samples were subsequently examined by Radiographic Testing.

The examination of the steel samples was carried out with the help of the X-ray non-destructive testing, obtaining the image on a radiographic film.

Technical data:

- Sample: dissimilar welded joint sheet between carbon steel and austenitic stainless steel.
- Material: steels S235JR and X2CrNiMo17-12-2.
- Dimensions: thickness 12 mm, length 350 mm, width 450 mm.
- Exposure geometry: Normal geometry.
- Radiography technique: a wall.
- Radiography class: Class B
- Radiographic parameters:
  - a X-ray tube parameters: U = 150KV; I = 4.5 mA;
  - a source-film distance = 500 mm;
  - an exposure time = 1 minute and 30 seconds.
- Quality indicators used: Group 1 H Fe with the following hole diameters: Visible H 4
- Film FOMAPAK BOHEMIA CZECH REPUBLIC, EU (R5 + Pb).
- Very high blackness density = 3.
- Image blur index = the number of the largest perceptible element.

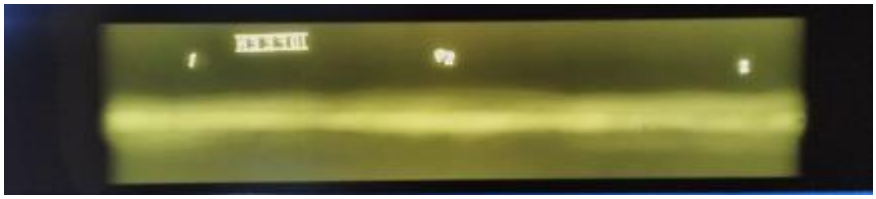

Fig. 8. *Radiographic film-sample 2*

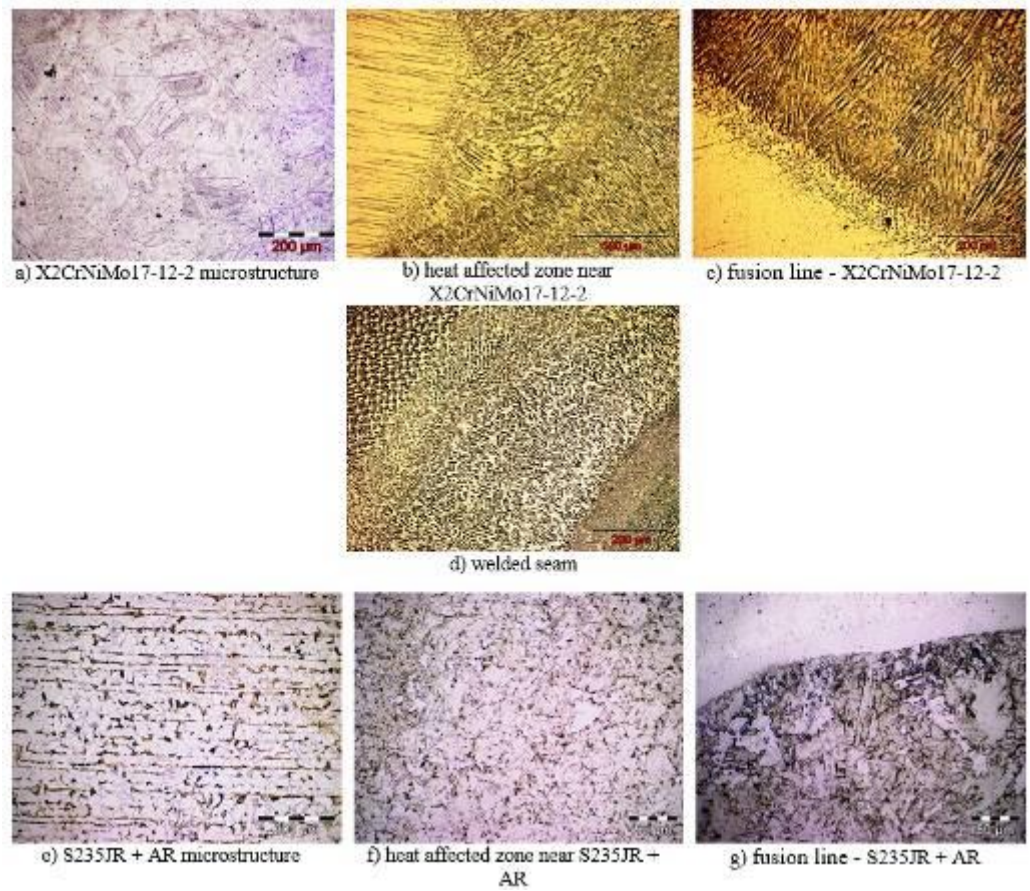

Fig. 9. *Microscopic analysis*

THE ANNALS OF "DUNAREA DE JOS" UNIVERSITY OF GALATI
FASCICLE IX. METALLURGY AND MATERIALS SCIENCE
N°. 1 - 2021, ISSN 2668-4748; e-ISSN 2668-4756
Article DOI: https://doi.org/10.35219/mms.2021.1.03

There were no imperfections of the interior highlighted using the Radiographic Testing, result which attest to the quality of the welded joint, as it can be seen from Figure 8.

In order to analyse the microstructure obtained destructive examination was applied. In figure 9 is presented the microstructure obtained in the areas of interest, namely: the heat-affected area, the fusion line, and the welded seam.

After analysing the microscopic images obtained the differences in structure can be seen, as follows:

• Stainless steel, X2CrNiMo17-12-2, shows microstructure with snail polyhedron grains and intragranular precipitations.

• Carbon steel, S235JR + AR, presents a ferrite-perlite microstructure in alternating ferrite and perlite strings.

• The fusion line between carbon steel, S235JR + AR (lower part), and deposition by welding with a high alloyed material (top). The HAZ shows the tendency to increase the granulation and the formation of the perlite and the coarse ferrite - Widmanstätten type.

• The fusion line between austenitic stainless steel, X2CrNiMo17-12-2, and welding with a high alloyed material. One biphasic ferrite and austenitic dendritic microstructure can be observed.

• In the heat affected zone near S235JR + AR a modified ferrite and perlite structure is observed.

• In the heat affected zone near X2CrNiMo17-12-2 a dendritic microstructure directed towards the direction of the thermal delta and austenite ferrite flow is observed.

• The welded seam shows a dendritic structure of delta and austenite ferrite.

3. Conclusions

From the analysis of the presented, important conclusions are drawn as follows:

- Dissimilar welded samples using the MAG welding process were created.

- After the welding process the samples were non – destructively tested.

- No imperfections have been identified following Visual Testing and Penetrant Testing.

- The result obtained using Ultrasound Testing, through the two methods of welded samples was inconclusive, due to the difference in structure between the two basic materials.

- Ultrasonic examination of austenitic stainless steel is difficult because of the grain size. Due to the fact that the austenitic stainless steel presents a coarse structure in case of ultrasound testing the grain boundary sometimes can be mistaken as a flow by the equipment. On the screen of the ultrasound defectoscope a sonic grass can be observed which can mask small imperfections making them impossible to detect.

- The examination with Radiographic Testing confirmed the lack of imperfections in the welded samples.

Acknowledgment

This work has been funded by the European Social Fund from the Sectoral Operational Programme Human Capital 2014-2020, through the Financial Agreement with the title "Scholarships for entrepreneurial education among doctoral students and postdoctoral researchers (Be Antreprenor!)", Contract no. 51680/09.07.2019 - SMIS code: 124539.

References

[1]. Baldev Raj, Subramanian C. V., Jayakumar T., *Non-Destructive Testing of Welds*, Alpha Science International, Limited, 2001.

[2]. Paul Kah, Belinga Mvola, Jukka Martikainen, Raimo Suoranta, *Real Time Non-Destructive Testing Methods of Welding*, Advanced Materials Research, vol. 933, p. 109-116, https://doi.org/10.4028/www.scientific.net/AMR.933.109, 2014.

[3]. Baughurst L., Voznaks G., *Welding defects, causes and correction, Australian Bulk Handling Review*, http://courseware.cutm.ac.in/wp-content/uploads/2020/06/welding_defects_causes__correction.pdf, July/August 2009.

[4]. Oral Büyüköztürk, Mehmet Ali Taşdemir, *Nondestructive Testing of Materials and Structures*, Springer Science & Business Media, 2012.

[5]. Scutelnicu E., Constantin E., *Heat input influence on structural changes in carbon steel – stainless steel welded joints*, Proceedings of the 10th International Metallurgy and Materials Congress, ISSN 1301-3637, Istanbul, Turkey, vol. II, p. 1239-1244, 24-28 May 2000.

[6]. Taban E., Deleu E., Dhooge A., Kaluc E., *Evaluation of dissimilar welds between ferritic stainless steel modified 12% Cr and carbon steel S355*, Weld. J., 87, p. 291-297, 2008.

[7]. Dijmărescu Maria-Cristina, Dijmărescu Manuela-Roxana, *Welding Material Selection for a Specific Butt V-Weld by Means of Assisted Stress and Fatigue Calculations*, ISMEMS 2016, Advances in Engineering Research, vol. 93, Atlantic Press, p. 61-66, 2016.

[8]. Mvola B., Kah P., Martikainen J., *Dissimilar ferrous metal welding using advanced gas metal arc welding processes*, Rev. Adv. Mater. Sci., 38, p. 125-137, 2014.

[9]. Tasalloti H., Kah P., Martikainen J., *Effect of heat input on dissimilar welds of ultra high strength steel and duplex stainless steel: Microstructural and compositional analysis*, Mater. Charact., 123, p. 29-41, DOI: doi.org/10.1016/j.matchar.2016.11.014, 2017.

[10]. Ghosh N., Kumar Pal P., Nandi G., *GMAW dissimilar welding of AISI 409 ferritic stainless steel to AISI 316L austenitic stainless steel by using AISI 308 filler wire*, Eng. Sci. Technol., 20, p. 1334-1341, DOI: doi.org/10.1016/j.jestch.2017.08.002, 2017.

[11]. Jing W., Min-Xu L., Lei Z., Wei C., Ningxu L., Li-Hua H., *Effect of welding process on the microstructure and properties of dissimilar weld joints between low alloy steel and duplex stainless steel*, Int. J. Min. Met. Mater., 19 (6), p. 518-524, DOI: 10.1007/s12613-012-0589-z, 2012.

[12]. Mirsalehi S. E., Ahmadi M., *Investigation on microstructure, mechanical properties and corrosion behavior of AISI 316L stainless steel to ASTM A335-P11 low alloy steel*

dissimilar welding joints, Mater. High Temp., 32, p. 627-635, DOI: doi.org/10.1179/1878641315Y.0000000009, 2015.

[13]. Dev S., Devendranath Ramkumar K., Arivazhagan N., Rajendran R., *Investigations on the microstructure and mechanical properties of dissimilar welds of inconel 718 and sulphur rich martensitic stainless steel, AISI 416*, J. Manuf. Process., 32, p. 685-698, 2018.

[14]. Kurt A., Uygur I., Paylasan U., *Effect of friction welding parameters on mechanical and microstructural properties of dissimilar AISI 1010-ASTM B22 joints*, Welding Journal, 90 (5), p. 102-106, 2011.

[15]. Albert S. K., Das C. R., Shiju S., Mastanaiah P., Patel M., Bhaduri A. K., Jayakumar T., Murthy C. V. S., Rajendra K., *Mechanical properties of similar and dissimilar weldments of RAFMS and AISI 316L (N) SS prepared by electron beam welding process*, Fusion Eng. Des., 89, p. 1605-1610, DOI: doi.org/10.1016/j.fusengdes.2014.04.063, 2014.

[16]. Di H., Sun Q., Wang X., Li J., *Microstructure and proprieties in dissimilar/ similar weld joints between DP780 and DP980 steels processed by fiber laser welding*, J. Mat. Sci. Technol., 33, p. 1561-1571, 2017.

[17]. ***, *Non-destructive Testing, classification notes No. 7*, Det Norske Veritas AS, March 2012.

[18]. Halmshaw R., *Introduction to the Non-Destructive Testing of Welded Joints*, Second Edition, Abington Publishing, 2006.

[19]. Oral Büyüköztürk, Mehmet Ali Taşdemir, *Nondestructive Testing of Materials and Structures*, Springer Science & Business Media, 2012.

[20]. ***, *SR EN 10025 - 2 - Hot rolled products of structural steels - Part 2: Technical conditions for non-alloy structural steels*, 2004.

[21]. ***, *SR EN 10088-2 - Stainless steels - Part 2: Technical delivery conditions for sheet/plate and strip of corrosion resisting steels for general purposes*, 2015.

[22]. ***, *SR EN ISO 17633-A - Welding consumables - Tubular cored electrodes and rods for gas shielded and non-gas shielded metal arc welding of stainless and heat-resisting steels – Classification*, 2010.

THE ANNALS OF "DUNAREA DE JOS" UNIVERSITY OF GALATI
FASCICLE IX. METALLURGY AND MATERIALS SCIENCE
No. 1 - 2021, ISSN 2668-4748; e-ISSN 2668-4756
Article DOI: https://doi.org/10.35219/mms.2021.1.04

STRUCTURAL CHANGES OF NITROGEN FERRITE AFTER AGING IN TEMPERATURE INTERVAL UP TO 100 °C

Tatyana MECHKAROVA, Yaroslav ARGIROV, Daniela SPASOVA, Aneliya STOYANOVA
Technical University of Varna, Bulgaria
e-mail: tatqna13@abv.bg

ABSTRACT

This paper aims to determine the extent of aging of nitrogen ferrite at temperatures below 100 °C and the structural and strength changes that occur in the process. The tests are carried out on samples of technically pure iron (Armco). The specimens are pre-deformed by tension and re-crystallisation heating to achieve a large-grain ferrite structure. A large-grained structure has been chosen to more accurately track the change in micro-hardness of the individual grains during the aging process. Nitric ferrite results from gas carbonitriding and subsequent hardening. Upon hardening, the samples are stored in a refrigerator, and then the surface layer formed is removed through electrochemical corrosion. Afterwards, aging heat treatment at temperatures below 100 °C is undertaken. After the aging process, micro-hardness of the individual grains is examined and X-ray structural analysis is performed.

KEYWORDS: nitric ferrite, aging, gas carbonitriding, micro-hardness, X-ray structural analysis

1. Introduction

The aging tendency of nitric ferrite is recognized in literature [1-5]. This is caused by the high solubility of nitrogen in α-Fe (0.11%) at nitriding temperature and its change during the cooling process, reaching up to 0.04 % at 20 °C [6-9]. Most of the research on the aging of nitric ferrite is undertaken at aging temperature of 100 °C, at which much of the phase changes occur. These phase changes consist in the continuous release of iron nitrites of the type $Fe_{16}N_2$ (α) and Fe_4N(γ'). The first $Fe_{16}N_2$ (α) is formed at lower temperatures and its orientation is dependent on the α matrix, and the second Fe_4N(γ') at higher temperatures (>200 °C) is characterized by larger dimensions and unspecified orientation in the matrix [1-5].

The described aging modes lead to a decrease in the strength of the satiated nitric ferrite and are not able to use the strengthening potential of the hardened state of the ferrite phase [1-5].

It is obvious that at the basis of these substructural changes of the ferrite phase lies the release of α"- nitride ($Fe_{16}N_2$) and the rupture of its coherent connection to the matrix [6-8].

The α"- phase has a multi-atomic large crystal cell with parameters a = 5.72 Å and c = 6.29 Å [6-10], which coherently interacts with the body-centred cubic unit cell of the ferrite along the plane (100) [6-8].

During slow cooling after gas carbonitriding in the diffusion zone, the ferrite crystals release the nitrogen dissolved in them until reaching an equilibrium along the saturation line changing the concentration of 0.11÷0.01%. The nitrogen released is in the form of γ' nitride, which constitutes an independent phase and follows the reaction $\alpha N \rightarrow \alpha N + \gamma'$. The shape in which the γ' is observed is needle-like and equiaxed in the ferrite crystals. On cooling in environments where the period after gas carbonitriding is insufficient for secondary releases, a supersaturated αN solid solution is formed in the diffusion zone. The soluble component is dissolved in the octahedral cavities of the body-centred cubic unit cell, fills the point defects in the structure (vacancies), and groups around the dislocation nodes as well. This requires the cooling of the test samples to be carried out in water [9-15].

Reheating activates the dissolved nitrogen and the system's tendency to minimize the amount of free energy leads to its more favourable arrangement,

THE ANNALS OF "DUNAREA DE JOS" UNIVERSITY OF GALATI
FASCICLE IX. METALLURGY AND MATERIALS SCIENCE
Nº. 1 - 2021, ISSN 2668-4748; e-ISSN 2668-4756
Article DOI: https://doi.org/10.35219/mms.2021.1.04

bringing the structure to a more equilibrium state. The changes occurring in the structure during reheating may be recorded:

- Changes in the integral area of the X-ray line, as a consequence of structural micro tensions (II genus), defects in the arrangement, blockage in the crystal.
- Changes in the mechanical characteristics (hardness, strength).
- Microstructural changes – decoration of the ferrite crystals with subsequent secondary separation is registered.

The purpose of the study is to determine the possibility for strengthening the diffusion zone after reheating the carbonitriding iron materials with ferrite structure, and to identify optimal technological modes after reheating, gas carbonitriding temperature, heating temperature -t_{aging}, reheating time - τ_{aging}.

2. Experimental study

2.1. Preparation of experiment samples

The tests were carried out on cut samples of technically pure iron (Armco) [18-20] measuring 40x15x2 mm. The samples are deformed by a tensile test machine with a deformation rate of ε = 16%, and then re-crystallisation heated at 700 °C for 2 hours, achieving a large-grain ferrite structure with an average ferrite grain size $\bar{I}$ = 105 μm. Nitric ferrite is obtained after gas carbonitriding in the following mode:

- low temperature saturation:

$$t = 570\ ^oC,$$
$$\frac{NH_3}{CO_2} = \frac{1500^l_h}{200^l_h},$$
$$\tau = 3\ h$$

- cooling in water.

The hardening of the samples is carried out in water and after that they are stored in a refrigeration chamber. Since on the surface of the samples there is a carbonitride zone consisting of ε-carbonitride, this layer is removed by electrochemical corrosion to allow for conducting X-ray structural studies of the ferrite phase. The aging is carried out in a laboratory chamber furnace with a fan for effecting convective heat exchange within the volume of the chamber.

Table 1 shows the aging regimes studied and Fig. 1 illustrates the thermal treatment cyclorama of the samples.

Table 1. *The aging regimes*

T	Heating time, min									
°C	5	10	20	40	60	90	120	140	180	400
60	*		*	*	*		*	*	*	*
80	*		*	*	*	*	*	*	*	*
100		*	*	*	*		*	*	*	*

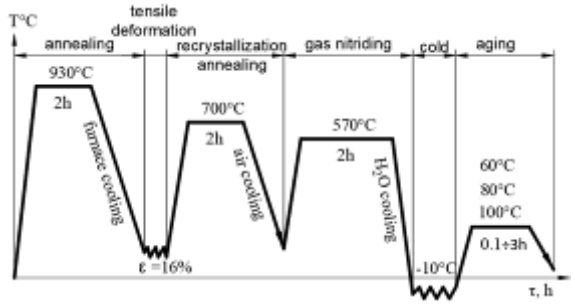

Fig. 1. *The thermal treatment cyclorama of the samples*

2.2. Methodology of metallographic tests and X - ray diffraction analysis

The determination of the crystals size in the different technological modes is carried out using a specialized "Epiquant" metallographic microscope.

The experiments are conducted using standard metallographic methods to monitor thin gradient layers. The transverse surface of the sample is observed, with the sample pressed with metal clamps and thin foil placed on the frontal surfaces. The purpose of the observation is to trace the secondary release on the cut ferrite grains. For this purpose, a polarized light observation methodology is used. Fine dispersion releases require greater optical magnification, which necessitates the use of immersion optics.

A standard methodology for an X-ray graphic recording is applied to perform the X-ray analysis using the U.S.-50IM device. The set does not allow digital capture of the profile obtained. This requires the use of the graphical programming product "Bytescout Graph Digitizer Scout" enabling the conversion of graphical results into digital Fig. 2. The graphs corresponding to the other aging temperatures are constructed in the same way.

THE ANNALS OF "DUNAREA DE JOS" UNIVERSITY OF GALATI
FASCICLE IX. METALLURGY AND MATERIALS SCIENCE
Nº. 1 - 2021, ISSN 2668-4748; e-ISSN 2668-4756
Article DOI: https://doi.org/10.35219/mms.2021.1.04

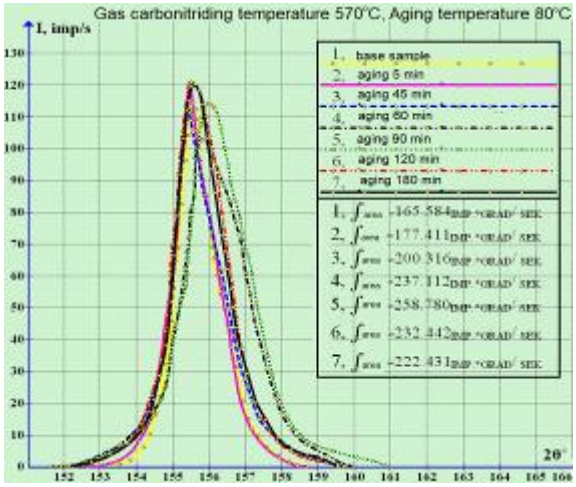

Fig. 2. *Areas of X-ray lines (211) in nitrogen ferrite after gas carbonitriding at 570 °C and aging at 80 °C*

3. Results of the experimental study

The article does not address issues related to the mechanism of aging, but it sets out the results of the kinetic changes of the X-ray broadening of the lines of the diffraction maximums of ferrite, as well as the micro-hardness.

3.1. Results of metallographic tests

At high temperature (100 °C) and duration of aging, a characteristic emphasis on the relief of the ferrite structure is noted, evenly the entire volume of grains observed by special metallographic methods (immersion optics, interfering contrast and polarization) Fig. 3.

Figure 3a, b shows the initial structures after gas carbonitriding. The difference between the two samples refers to the manner of cooling (fast and slow). With slow cooling, the system is in equilibrium throughout the whole cooling period, accompanied by the release of the γ' phase and thus maintaining an equilibrium concentration of the basic matrix αN. The release has a needle-like form. The stable γ'-phase Fe_4N cumulates on the plane (012) of the matrix and arranges at an acute angle.

In the microstructure characterized by its nonequilibrium state, Fig. 3a, resulting from the high cooling rate and the formation of a supersaturated solid solution, the crystals are visibly homogeneous, with no apparent relief.

Most of the studies of nitrogen ferrite have been performed at aging temperatures of above 100 °C, at which significant phase changes take place. These phase changes consist in the continuous release of iron nitrides of the type $Fe_{16}N_2$ (α") and Fe_4N (γ'). The former is formed at lower temperatures and is orientation dependent on the α-matrix, and the latter is formed at higher temperatures (>200 °C), and is characterized by its larger dimensions and indeterminate orientation in the matrix.

These aging modes lead to a continuous loss of strength (softening) of the supersaturated nitrogen ferrite and are not able to make use of the hardening potential, which is generally contained in the hardened state of the ferrite phase.

The decomposition of α saturated solid solution follows the general laws of phase transformations. Initially, at low aging temperatures, Cottrell atmospheres are formed. As the retention time increases (temperature rise to 60÷150 °C), lamellar microstructures of the metastable α" - $Fe_{16}N_2$ phase are developed, coherently connected to the matrix. Upon the release of the metastable $Fe_{16}N_2$ nitride, a pronounced predominant orientation of its lamellae in the direction of plane (100) of the original nitrogen ferrite lattice is observed. In the initial stage of aging, the length of the lamellar microstructures is 100-200 Å and increases in the aging process to 500-5000 Å. Due to the obviously small size and the lack of boundaries in the individual zones formation, Fig. 3c, d, e, they cannot be observed as defined needle-like crystals, but only as matrix αN relief.

Upon breaking the coherent bond with the main matrix, the precipitates are observed as needle-like crystals, similar to the slowly cooled structures, Fig. 3 b.

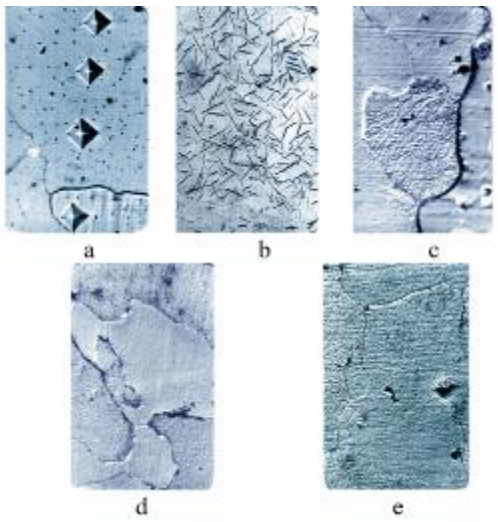

Fig. 3. *Microstructure in the diffusion zone after gas carbonitriding, t = 570 °C, τ = 3 h x 500*
a/ gas carbonitriding → cooling in H_2O,
b/ gas carbonitriding → slowly cooled,
c/ gas carbonitriding → cooling in H_2O → t_{aging} = 80 °C, τ_{aging} = 60 min,

THE ANNALS OF "DUNAREA DE JOS" UNIVERSITY OF GALATI
FASCICLE IX. METALLURGY AND MATERIALS SCIENCE
No. 1 - 2021, ISSN 2668-4748; e-ISSN 2668-4756
Article DOI: https://doi.org/10.35219/mms.2021.1.04

d/ gas carbonitriding → cooling in H_2O → t_{aging} = 80 °C, τ_{aging} = 120 min,
e/ gas carbonitriding → cooling in H_2O → t_{aging} = 100 °C, τ_{aging} = 60 min

3.2. X - ray diffraction analysis

X-ray examinations were carried out of the line (211) of nitrogen ferrite, which is a major phase in the diffusion zone. The main data that can be obtained from the X-ray structural analysis is a study of the zones of nitrogen atoms formed in the ferrite matrix, leading to the deformation of one of the atomic planes of the solvent. This type of micro tensions of the crystal cell can be determined by changing the width of the X-ray line. Table 2 presents the results obtained from the X-ray lines filmed (211) of the αN phase and the specified integral areas for the different aging modes.

The results of the X-ray examinations are illustrated in Table 2, from which it appears that all the three output samples have different integral areas. Therefore, analyses based on absolute values are not entirely reliable.

Real analyses are obtained using relative values (1). When using relative values, for the integrated area we use $\int_{i,j}$. Index (i) means t_{aging}, °C; j means τ_{aging}, min.

$$\int i,j(relative) = \frac{\int base\ sample - \int i,j}{\int base\ sampe} \quad .. (1)$$

Table 2. *Integral area of the X-ray line (211)*

Time aging	T °C aging		
τ_{min}	τ = 60 °C	τ = 80 °C	τ = 100 °C
base sample	207.524	165.584	188.685
5	213.045	177.411	
10			189.599
20	217.995	200.316	190.497
40	220.137	237.112	197.993
60	228.643	258.780	200.218
90		232.442	
120	228.952	222.431	167.421
180	231.164	200.316	164.231
400	188.810	184.216	158.349

(I, imp/sek) in nitride ferrite t_{gcn} = 570 °C

Fig. 4 indicates that the maximum value of the integral area in the αN phase aging is observed at an aging temperature of about 80 °C and time τ_{aging} = 90÷120 min.

Fig. 4 combines the results of the radiographs for all temperatures and aging times.

Where the red region of isolines shows the extremum of the relative value of the X-ray line widening calculated by formula 1 according to the technological parameters of time and temperature set. The absolute broadening of the baseline (Fig. 2 sample 1) is taken account of in the calculations of the relative values of all X-ray lines.

As the time and temperature of the aging increase, we can note a decrease in the area of the X-ray line. Perhaps this is due to the system need to move to a more equilibrium state, which is characterized by a partial rupture of the coherent link between the matrix (αN) and the zone of dissolved nitrogen atoms formed in the aging process. The aspiration is to build a new γ' phase through raising the temperature. The studies performed proved a certain instability of this coherence, that is, it occurs under strictly defined conditions and is quickly destroyed. Perhaps this is due to the small similarity of the crystal grids of α" and α phases, the difference in concentrations and similarity of the cell of α" and γ'- nitrite, which determines the rapid transition of α" to γ'-nitrite. The strictly plastic shape and orientation of the α"-crystals, which are particularly well manifested in aging above 180 °C, confirm this crystallographic difference between α" and α- phases.

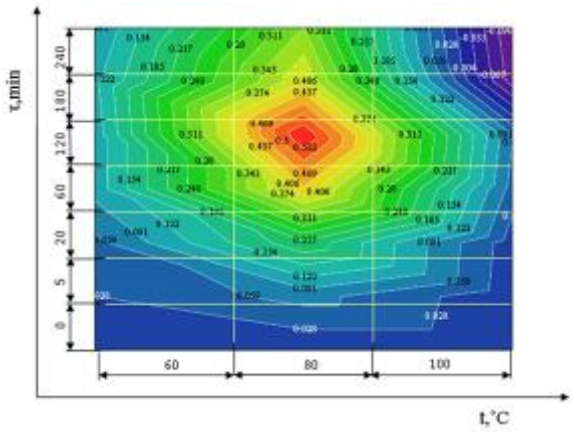

Fig. 4. *Change in the relative integral area of the X-ray line (211) at αn, depending on the temperature (570 °C) and aging time at gas carbonitriding*

3.3. Microhardness tests

As a result of the aging deformation of the crystal lattice, which is evident from the X-ray line broadening Fig. 4, a change in the microhardness Fig. 5, also occurs, which is indicative of the overall change in the mechanical properties in the diffusion region [16-19].

The results obtained are used for the determination of the change in microhardness with the change in the technological parameters temperature and aging time, Fig. 5. The maximum

THE ANNALS OF "DUNAREA DE JOS" UNIVERSITY OF GALATI
FASCICLE IX. METALLURGY AND MATERIALS SCIENCE
N°. 1 - 2021, ISSN 2668-4748; e-ISSN 2668-4756
Article DOI: https://doi.org/10.35219/mms.2021.1.04

hardness of 470 HV recorded along the blue line corresponds to an aging mode of t = 80 °C and τ = 90 min, which is associated with the reported line broadening extremum in Fig. 4. For comparison, the initial hardness in the diffusion zone of nitrogen ferrite is in the range of 250-320 HV [16-19].

The elastic deformation of the ferrite matrix cell, as indicated by the increased X-ray broadening, is the cause for an increase in the hardness of the aging matrix. This change in the hardness of the nitrogen ferrite in the aging process, shown in Fig. 5, is consistent with the variation of the X-ray broadening. It is notable that the initial state of the different samples is characterized by different hardness. This difference is due to the fact that each sample has a certain gradient of nitrogen concentration, and respectively of nitrogen ferrite concentration, in the diffusion layer. Although hardness is determined at the same distance from the surface (40 μm) for all samples, some deviation in the degree of saturation of the individual samples can be expected. In addition, the change in micro hardness is measured in separate ferrite grains, therefore it is possible that the crystallographic orientation may also have a certain influence.

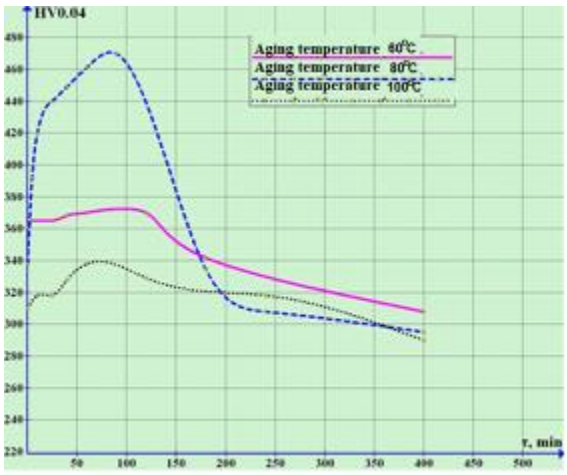

Fig. 5. *Microhardness at constant depth in the diffusion zone after gas carbonitriding at t = 570 °C, depending on temperature and aging time*

A similar effect is perceived in the determination and analysis of X-ray broadening. Notwithstanding these initial deviations, a maximum in hardness is obviously observed in the aging process, undoubtedly indicating an increase in the strength of nitric ferrite after aging in a narrow temperature range of 80-90 °C. At lower temperatures, the activation of nitrogen atoms in the saturated ferrite is still insufficient for their segregation and the formation of corresponding precipitates. Deviations in X-ray broadening and hardness after aging at 60 °C are negligible. Aging at 100 °C also has a strengthening effect, but not as pronounced as after aging at 80 °C. The maximums for these temperatures are drawn towards smaller durations (times), which is natural due to the greater diffusion mobility of nitrogen atoms in ferrites.

4. Conclusion

In conclusion, it should be noted that the saturated nitrogen ferrite formed has a tendency to age after low temperature gas carbonitriding, its strength indicating the greater increase in a temperature range of 80-90 °C (470 HV) when retained at these temperatures from 40 to 70 minutes. For aging processes, these optimal temperature ranges and aging time turn out to be too narrow, due to the high sensitivity of the coherent interaction between the nitride phase (α") and the ferrite matrix (α).

References

[1]. Bielawski J., Baranowska J., Szczecinski K., *Protective Nitrided Layers on Ferite-Austenite Chromiun Steel*, Materials Science, vol. 11, no. 3, p. 221-225, 2005.
[2]. Callister W. D., *Materials Science and Engineering: An Introduction*, 7th ed., John Wiley & Sons, Inc., United States of America, 2007.
[3]. Christiansen T., Somers M. A. J., *Characterisation of Low Temperature Surface Hardened Stainless Steel*, Struers Journal of Materialography, p. 2-17, 9/2006.
[4]. Grachov S. V., Baras V. R., *Thermomechanical treatment of age hardening austenitic steels*, Ind. Heat., vol. 47, no. 10, p. 20-23, 1980.
[5]. Kubota S., Xia Y., Tomota Y., *Work-hardening Behavior and Evolution of Dislocation-microstructures in High-nitrogen Bearing Austenitic Steels*, ISIJ International, 38(5), 474, 1998.
[6]. Llewellyn D. T., Hudd R. C., *Steels: Metallurgy and applications*, 3rd Edition, Butterworth-Heinemann, 400, 1998.
[7]. ***, *Handbook: Steel and alloys grades and properties*, http://www.steelnumber.com/en/steel_composition_eu.php?name_id=18.
[8]. Marchev K., Landis M., Valletio R., Cooper C. V., Giessen B. C., *The m – Phase Layer on Ion-Nitrided Austenitic Stainless Steel (III) An Expitaxial Relationship Between the m – Phase and the γ Parent Phase and a Review the m – Phase and the γ Parent Phase and a Review of Structural Identifications of This Phase*, Surface and Coatings Technology, 116-119, p. 184-188, 1999.
[9]. Peralta P. D., *Dislocation structure and cyclic plasticity*, Encycl. Mater. Sci. Technol., Elsevier, p. 2222-2235, 2001.
[10]. Podgomik B., Vizintin J., Ronkainen H., Holmberg K., *Friction and Wear Properties of DLC-coated Plasma Nitrided Steel in Unidirectional and reciprocating Sliding*, Thin Solid Films 377-378, p. 254-260, 2000.
[11]. Podgornik B., Vizintin J., Wanstrand O., Larsson M., Hogmark S., Ronkainen H., Holmberg K., *Tribological Properties of Plasma Nitrided and Hard Coated AISI 4140 Steel*, Wear, 249, p. 254-259, 2001.
[12]. Sun Y., Li X., Bel T., *Structural Characteristics of Low Temperature Plasma Carburised Austenitic Stainless Steel*, Materials Science and Technology, vol. 15, p. 117l-1178, October 1999.
[13]. Haasen P., *Physical metallurgy. Cambridge*, New York: Cambridge University Press, 1978.

[14]. Samuel J., *Introduction to materials science course manual*, Madison, Wisconsin: University of Wisconsin-Madison, 2009.
[15]. Leslie W. C., *The physical metallurgy of steels*, Washington: Hempisphere Pub. Corp., New York: McGraw-Hill, ISBN 0070377804, 1981.
[16]. Chinn R. L., *Hardness, bearings, and the Rockwells*, Advanced Materials & Processes, 167 (10), p. 29-31, 2009.
[17]. Davis J. R., *Surface hardening of steels: Understanding the basics*, Materials Park, OH: ASM International, 2002.
[18]. Dieter George E., *Mechanical Metallurgy*, SI Metric Adaptation, Maidenhead, UK: McGraw-Hill Education, ISBN 0-07-100406-8, 1989.
[19]. Revankar G., *Introduction to hardness testing*, Mechanical testing and evaluation, ASM Online, vol. 8, 2003.

THE ANNALS OF "DUNAREA DE JOS" UNIVERSITY OF GALATI
FASCICLE IX. METALLURGY AND MATERIALS SCIENCE
Nº. 1 - 2021, ISSN 2668-4748; e-ISSN 2668-4756
Article DOI: https://doi.org/10.35219/mms.2021.1.05

POLY(3-HYDROXYBUTYRATE-CO-3-HYDROXYVALERATE) BASED INORGANIC CONSOLIDATE FOR FIRWOOD PRESERVATION

Mădălina Elena DAVID[1,2], Ramona Marina GRIGORESCU[1], Lorena IANCU[1], Elena Ramona ANDREI[1], Rodica-Mariana ION[1,2]

[1] "Evaluation and Conservation of Cultural Heritage" Research Group, National Institute for Research and Development in Chemistry and Petrochemistry, ICECHIM, 202 Splaiul Independentei, Bucharest, Romania
[2] Materials Engineering Department, Valahia University, 13th Aleey Sinaia, Targoviste, Romania
e-mail: madalina.e.david@gmail.com

ABSTRACT

The aim of this study was to address one of the major challenges of the conservation state of wooden artifacts or artworks namely, the preservation and restoration of wood surfaces. The factors involved in the deterioration of wood are mainly the external factors such as fire, low temperature and microbiological agents, which induce some degradation processes in wood, identified by discoloration, fragility and unsightly appearance. In this study, biodegradable materials based on poly(3-hydroxybutyrate-co-3-hydroxyvalerate) (PHBHV) and composites based on PHBHV and particles (zinc oxide (ZnO), carbonated hydroxyapatite (CHAp) and its metallic derivatives with silver (AgCHAp) and strontium (SrCHAp) were applied on firwood specimens in order to investigate their consolidation capacity. Colorimetric measurements have confirmed that the chosen treatments did not change the colour of the natural wood. The hardness test revealed that the consolidation system increases the mechanical properties of the samples. The used treatments confer a strong hydrophobic character which prevents exfoliation of the wood samples, as confirmed by the performed water absorption test.

KEYWORDS: poly(3-hydroxybutyrate-co-3-hydroxyvalerate), zinc oxide, carbonated hydroxyapatite, preservation, firwood

1. Introduction

Wood is one of the oldest materials in the humanity history being used for thousands of years as a construction material, for furniture, fuel and paper. It is an organic material and presents a porous and fibrous structure which supports a continuous degradation and deterioration processes by weathering and various organisms' action [1, 2]. Due to the hygroscopic nature of wood [3], this material is subjected frequently to several deterioration processes, like the loss of mechanical strength through moisture absorption, a higher degree of surface roughness and cracking on UV exposure [4-7], so the treatments that preserve the wood are highly needed.

In order to prevent the wood degradation processes, the researchers have tried to use some conservation treatments with different compatible materials [1, 8, 9]. In the last several years, biodegradable polymeric materials have been used in order to protect the wooden artifacts or artworks. Polyhydroxyalkanoates (PHAs) are a class of biodegradable polymers under ambient conditions that can be intracellularly synthesized by a range of bacteria and archaea from renewable/waste resources [10, 11]. Among all the PHAs family, poly(3-hydroxybutyrate) (PHB) and its copolymer poly(3-hydroxybutyrate-co-3-hydroxyvalerate) (PHBHV) are the most common used in various applications and currently, these materials have been tested in order to investigate their potential in wood protection [10, 12]. In the last years, PHBHV has received great attention from different research labs. For example, Chan C.M. and co-workers investigated the effects of natural weathering on the physical and mechanical properties of biodegradable composites based on PHBHV and wood flour (WF). Composite samples with three

THE ANNALS OF "DUNAREA DE JOS" UNIVERSITY OF GALATI
FASCICLE IX. METALLURGY AND MATERIALS SCIENCE
Nº. 1 - 2021, ISSN 2668-4748; e-ISSN 2668-4756
Article DOI: https://doi.org/10.35219/mms.2021.1.05

different WF contents (0, 20 and 50 wt%) were placed on an outdoor inclined rack for 12 months. It was observed that neat PHBHV and the 20% WF samples showed little loss in mechanical properties over the 12-month period compared 50% WF. A less dense fungal cell network and lower dry weight loss values were observed on the PHBHV 20%WF composite when compared to 50% WF. At lower wood content, the PHBHV matrix acted as a barrier, partially encapsulating the wood particles. A lower relative abundance of fungi was shown in all PHBHV samples, suggesting that PHBHV does not promote fungal colonization relative to woody materials [10].

Also, in the last years it has been demonstrated that both micro and nanomaterials plays an important role in cultural heritage, new and efficient systems being obtained and successfully tested on wood, such as metallic oxides (ZnO, TiO_2, CuO) [13-16], metallic nanoparticles (Ag) [17] and recently, hydroxyapatite (HAp) ($Ca_{10}(PO_4)_6(OH)_2$: Ca/P = 1.67) [1, 18-20]. By replacing the phosphate and/or the hydroxyl groups from the apatite structure with carbonate groups, carbonated hydroxyapatite can be obtained and its mechanical and antimicrobial properties can be enhanced by the insertion of metallic ions that replace calcium. With a similar structure compared with HAp and better characteristics, CHAp can improve the wood resistance to environmental impact [18].

This paper aims to obtain new composite coatings based on PHBHV and inorganic consolidants, such as ZnO micronized particles [16], carbonated hydroxyapatite (CHAp) and CHAp derivatives with different metal ions (Ag^+, Sr^{2+}) [18]. The obtained solutions were tested on firwood samples, in order to investigate the potential of new solutions for artifacts preservation.

2. Materials and methods

Wooden materials:

In this study, firwood specimens (7x3x1 cm) without knots were treated by brushing three times on all sides with the solutions based on PHBHV and particles.

Solutions preparation:

PHBHV powder with a molecular weight of 67,000 g/mole containing 2% hydroxyvalerate (Good Fellow) was used as composites matrix. A solution of PHBHV (1 wt%) in chloroform was prepared by heating the solution for 6 h at 60 °C under magnetic stirring [21]. The PHBHV/ZnO solution was obtained according to Fig. 1.

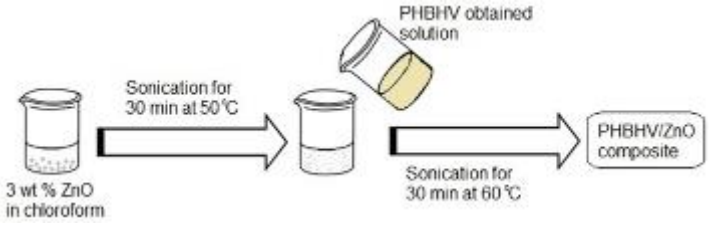

Fig. 1. *Schematic diagram of the procedure for the preparation of the PHBHV/ZnO composite*

CHAp and its metallic derivatives (Ag, Sr) nanoparticles (NPs) have been prepared by a nanoemulsion technique described in our previous study [18] and then used in order to obtain PHBHV/CHAp NPs, PHBHV/AgCHAp NPs and PHBHV/SrCHAp NPs solutions. The solutions were obtained in the same way as in the case of PHBHV/ZnO solution.

3. Characterization methods

Colorimetric Measurements have been recorded with a CR-410 colorimeter (Konica Minolta, Tokyo, Japan). The measurements were expressed following the CIE L* a* b* systems [22]. The total color differences ΔE_{xfinal} was estimated according to EN 15886 [23] and ASTM 2244 [24], and calculated using formula (1).

$$\Delta E_{xfinal} = [\Delta L^2 + \Delta a^2 + \Delta b^2]^{1/2} \quad (1)$$

where, ΔL is the difference in lightness ($\Delta L = L_{treated\ material} - L_{control}$), Δa is the chromatic deviation of the a coordinates (ranges in value from +60 (red) to -60 (green), $\Delta a = a_{treated\ material} - a_{control}$) and Δb is chromatic deviation of the b coordinates (ranges in value from +60 (yellow) to -60 (blue), $\Delta b = b_{treated\ material} - b_{control}$).

The colorimetric investigation has been recorded for the untreated and treated specimens with PHBHV, PHBHV / CHAp, PHBHV / AgCHAp, PHBHV / SrCHAp and PHBHV / ZnO solution applied by brushing on the surfaces of firwood specimens.

Gloss Measurements have been performed according to ISO 2813 [25] with 3nh glossmeter, model HG268. This technique has been used in order to investigate the specular reflection gloss of the

THE ANNALS OF "DUNAREA DE JOS" UNIVERSITY OF GALATI
FASCICLE IX. METALLURGY AND MATERIALS SCIENCE
Nº. 1 - 2021, ISSN 2668-4748; e-ISSN 2668-4756
Article DOI: https://doi.org/10.35219/mms.2021.1.05

surfaces. The glossmetric investigation was recorded for untreated and treated samples.

Mechanical Testing Measurements have been recorded with a Silver Schmidt Hammer Proceq test hammer, type L-0.735 Nm impact energy, according to ASTM C805 [26]. The strength range of the Silver Schmidt test hammer is from 10-100 N/mm^2. For each sample, ten replicates in different places were recorded with the hammer positioned at 90º downward and the result (rebound number value) was calculated as the average of the readings.

Water Absorption Test offers information about the quantity of water absorbed by a material at room temperature. In the first step, all the samples have been dried in an oven for 8 hours at 40 ºC, this low drying temperature will prevent the deterioration of any organic substances employed in the case of treated samples. After drying, the samples were left at room temperature to cool, and then weighed (W1). Once being completely dried and the constant mass being recorded, the samples were placed in a tray filled with distilled water for 24 hours. Then the samples were removed from the water, wiped with a paper towel and weighed (W_2). The water absorption (WA) was calculated using formula (2).

$$WA = \frac{W_2 - W_1}{W_1} * 100 \quad (2)$$

Water Drop Absorption test measures the absorption time of a limited and definite amount of water by the surface of a material. In the first step, all the samples have been dried in an oven for 24 hours at 60 ºC, and then the samples were left at room temperature to cool. A burette (filled with distilled water) was placed at a distance of 1 cm from the sample surface and then 1 mL of water was dropped onto the surface of the sample. The time required for the total absorption of the water in the case of all samples was investigated.

4. Results and discussion

In order to investigate the ability of the new materials to consolidate the wood, the first step was to determinate the variation of chromatic parameters before and after the application of the treatment (Fig. 2 (a) and (b)). Chromatic parameters are important because the applied treatment must not significantly change the original colour of the object. Compared with Control (untreated wood) it can be observed that all the treated samples present very low differences in the case of Δa_x coordinate, that indicated sample reddening (Fig. 2 (a)). In the yellow-blue interval (Δb_x) some changes in colour can be observed (indicating yellowing), mostly in the case of the samples where particles are present, but these differences of colour are below 3, what means that the samples colour is stable. Also, the total colour differences ΔE_x confirms that the surface of the samples treated with PHBHV-ZnO and PHBHV-AgCHAp are the most light in colour, due to the presence of the particles. These differences are acceptable because the values are below 3 what means that consolidate doesn't influence the colour of the samples. In the case of PHBHV-CHAp and PHBHV-SrCHAp, ΔE_x ranges from 1.5 to 3.0, what means that the difference is barely noticeable on the surface, and for PHBHV the difference is slightly perceptible [27]. The graphic representation of the colour of the samples (Fig. 2 (b)) confirms that the closest colour to the control samples are the samples treated with PHBHV and PHBHV-CHAp.

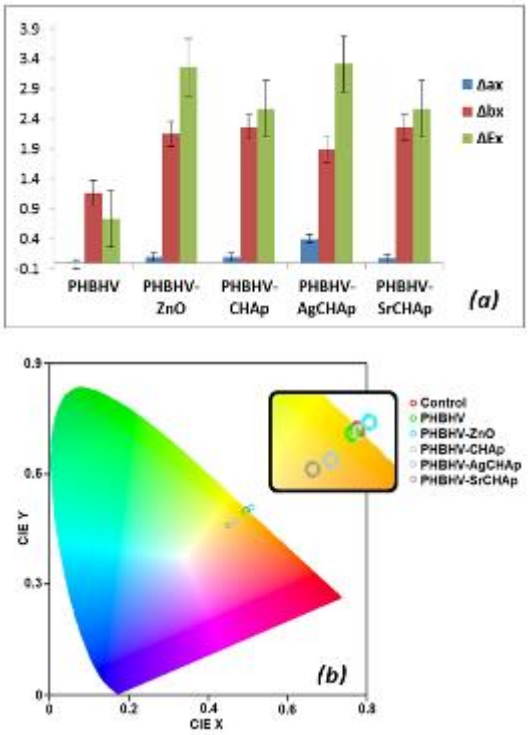

Fig. 2. *Chromatic parameters (a) and graphic representation of the colour of the samples in the CIE 1931 system (b) of the untreated and treated samples*

Gloss measurements (GU) were carried out in order to investigate the changes in the texture of the samples (changes in reflecting properties over the surface). It can be observed (Fig. 3) that all the samples presented a low gloss (values under 10 gloss units-GU), and when the treatment is applied the gloss of the sample present a small decrease, mostly in the case of the samples treated with the solution based on PHBHV-ZnO.

THE ANNALS OF "DUNAREA DE JOS" UNIVERSITY OF GALATI
FASCICLE IX. METALLURGY AND MATERIALS SCIENCE
Nº. 1 - 2021, ISSN 2668-4748; e-ISSN 2668-4756
Article DOI: https://doi.org/10.35219/mms.2021.1.05

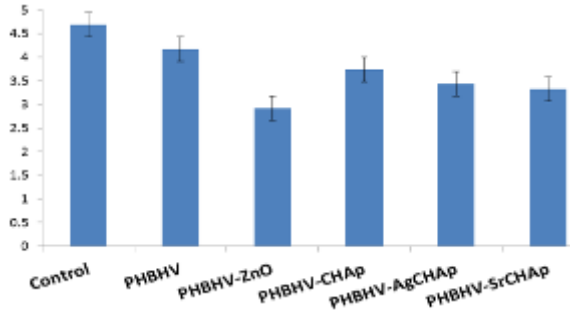

Fig. 3. *Glossmetric measurements of the untreated and treated samples*

Mechanical measurements were recording with Silver Schmidt test hammer in order to evaluate the mechanical properties of the wood samples. The rebound number measurements for the untreated and treated samples are shown in Fig. 4. Compared to control, all the treated samples presented an increased rebound number. The sample treated with PHBHV-CHAp NPs presents the highest values. The addition of the particles on the samples surface enhanced the durability of wood compared to the untreated wood, due to the role of the particles in reinforcing the wood [1].

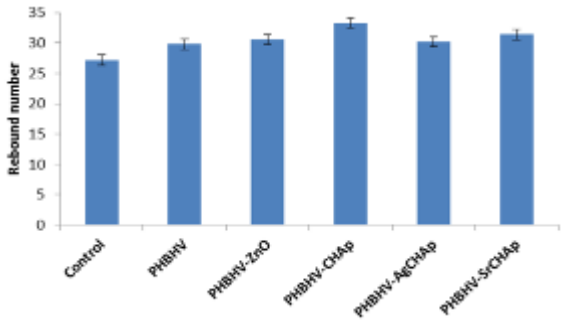

Fig. 4. *Mechanical strength of the untreated and treated samples*

Wood is a hydrophilic material and adsorbs moisture when it is exposed to real conditions. Water absorption test (Fig. 5) was carried out in order to investigate the quantity of water absorbed by a material under specified conditions. Compared with control it can be observed that the treated samples present a lower absorption capacity (the untreated sample has absorbed almost a double amount of water compared to treated samples), what proves the efficiently of the treatment.

Fig. 6 presents the aspect of untreated and treated sample, which confirms that treatment prevents exfoliation of the sample (a very common phenomenon in the case of wood found in nature).

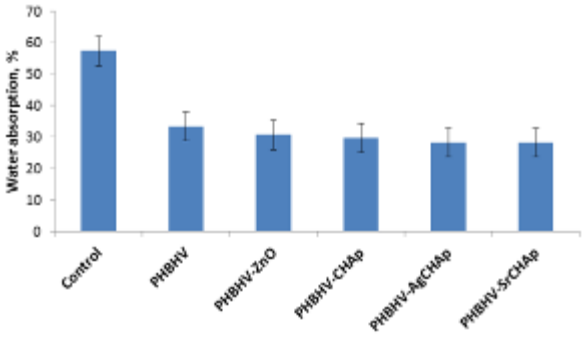

Fig. 5. *Water absorption test of untreated and treated firwood specimens*

Fig. 6. *The aspect of the samples after water absorption test (24 hours in water)*

Fig. 7. *Water drop absorption at different times*

Once again, the hydrophobic character of the treated materials is confirmed by water drop absorption. After the drop touched the surface of the materials, in the case of control sample the drop adhered to the surface of the material, confirming its hydrophilicity (Fig. 7). While, in the case of the treated materials the drop did not adhere to the surface of the material, which means that after the treatment, the surface of the material has become hydrophobic. Also, the untreated wood has absorbed the drop after only 2 hours and after 8 hours the

sample was completely dried (Fig. 7 - control). In the case of the treated materials, the drop remains on the wood surfaces until it evaporates, after 8 hours ~70% of the drop was evaporated. After 24 hours, the drop was completely evaporated from the surface of the treated materials, so the treated samples maintained their hydrophobic character in time.

5. Conclusions

This study investigated the potential of biodegradable coatings based on PHBHV and particles, tested on the firwood samples, as a new solution for preservation of some wooden artifacts. The values obtained on colorimetric and gloss measurements have confirmed that all consolidates did not significantly influence the aspect of the samples. The hardness test reveals that the presence of the consolidating system increases the mechanical properties of the samples. The improvement of resistance was achieved for all the treated samples, mostly in the case of the samples treated with PHBHV-CHAp. The tests performed in order to investigate the absorption capacity of the samples confirmed that the used treatments confer a strong hydrophobic character to the samples, due to the fact that the drop was not absorbed by the material but evaporated in time from the surface samples. Also, by visual analysis it can be confirmed that the untreated sample presents a strong exfoliating behavior of the surface, compared to the treated sample. So, following these results it can be confirmed that the developed treatments for firwood protection are a good alternative to protect the wood-based materials found in nature.

Acknowledgments

This work was supported by a grant of the Romanian Ministry of Research and Innovation, CCCDI-UEFISCDI, project number PN-III-P1-1.2-PCCDI-2017-0476/51PCCDI/2018, within PNCDI III.

References

[1]. Ion R.-M., Nyokong T., Nwahara N., Suica-Bunghez I.-R., Iancu L., Teodorescu S., Dulama I. D., Stirbescu R. M., Gheboianu A., Grigorescu R. M., *Wood preservation with gold hydroxyapatite system*, Heritage Science, 6(1), p. 37, 2018.
[2]. Laks P., Heiden P. A., *Compositions and methods for wood preservation*, Google Patents, 2003.
[3]. Stark N., *Influence of moisture absorption on mechanical properties of wood flour-polypropylene composites*, Journal of Thermoplastic Composite Materials, 14(5), p. 421-432, 2001.
[4]. Tajvidi M., Najafi S. K., Moteei N., *Long-term water uptake behavior of natural fiber/polypropylene composites*, Journal of Applied Polymer Science, 99(5), p. 2199-2203, 2006.
[5]. Badji C., Soccalingame L., Garay H., Bergeret A., Bénézet J.-C., *Influence of weathering on visual and surface aspect of wood plastic composites: Correlation approach with mechanical properties and microstructure*, Polymer Degradation and Stability, 137, p. 162-172, 2017.
[6]. Fabiyi J. S., McDonald A. G., Wolcott M. P., Griffiths P. R., *Wood plastic composites weathering: Visual appearance and chemical changes*, Polymer Degradation and Stability, 93(8), p. 1405-1414, 2008.
[7]. La Mantia F. P., Morreale M., *Accelerated weathering of polypropylene/wood flour composites*, Polymer Degradation and Stability, 93(7), p. 1252-1258, 2008.
[8]. Teng T.-J., Arip M. N. M., Sudesh K., Nemoikina A., Jalaludin Z., Ng E.-P., Lee H.-L., *Conventional technology and nanotechnology in wood preservation: A review*, BioResources, 13(4), p. 9220-9252, 2018.
[9]. Morrell J. J., *Protection of wood-based materials*, Handbook of Environmental Degradation of Materials, Elsevier, p. 343-368, 2018.
[10]. Chan C. M., Pratt S., Halley P., Richardson D., Werker A., Laycock B., Vandi L.-J., *Mechanical and physical stability of polyhydroxyalkanoate (PHA)-based wood plastic composites (WPCs) under natural weathering*, Polymer Testing, 73, p. 214-221, 2019.
[11]. Grigore M. E., Grigorescu R. M., Iancu L., Ion R.-M., Zaharia C., Andrei E. R., *Methods of synthesis, properties and biomedical applications of polyhydroxyalkanoates: a review*, Journal of Biomaterials Science, Polymer Edition, 30(9), p. 695-712, 2019.
[12]. Radu I. C., Hudita A., Zaharia C., Galateanu B., Iovu H., Tanasa E. V., Georgiana Nitu S., Ginghina O., Negrei C., Tsatsakis A., Velonia K., Shtilman M., Costache M., *Poly(3-hydroxybutyrate-CO-3-hydroxyvalerate) PHBHV biocompatible nanocarriers for 5-FU delivery targeting colorectal cancer*, Drug Deliv., 26(1), p. 318-327, 2019.
[13]. Clausen C. A., Green F., Kartal S. N., *Weatherability and leach resistance of wood impregnated with nano-zinc oxide*, Nanoscale research letters, 5(9), p. 1464, 2010.
[14]. Rassam G., Abdi Y., Abdi A., *Deposition of TiO2 nano-particles on wood surfaces for UV and moisture protection*, Journal of Experimental Nanoscience, 7(4), p. 468-476, 2012.
[15]. Shiny K., Sundararaj R., Mamatha N., Lingappa B., *A new approach to wood protection: Preliminary study of biologically synthesized copper oxide nanoparticle formulation as an environmental friendly wood protectant against decay fungi and termites*, Maderas. Ciencia y tecnología, (AHEAD), 2019.
[16]. David M. E., Ion R.-M., Andrei E. R., Grigorescu R. M., Iancu L., Filipescu M. I., *Superhydrophobic Coatings Based on Cellulose Acetate for Pinewood Preservation*, Journal of Science and Arts, 1(50), p. 171-182, 2020.
[17]. Borges C. C., Tonoli G. H. D., Cruz T. M., Duarte P. J., Junqueira T. A., *Nanoparticles-Based Wood Preservatives: The Next Generation of Wood Protection?*, Cerne, 24(4), p. 397-407, 2018.
[18]. Ion R.-M., Iancu L., Vasilievici G., Grigore M. E., Andrei R. E., Radu G.-I., Grigorescu R. M., Teodorescu S., Bucurica I. A., Ion M.-L., *Ion-Substituted Carbonated Hydroxyapatite Coatings for Model Stone Samples*, Coatings, 9(4), p. 231, 2019.
[19]. Iancu L., Ion R.-M., Grigorescu R. M., David M. E., Ghiurea M., Vasilievici G., Stirbescu R. M., Dulama I. D., *Double Substituted Carbonated Hydroxyapatite for Stone Consolidation*, Journal of Science and Arts, 3(52), p. 713-730, 2020.
[20]. Ion R. M., Iancu L., David M. E., Grigorescu R. M., Trica B., Somoghi R., Vasile S. F., Dulama I. D., Gheboianu A. I., Tincu S., *Multi-Analytical Characterization of Corvins' Castle-Deserted Tower, Construction Materials and Conservation Tests*, Heritage, 3(3), p. 941-964, 2020.
[21]. Leimann F., Cardozo Filho L., Sayer C., Araújo P., *Poly (3-hydroxybutyrate-co-3-hydroxyvalerate) nanoparticles prepared by a miniemulsion/solvent evaporation technique: effect of phbv*

molar mass and concentration, Brazilian Journal of Chemical Engineering, 30(2), p. 369-377, 2013.

[22]. Ion R.-M., Iancu L., Grigorescu R.-M., Tincu S., Vasilievici G., Ion N., Bucurica I. A., Teodorescu S., Dulama I. D., Stirbescu R. M., *Arhaeometric investigations on ceramic materials from Hunedoara-the court area*, Journal of Science and Arts, 18(2), p. 471-480, 2018.

[23]. ***, *EN U 15886. Conservation of cultural property, Test methods. Colour measurements of surfaces*, 2010.

[24]. ***, *ASTM D 2244. Standard Practice for Calculation of Color Tolerances and Color Differences from Instrumentally Measured Color Coordinates, American Society for Testing and Materials*, West Conshohocken, PA, 2003.

[25]. ***, *ISO 2813: Paints and Varnishes-Determination of Gloss Value at 20 Degrees, 60 Degrees and 85 Degrees*, International Organization for Standardization, 2014.

[26]. Aydin F., Saribiyik M., *Correlation between Schmidt Hammer and destructive compressions testing for concretes in existing buildings*, Scientific Research and Essays, 5(13), p. 1644-1648, 2010.

[27]. Garay R., Inostroza M., Ducaud A., *Color and gloss evaluation in decorative stain applied to cases of Pinus radiata wood treated with copper azole micronized Type C*, Maderas. Ciencia y tecnología, 19(1), p. 21-38, 2017.

THE ANNALS OF "DUNAREA DE JOS" UNIVERSITY OF GALATI
FASCICLE IX. METALLURGY AND MATERIALS SCIENCE
Nº. 1 - 2021, ISSN 2668-4748; e-ISSN 2668-4756
Article DOI: https://doi.org/10.35219/mms.2021.1.06

GREEN SYNTHESIS OF METALLIC NANOPARTICLES, PHYTOCHEMICAL COMPOUNDS AND ANTIOXIDANT ACTIVITY USING TWO TYPES OF ALGAE PLANTS

Ioana Raluca SUICA-BUNGHEZ[1], Ileana Cristina COVALIU[2], Ana Alexandra SORESCU[1,3], Rodica Mariana ION[1,3]

[1]The National Institute for Research & Development in Chemistry and Petrochemistry, Romania
[2]Faculty of Biotechnical Systems Engineering, University Politehnica of Bucharest, Romania
[3]University Valahia of Targoviste, Romania
e-mail: cristina_covaliu@yahoo.com, alexiasorescu@yahoo.com

ABSTRACT

Scientific studies have demonstrated that the vegetable material extracts act as potential precursors for the synthesis of nanomaterial using eco-friendly ways. Because the plant extracts contain various secondary metabolites, they act as reducing and stabilizing agents for the bioreduction reaction for synthesis of novel metallic nanoparticles.

Herein, we describe the characteristics of different algae types, from different locations (Belgium and South Correa). Algae have important components, like chlorophyll and other plant pigments, omega-3 fatty acids and essential elements. Also, it has been demonstrated that algae provide a rich source of natural bioactive compounds with antibacterial and antioxidant properties. Another important aspect is the fact that algae represent a good wastewater treatment. In addition to the economic aspect, algae biomass is a source of biodiesel and offers an efficient way for nutrient consumption and provides aerobic bacteria with oxygen through photosynthesis. It is a low-cost technique for the removal of phosphorus, nitrogen and pathogens. We first characterized and compared quantitatively (polyphenols, flavonoids) and qualitatively (carbohydrates, alkaloids) the properties of two algae types extracts (green algae - Enteromorpha spp. *and brown ones* - Hizikia fusiforme*). We then obtained and characterized the gold nanoparticles, formed using $HAuCl_4$ (10^{-3} M) and algae sample extracts. The algae extracts, the green method for obtaining metallic nanoparticles (AuNP) and the nanoparticles investigated by UV-Vis spectroscopy, optical microscopy and SEM technique are shown in this research.*

KEYWORDS: marine algae, phytochemical properties, metallic nanoparticles, green chemistry

1. Introduction

Nanotechnology is a rapidly growing area of science with tremendous impact in critical aspects of society, such as health and energy, with immediately applicability of metal nanoparticles in many areas such as medicine, catalysis, or electronics [1, 2]. This branch of science refers to the fabrication of nanoparticles with various shapes, sizes and their associated chemical and physical parameters for the beneficial use in material sciences, such as solar energy conversion, catalysis, microelectronics, photonics, antimicrobial functionalities and water management [3].

It has been previously demonstrated that plants, fruits, or vegetable materials (algae, fungi, bacteria) are excellent sources of compounds suitable for the obtaining of metallic (platinum, silver and gold) nanoparticles [4]. Some of these substances (polysaccharides, phenols, flavonoids, or tannins) can serve as reducing and also stabilizing agents. The bioorganic molecules from these extracts provide the opportunity of complex combinations of reducing and stabilizing agents, giving thereby rise to a large variety of parameters in the green preparation

THE ANNALS OF "DUNAREA DE JOS" UNIVERSITY OF GALATI
FASCICLE IX. METALLURGY AND MATERIALS SCIENCE
Nº. 1 - 2021, ISSN 2668-4748; e-ISSN 2668-4756
Article DOI: https://doi.org/10.35219/mms.2021.1.06

process, with the end result of metallic nanoparticles of different sizes and shapes [5].

Numerous attempts have been made to uncover the roles that organisms present in the accumulation of gold and its conversion to non-toxic nanoparticles [6]. Nair & Pradeep [7] have demonstrated the production of gold and silver alloy nanoparticles using lactic acid bacteria exposed to gold and silver ion mixtures. Other groups [8, 9] observed that Au (III) ions can be reduced to Au (0) by alfalfa plants or oat (*Avena sativa*) biomass forming Au nanoparticles. Similar nanogold synthesis has been reported in algae, including *Chlorella vulgaris* [10], *Sargassum wightii* [11] and *Plectonema boryanum* [12, 13]. Cyanobacteria (such as *Lyngbya majuscula* and *Spirulina subsalsa*), green algae (*Rhizoclonium hieroglyphicum* and *R. riparium*) and diatoms (*Nitzschia obtusa* and *Navicula minima*) has recently been reported to demonstrate potential of gold nanoparticle synthesis by Chakraborty et al. [14], and biosynthesis of gold nanorods by *Nostoc ellipsosporum* [15].

Over the last years, the entire process of intracellular formation of gold nanoparticles by algal biomass wasn't yet fully understood but scientists tried to demonstrate the roles that microorganisms, marine algae plants can play in the capturing of gold and its conversion to non-toxic nanoparticles, using ecofriendly methods [16].

Marine algae have received increased importance as a source for the synthesis of nanoparticles. Bioactive metabolites isolated from seaweed algae such as flavonoids, citric or ascorbic acid, polyphenolics, terpenes, alkaloids and reductase could act as reducing agents [17]. Previous studies propose that there are certain marine algae suitable not for only for gold nanoparticles synthesis, even for silver [18] or platinum [19] nanoparticles. Another studies, using *Galaxaura elongata* [20] or *Gelidiella acerosa* [21], showed for the first time the synthesis of highly stable Ag-NPs with its antimicrobial activity. Also, research studies were performed on *G. acerosa* marine algae, with demonstrated rich antioxidant characteristics, anticancer activity, cytotoxicity and antibacterial activity [22].

The use of biological processes for the treatment of wastewaters metal pollution can overcome the barriers of physical and chemical treatments and provide a way for a low-cost removal of metals. Therefore, a big interest has been generated using different types of inexpensive biomass for adsorbing or removing the heavy metals (Cr, Ni, Cu, Cd, Fe, etc) from wastewater [23]. It is very important to appreciate and appreciate the importance of seaweeds in this moment, when earth can no longer sustain the lot of wastes [24].

2. Materials and methods

We used different algae types, from Belgium and South Correa (Fig. 1 a) and b). The dried marine algae were green (*Enteromorpha spp.*) and brown (*Hizikia fusiforme*). 0.5 g from each dried algae were extracted in a hydroalcoholic mixture (EtOH: H_2O distilled), using ultrasound bath (1 hour). Then, the solutions were macerated at room temperature, in the dark, for 48 hours. The extracts were filtered through a filter paper to obtain clear samples.

a) b)

Fig. 1. *a) AB-Belgium algae (*Enteromorpha spp*) and b) AC-South Correa algae (*Hizikia fusiforme*) dried plants*

It is noteworthy to specify that the algae were chosen to obtain metallic nanoparticles, after we observed positive results for total phytochemical contents and antioxidant activity, with a high potential in balancing the oxidative stress.

For determinations of phytochemical methods, $NaNO_2$, NaOH, Na_2CO_3, DPPH and Folin–Ciocalteu reagent, from Merck and $AlCl_3$, Benedict and Millon reagents from Sigma-Aldrich were used. For gold

THE ANNALS OF "DUNAREA DE JOS" UNIVERSITY OF GALATI
FASCICLE IX. METALLURGY AND MATERIALS SCIENCE
Nº. 1 - 2021, ISSN 2668-4748; e-ISSN 2668-4756
Article DOI: https://doi.org/10.35219/mms.2021.1.06

nanoparticles, $HAuCl_4$ was purchased from Acros Organics.

Preparation of gold nanoparticles (AuNP) formed in the presence of hydro-alcoholic extracts 5 mL of fruit extract sample were added to 5 mL $HAuCl_4$ (10^{-3} M), ultrasonicated on Bioblock Scientific (30 min/40 °C) ultrasound bath, then kept in the dark overnight, at room temperature.

All experimental measurements were carried out in triplicate and are expressed as average of three analyses. Total flavonoids and polyphenols content were calculated utilizing the results of curve calibration standards (Table 1).

Table 1. *Preparation methods of phytochemicals analyses*

No.	Assay	Reagents	Conditions	Monitoring and calibration	References
1	Total Flavonoids Content	1 mL extract + 4 mL distilled water + 0.3 mL $NaNO_2$ (5%); After 5 min: 0.3 mL $AlCl_3$ (10%); After 5 min: 2 mL 1M NaOH + 2.4 mL distilled water	30 minutes kept at room temp.	Absorbance at 510 nm; Catechin curve calibration standard (R^2 = 0.9988)	25, 26
2	Total Polyphenols Content	1 mL diluted extract + 5 mL Folin-Ciocalteu reagent. After 8 min: 4 mL Na_2CO_3	60 min kept at room temp	Absorbance at 765 nm; Gallic acid curve calibration standard (R^2 = 0.9944)	27, 28

Absorption spectroscopy. The absorption spectra of the sample extracts and of the samples with silver nanoparticles were obtained using an Analytic Jena UV-VIS spectrophotometer, in the wavelength range of 250-750 nm.

Optical microscopy. The optical microscopy was performed with a Novex trinocular microscope (EUROMEX Microscopen B.V. HOLLAND) (at different magnifications: 40×, 10×, 400×, 100×).

Scanning Electron Microscopy (SEM). It was used the Scanning Electron Microscope (SEM) SU-70 (Hitachi, Japan), very sensitive equipment, with field emission which is based on a Schottky electron source. The application field of SEM (coupled with EDS, WDS and EBL) was utilized for characterization of micro- and nanoparticles from samples.

Antioxidant activity determination. The antioxidant activity of the extracts was evaluated using the DPPH method [25], via spectrophotometry. The algae samples were evaluated at 100 mg/L concentration, by mixing 0.5 mL of extract with 1 mL of DPPH solution (2 mg/100 mL). The samples were mixed 30 minutes and kept in the dark for 30 minutes, at room temperature. After that, each mixture sample was tested for the DPPH radical-scavenging activity by measuring the absorbance at 517 nm on a UV-VIS spectrophotometer. The antioxidant activity (AA %) was calculated using the formula:

$$AA\% = [(A_{Control} - A_{Extract}) / A_{Control}] \times 100$$

where: AControl is the absorbance of a DPPH solution without extract, AExtract is the absorbance of the sample extract with DPPH (2 mg/100 mL).

3. Results and discussion

Results of phytochemicals content are presented in Table 2.

The qualitative tests presented in table 3 and 4 confirmed that both algae have carbohydrates and alkaloids in their structure.

Table 2. *Results of phytochemicals content for algae plants*

Algae extract	**Antioxidant activity AA %**	**Total flavonoid content TFC mg/L**	**Total polyphenols content TPC mg/L**
AB (*Enteromorpha spp.*)	85.395	342.56	97.178
AC (*Hizikia fusiforme)*	79.728	182.23	52.262

THE ANNALS OF "DUNAREA DE JOS" UNIVERSITY OF GALATI
FASCICLE IX. METALLURGY AND MATERIALS SCIENCE
N°. 1 - 2021, ISSN 2668-4748; e-ISSN 2668-4756
Article DOI: https://doi.org/10.35219/mms.2021.1.06

Table 3. *Results of qualitative tests for carbohydrates*

Reagent/test	**Algae extract**	
	AB (*Enteromorpha spp.*)	AC (*Hizikia fusiforme)*
Molish reagent	+	+
Benedict reagent	+	+
Fehling B reagent	+	+
Ammonium molybdite test	+	+
$CoCl_2$ test	+	+
Seliwanoff reagent	+	+
Barfoed reagent	+	+

Table 4. *Results of qualitative tests for alkaloids*

Algae extract	**Mayer reagent**	**Wagner reagent**	**Hager reagent**
AB (*Enteromorpha spp.*)	+	+	+
AC (*Hizikia fusiforme)*	+	+	+

Characterization of metallic nanoparticles formed in presence of algae extract samples. The metallic nanoparticles samples were obtained by mixing of 5 mL from hydroalcoholic algae extract with 5 mL of aqueous solution of 10^{-3} M, $HAuCl_4$; then the samples were ultrasonicated and were kept overnight at room temperature. Visually, the formation of nanoparticles was evidenced by changes of color of mixed solutions (Fig. 2), due to excitation of surface plasmon vibrations in the metal nanoparticles.

a) b)

Fig. 2. *Color changed after 4 and 24 hours of A) AuNP-AB and B) AuNP-AC solutions*

UV-VIS results. The absorption bands between 280-360 nm wavelengths of algae extract samples presented specific peaks of phenolic acids and flavonoids [26], while the UV-VIS absorption spectrum of algae extract-AuNP samples (Fig. 3b) was observed between 540-580 nm areas for AuNP. The peaks appeared between 430-457 nm and 645-660 nm, in both algae extract samples are attributed to chlorophyll a and b [29].

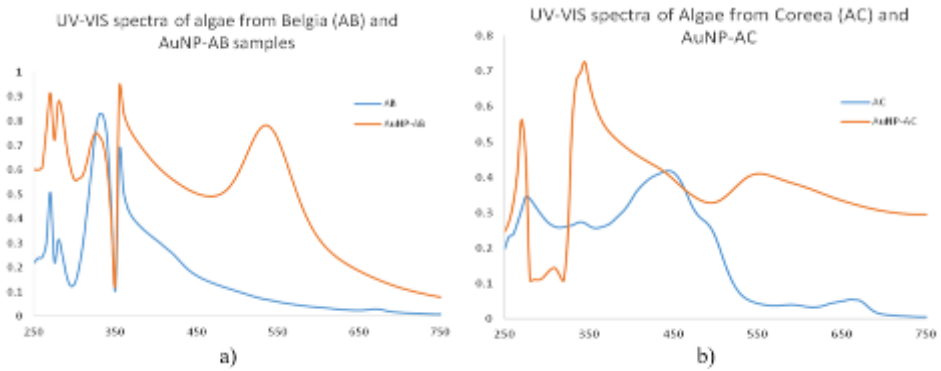

Fig. 3. *UV-Vis spectra of algae extract and gold nanoparticles (AuNP)*

THE ANNALS OF "DUNAREA DE JOS" UNIVERSITY OF GALATI
FASCICLE IX. METALLURGY AND MATERIALS SCIENCE
N°. 1 - 2021, ISSN 2668-4748; e-ISSN 2668-4756
Article DOI: https://doi.org/10.35219/mms.2021.1.06

Antioxidant activity of AuNP-algae extract samples is presented in Table 5.

Table 5. *Results of qualitative tests for alkaloids*

Sample name	AA %
AB (*Enteromorpha spp.*)	91.096
AC (*Hizikia fusiforme)*	87.154

In the next figure (Fig. 4), optical microscopy images of AC (*Enteromorpha spp.*) dried algae and the changes of algae structure after it were formed gold nanoparticles are presented.

We used scanning electron microscopy of AuNPs-*Hizikia fusiforme* extract to characterize the particle shape and morphology. The SEM results revealed that the gold nanoparticles possessed spherical shape with average particle size between 10-50 nm (Fig. 5).

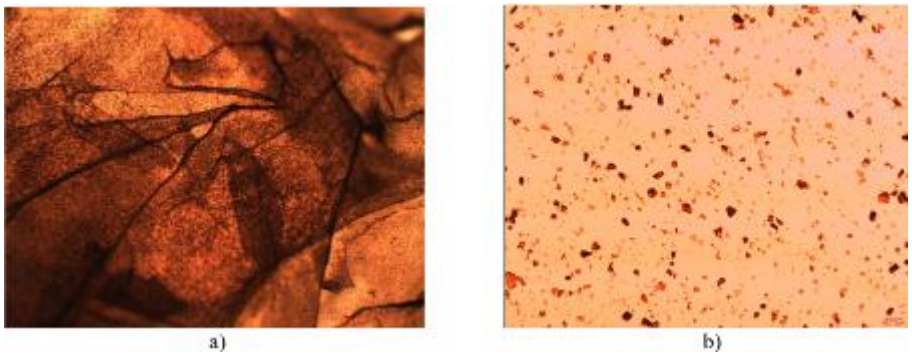

Fig. 4. *Optical microscopy of AC (*Enteromorpha spp.*) dried algae and AC-AuNP sample*

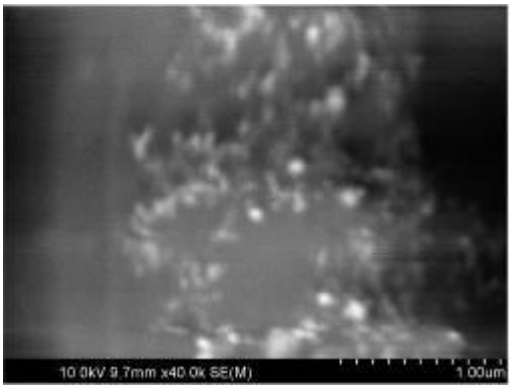

Fig. 5. *SEM of gold nanoparticles of* Hizikia fusiforme

4. Conclusions

In the present study we report a simple, economical and eco-friendly bottom-up approach to design gold nanoparticles using two different types of dried algae: green algae (*Enteromorpha spp.*) and brown ones (*Hizikia fusiforme*) and $HAuCl_4$ (10^{-3} M), which determined a shift in the color of the extracts. This was demonstrated using UV-Vis spectroscopy, which showed specific wavelengths for gold nanoparticles AuNP, between 500-550 nm. Using SEM technology, we characterized the obtained gold nanoparticles, with measurements of the average size of the synthesized nanoparticles between 10-50 nm, with spherical in morphology and capped by phytochemicals. Also, optical microscopy allowed us to see a structural parallel arrangement of dried algae structure plant. We measured the flavonoids and polyphenols contents in the obtained compounds and observed that they are higher in the green algae than the brown ones. Moreover, the high values for the measured antioxidant activity suggest a strong scavenging capacity for the gold nanoparticles samples.

Our current research concludes that the hydroalcoholic extract of algae plants possess a strong reduction efficacy of gold cations to gold nanoparticles. Due to the eco-friendly, low-cost method and the rapid capacity of algae to form nanoparticles, next step will be to make silver nanoparticles in the presence of marine algae plants and corroborated with gold nanoparticles to use them for wastewater treatment.

References

[1]. Mobasser S., Firoozi A., *Review of Nanotechnology Applications in Science and Engineering*, 6, 4, p. 84-93, 2017.
[2]. Kulkarni N., Uday Muddapur, *Biosynthesis of Metal Nanoparticles: A Review*, Journal of Nanotechnology, p. 1-8, 2014.
[3]. Thomas J. Joseph Prakash, Sowmiya K., *A review on nanotechnology and plant mediated metal nanoparticles and its applications*, 8, 6, 20 pp, 2020.
[4]. Kuppusamy P., ***et al.***, *Biosynthesis of metallic nanoparticles using plant derivatives and their new avenues in pharmacological applications – An updated report*, Saudi Pharmaceutical Journal: SPJ 24, p. 473-484, 2016.
[5]. Palanco Marta Espina *et al.*, *Templated green synthesis of plasmonic silver nanoparticles in onion epidermal cells suitable for surface-enhanced Raman and hyper-Raman scattering*, Beilstein Journal of Nanotechnology 7, p. 834-840, 2016.

[6]. Mehta S. K., Gaur J., *Use of algae for removing heavy metal ions from Wastewater: Progress and Prospects*, Critical Reviews in Biotechnology 25, p. 113-152, 2005.
[7]. Nair B., Pradeep T., *Coalescence of Nanoclusters and Formation of Submicron Crystallites Assisted by Lactobacillus Strains*, Crystal Growth & Design 2, p. 293-298, 2002.
[8]. Gardea-Torresdey J. *et al.*, *Formation and Growth of Au Nanoparticles inside Live Alfalfa Plants*, Nano Letters 2, p. 397-401, 2002.
[9]. Armendariz V. *et al.*, *The extraction of gold nanoparticles from oat and wheat biomasses using sodium citrate and cetyltrimethylammonium bromide, studied by x-ray absorption spectroscopy, high-resolution transmission electron microscopy, and UV-visible spectroscopy*, Nanotechnology 20, 10, 105607, 2009.
[10]. Ting Y. *et al.*, *Gold uptake by Chlorella vulgaris*, Journal of Applied Phycology 7, p. 97-100, 2004.
[11]. Singaravelu G. *et al.*, *A novel extracellular synthesis of monodisperse gold nanoparticles using marine alga, Sargassum wightii Greville*, Colloids and surfaces. B, Biointerfaces 57, 1, p. 97-101, 2007.
[12]. Lengke M. *et al.*, *Morphology of gold nanoparticles synthesized by filamentous cyanobacteria from gold(I)-thiosulfate and gold(III)--chloride complexes*, Langmuir: the ACS journal of surfaces and colloids 22, 6, 2780-7, 2006.
[13]. Lengke M. *et al.*, *Mechanisms of gold bioaccumulation by filamentous cyanobacteria from gold(III)-chloride complex*, Environmental science & technology 40, 20, 6304-9, 2006.
[14]. Chakraborty N. *et al.*, *Biorecovery of gold using cyanobacteria and an eukaryotic alga with special reference to nanogold formation - a novel phenomenon*, Journal of Applied, Phycology 21, p. 145-152, 2009.
[15]. Parial D. *et al.*, *Gold nanorod production by cyanobacteria – a green chemistry approach*, Journal of Applied Phycology 24, p. 55-60, 2012.
[16]. Parial D. *et al.*, *Screening of different algae for green synthesis of gold nanoparticles*, European Journal of Phycology 47, p. 22-29, 2012.
[17]. Santhoshkumar J., Rajeshkumar S., Kumar S. V., *Phyto-assisted synthesis, characterization and applications of gold nanoparticles-a review*, Biochem Biophy 11, p. 46-57, 2017.
[18]. Deepak P. *et. al.*, *Structural characterization and evaluation of mosquito-larvicidal property of silver nanoparticles synthesized from the seaweed, Turbinaria ornata (Turner) J. Agardh 1848*, Artif. Cells Nanomed Biotech 45, 5, p. 990-998, 2017.
[19]. Ramkumar V. S. *et. al.*, *Synthesis of platinum nanoparticles using seaweed Padina gymnospora and their catalytic activity as PVP/PtNPs nanocomposite towards biological applications*, Biomed Pharmacother 92, p. 479-490, 2017.
[20]. Abdel-Raouf N. *et al.*, *Green biosynthesis of gold nanoparticles using Galaxaura elongata and characterization of their antibacterial activity*, Arabian Journal of Chemistry 10, 2, S3029-S3039, 2017.
[21]. Senthil Kumar P. *et al.*, *Evaluation of alpha-amylase and alpha-glucosidase inhibitory properties of selected seaweeds from Gulf of Mannar*, Int Res J Pharma 3, p. 128-130, 2011.
[22]. Senthilkumar P. *et al.*, *Facile green synthesis of gold nanoparticles from marine algae Gelidiella acerosa and evaluation of its biological Potential*, SN Applied Sciences 1, p. 1-12, 2019.
[23]. Mehta S. K., Gaur J. P., *Use of Algae for Removing Heavy Metal Ions From Wastewater: Progress and Prospects*, Critical Reviews in Biotechnology, 25, p. 113-152, 2005.
[24]. Arumugam N. *et al.*, *Treatment of Wastewater Using Seaweed: A Review*, Int. J. Environ. Res. Public Health 15, 2851, 19 p, 2018.
[25]. Șuică-Bunghez I. R. *et al.*, *Antioxidant activity and phytochemical compounds of snake fruit (Salacca Zalacca)*, IOP Conf. Series: Materials Science and Engineering, 133, 2016.
[26]. Șuică-Bunghez, Ioana-Raluca *et al.*, *Characterization of antioxidant activity and phytochemical compounds, metal nanoparticles obtained by Sideritis Scardica extracts*", Rev. Roum. Chim., 62, 6-7, p. 545-552, 2017.
[27]. Sulaiman C. T., Balachandran I., *Total Phenolics and Total Flavonoids in Selected Indian Medicinal Plants*, Indian Journal of Pharmaceutical Sciences, 258:260, 2012.
[28]. ***, *International Standard ISO 14502-1:2005, Determination of substances characteristic of green and black tea — Part 1: Content of total polyphenols in tea — Colorimetric method using Folin-Ciocalteu reagent.*
[29]. Makarska-Bialokoz M., Kaczor A., *Computational Analysis of Chlorophyll Structure and UV-Vis Spectra: A Student Research Project on the Spectroscopy of Natural Complexes*, Spectroscopy Letters, 47, p. 147-152, 2014.

THE ANNALS OF "DUNAREA DE JOS" UNIVERSITY OF GALATI
FASCICLE IX. METALLURGY AND MATERIALS SCIENCE
N°. 1 - 2021, ISSN 2668-4748; e-ISSN 2668-4756
Article DOI: https://doi.org/10.35219/mms.2021.1.07

POLYSACCHARIDE NANOCAPSULES FOR DRUG DELIVERY APPLICATIONS, CURRENT STATUS AND FUTURE PERSPECTIVES

Marian FLOREA[1], Rodica Mariana ION[1,2]
[1] Valahia University Targoviste, 35 Lt. Stancu Ion str., 130105 Targoviste, Romania
[2] ICECHIM, 202 Splaiul Independentei, 060021 Bucharest, Romania
e-mail: florea.marian93@gmail.com

ABSTRACT

In recent years pharmaceutical formulations using polymeric nanocapsules have been widely studied for developing novel drug delivery strategies. Nanocapsules provide a unique core-shell nanostructure, consisting of a liquid/solid core surrounded by a polymeric shell. Natural or modified polysaccharides are prime candidates for use as building blocks of the nanocapsule shells, due to their demonstrated safety, versatility and low cost and to the fact that they are widely used as excipients in classical drug formulations. The aim of this paper is to present the recent advances in drug delivery strategies using polysaccharidic nanocapsules and to discuss future opportunities and challenges in developing modern pharmaceutical formulations using such systems.

KEYWORDS: drug delivery, nanotechnology, nanocapsule, polysaccharide

1. Introduction

The rapid development of nanomedicine together with recent approvals of nanoformulations [1] make developing efficient and safe nano-drug delivery systems, a central strategy in improving human health. To address the toxicological and environmental safety concerns, many research groups focus on the use of natural polymers, especially polysaccharides, for developing novel drug delivery systems (DDS) due to their safety and widespread use as pharmaceutical excipients.

Polysaccharides are one of the most abundant, renewable natural resource available. Structurally, these carbohydrates are composed of monosaccharide units, linked together by covalent glycosidic bonds. In nature, polysaccharides serve important roles in plant development, acting as structural polymers (cellulose), as energy storage (starch) and serving many other functional roles. Many of the currently used polysaccharides are also of animal origin, such as chitosan, that can be found in abundance in the shells of many invertebrates, or of bacterial origin like dextran that can be synthetized by microorganisms [2].

Polysaccharides are rich in deprotonated amino groups or carboxylic acid groups, making the polymer display a cationic or anionic charge, suitable for use in nanocapsule synthesis by electrostatic interactions [3].

In the pharmaceutical industry, polysaccharides are routinely used in pharmaceutical formulations and due to their specific qualities, they represent ideal candidates for developing drug delivery systems. The most notable advantageous characteristics of these polymers are:

- *Abundance*: in nature, polysaccharides are one of the most abundant polymers and their purification from natural sources use techniques which are well known, optimised and documented [2].
- *Versatility*: • The polymers can be functionalised through a variety of chemical and enzymatic methods to produce specialised polymers for specific uses.
• Due to the many functional groups displayed, polysaccharides can be easily functionalised with many functional molecules such as antigens [4] or can form polyelectrolytic complexes with different polymers [5].
• Ionic polysaccharides can be used for fabricating pH-dependant or Ion-dependant controlled release dosage forms [2, 6].
• The functional groups of the polysaccharides can provide bioadhesive properties to the polymer, a feature that improves the performance of drug delivery systems with mucosal administration [7].

THE ANNALS OF "DUNAREA DE JOS" UNIVERSITY OF GALATI
FASCICLE IX. METALLURGY AND MATERIALS SCIENCE
Nº. 1 - 2021, ISSN 2668-4748; e-ISSN 2668-4756
Article DOI: https://doi.org/10.35219/mms.2021.1.07

• They can be formulated into hydrogels [8, 9].

- *Safety*: polysaccharides are biocompatible, biodegradable and safe polymers with low risk of immunogenicity [2, 10].

Nanocapsules are vesicular systems consisting of an inner core surrounded by a polymeric wall that have immense potential as drug carriers because of the many advantages like improving poor aqueous solubility, stabilizing drugs by protecting the molecule from the environment, providing the desired pharmacokinetic profile, allowing controlled release, as well as facilitating oral administration [11]. Novel Drug Delivery Systems (DDS) are being developed by utilising safe and biocompatible materials like polysaccharides in nanocapsule formulations, thus improving the safety and performance of known active pharmaceutical ingredients.

The purpose of this study is to present the role of polysaccharides in the development of nanocapsule-based drug delivery systems. Since the chemical structure of polysaccharides is well known and documented, in this review I would like to bring attention to the drug delivery systems developed in the last five years, the routes of administration employed and to the methods of synthesis used for fabricating these systems.

2. Polymeric nanocapsule formulation methods

There are many papers that discuss the synthesis methods for different polymeric nanocapsules, one of the most recent being published by Deng *et al.* in 2020 [3]. Most synthesis processes use the same basic principles that were described over a decade ago, nevertheless new approaches and optimisation efforts facilitated the development of more stable, versatile, and safe systems and processes. A broad description of the classic techniques commonly used, and their use in polysaccharidic nanocapsule formation will be presented in the following chapter.

2.1. Nanoprecipitation/ interfacial deposition

The interfacial deposition method, more commonly referred to as nanoprecipitation, was first described by Fessi *et al.* in 1989 [54]. This method employs the use of two separate liquid phases comprised of a solvent and non-solvent. The solvent phase or the organic phase, contains the dissolved polymer, the active substance, an oily component and in some cases a hydrophobic surfactant. The oily component will form the core of the nanocapsules. Systems with hollow core can be formed by omitting the oil from the solvent phase [3]. The non-solvent phase is comprised of one or more non-solvents together with a hydrophilic surfactant. The most commonly used non-solvent for this reaction is water [11]. Nanocapsules are formed by the addition of the organic phase into the aqueous phase through a thin needle and continuous stirring. The polymer precipitates in contact with the non-solvent and forms a thin film on the interface between the two phases, encapsulating the organic phase and forming an aqueous suspension of nanocapsules.

It is considered that the main mechanism of capsule formations is explained by the Gibbs-Marangoni effect due to the differences in surface tension of the two phases. As such, turbionary currents are formed on the surface of the oily droplets that mix together the two phases, forcing the polymer precipitation in the non-solvent [11, 55].

For the synthesis of polysaccharidic nanocapsules, the affinity of the polymers for water must be taken into consideration. Since most modified polysaccharides are water soluble, the synthesis processes in this case will be made through W/O emulsions. The non-solvent phase will be organic, and the polymer will be dissolved into the aqueous phase. The advantage of these kind of formulations is the ability to formulate systems suitable for hydrophilic drug delivery. Steinmacher et al. describes in 2017 such a system that utilises cyclohexane as a non-solvent and water as a solvent to form modified starch nanocapsules. These capsules present a good stability without permeation issues, releasing the formulated drug only after enzymatic degradation of the polysaccharidic shell [51].

2.2. Emulsion - solvent displacement

This method was first described by Quintanar-Guerrero *et al.* in 1996 [56]. As the name suggests, this synthesis method is based on two distinct steps. In the first step an emulsion is formed in which the polymer is dissolved into the internal phase with the help of a solvent, either volatile or miscible with the external phase. After the emulsion is formed, the precipitation of the polymer is forced on the surface of the organic phase droplets, by evaporation of the solvent or by diffusion into the external phase [3, 11].

This method is similar to the nanoprecipitation technique, the difference being in the method by which the precipitation is initiated. The nanocapsule synthesis processes usually employ water as the external phase, and an oil mixed with an organic solvent such as ethanol, acetone, or ethyl acetate as internal phase. This method leads to the formation of oil core nanocapsules, which are useful in formulations containing lipophilic drug substances. Such a process was published by Sombra *et al.* in 2020 [57] for the formulation of oil core

THE ANNALS OF "DUNAREA DE JOS" UNIVERSITY OF GALATI
FASCICLE IX. METALLURGY AND MATERIALS SCIENCE
Nº. 1 - 2021, ISSN 2668-4748; e-ISSN 2668-4756
Article DOI: https://doi.org/10.35219/mms.2021.1.07

nanocapsules containing amphotericin B. The described method makes use of a mix of solvents, namely methanol and acetone, dissolved into the oil component of the system comprised of medium chain triglycerides (Miglyol 812®). This system forms spontaneous emulsions in contact with water due to the diffusion of the solvents.

During the synthesis process of nanocapsules, especially through emulsion-based techniques, the quality and quantity of employed surfactants and co-surfactants have a direct impact on system stability and capsule size.

2.3. Double emulsion

We can group the disperse systems formed by this process by the sequence in which the phases are arranged, into oil in water in oil (O/W/O) or water in oil in water (W/O/W). The critical step in the development of such systems is the careful selection of the right surfactants that can stabilise the interfacial surfaces of the emulsions, stabilising the system. The method is based on solvent diffusion or coacervation effects to form capsule walls [3]. Moise *et al.* develop a method to synthetise crosslinked gelatin and chitosan nanocapsules by a O/W/O double emulsion technique. The aqueous phase contains the dissolved polymer that will form the nanocapsule shell after reticulation due to a drop solubility [58].

2.4. Emulsion-coacervation

This method represents another emulsion-based technique where the emulsion droplets are used as templates for the formation of polymeric shell. Through the use of this technique, the polymeric capsule walls are formed by physical coacervation or chemical reticulation [3].

The coacervation method is frequently used for nanocapsule synthesis using natural polymers such as sodium alginate or gelatin [11]. Polyelectrolytic complexation represents the main mechanism of coacervation employed in the synthesis of drug delivery systems by this method. Complex coacervation can form between two polyelectrolytes or between a polyelectrolyte and a colloidal particle [59]. Dubey *et al.* develop mucoadhesive nanocapsules for the treatment of glaucoma, formed by complex coacervation of pectin and chitosan [52].

2.5. Layer by layer

The layer by layer method requires a template on which the capsule shell is formed. The general method makes use of electrostatic interactions between polyanions and polycations to form successive polymer layers onto the surface of a colloidal template.

For the manufacturing of hollow nanocapsules the process uses sacrificial templates that will be removed at the end of the synthesis process. Belbekhouche *et al.* in 2019 use gold nanoparticles as sacrificial template to form Poly-cyclodextrin and chitosan nanocapsules [45]. Ye *et al.* in 2005 [43] and later Pinheiro *et al.* in 2015 [60], synthetise nanocapsules from chitosan, alginate and fucoidan respectively using as polystyrene nanoparticles as a sacrificial template. Another approach to making hollow nanocapsules that does not utilise toxic solvents to remove the colloidal template is published in 2010 by Cuomo *et al.* that makes use of micellar structures as template that are later removed by adding a non-ionic surfactant to the suspension [44].

By combining the microemulsion method with the layer by layer technique, oil core nanocapsules can be synthetised, useful for drug delivery systems that employ hydrophobic APIs. This method uses oil droplets as templates and does not require the removal of the system core. By skipping the template removal step, there is a low risk of alternating the nanocapsule structure and the use of toxic solvents is also avoided. Szafraniec *et al.* in 2017 employs the layer by layer method to synthetise oil core nanocapsules [61].

The nanocapsule wall is formed by using cationic and anionic chitosan derivates that also act as stabilising agents during the synthesis process. The paper shows that no toxic effects are induced at 2000 mg/kg of body weight in animal toxicity studies.

By modifying the order, quality, and number of layers in the capsule shell, the nanocapsules manufactured by this method can achieve a controlled release of the formulated drug substances. This technique is especially useful for developing controlled release drug delivery systems. A pH-dependant formulation was described by Elbaz *et al.* in 2019 [62]. The described system uses chitosan, sodium alginate, poly L-arginine and Eudragit L100 as building blocks for the capsule shell. The system shows a delay in drug release in acidic condition at pH 1.2 and a sustained release at pH 7.4 when chitosan is used as the exterior layer. Another study uses κ-carrageenan and chitosan as wall components of a oily core nanocapsule. The system shows an abnormal release profile and a first order release kinetics when two layers are used, and a zero order kinetics for systems with three and four layers [50].

In recent years many research groups developed polysaccharide based nanocapsules that are shown to improve the bioavailability of conventional drugs, and even allow for new types of therapies such as needle-free vaccinations. In Table 1 are presented some of the more recent published articles on drug delivery systems based on polysaccharidic nanocapsules.

THE ANNALS OF "DUNAREA DE JOS" UNIVERSITY OF GALATI
FASCICLE IX. METALLURGY AND MATERIALS SCIENCE
N°. 1 - 2021, ISSN 2668-4748; e-ISSN 2668-4756
Article DOI: https://doi.org/10.35219/mms.2021.1.07

Table 1. *Nanocapsule-based drug delivery systems developed in the las five years*

Polymer shell	Core type	API	Function/Therapy	Formulation method	Ref.
Functionalized Chitosan	Oily - Oleic acid	-	-	Layer by Layer	[61]
Chitosan-Alginate	Hollow (Au template)	-	Antibacterial formulation	Layer by Layer	[25]
Chitosan-Pectin	API nanoparticles	Indomethacin	Controlled release DDS	Layer by Layer	[63]
Chitosan-Dextran sulfate	Oily - Vitamin E	Protein IutA	E. coli vaccine	Emulsion – Solvent diffusion Layer by Layer	[64]
Chitosan	Oily - Vitamin E	Ovalbumin	Needle-free vaccination	Emulsion – Solvent evaporation	[20]
Chitosan-Fucoidan	Hollow (PS template)	Poly-L-lysine	pH dependent release DDS	Layer by Layer	[60]
Chitosan-Pectin	API nanoparticles	Nisin	Antibacterial formulation	Emulsion-coacervation	[28]
Chitosan-Alginate	Hollow (PS template)	5-amino salicylic acid Glycomacropeptide	Controlled release DDS	Layer by Layer	[65]
Chitosan-Pluronic F127	Organic - API and acetone	Cyclosporine A	Hair growth treatment	Nanoprecipitation	[67]
Pectin-Chitosan	Hollow (Silica template)	Doxorubicin	Anticancer treatment	Layer by Layer	[68]
κ-Carrageenan-Chitosan	Oily - Olive oil	Diflunisal	Controlled release DDS	Emulsion - Layer by Layer	[50]
Furcellaran-chitosan	Organic - API	Doxorubicin	pH responsive controlled release DDS	Layer by Layer	[69]
Chitosan-Modified starch	Oily - Lemon essential oil	Essential oil	Stability enhancer of LEOs	Emulsion - Coacervation	[16]
CMS – QAS	Colloidal BSA particles	BSA	Targeted DDS (Colon)	Layer by Layer	[15]
Modified starch	Aqueous	Fluorescent dye SR 101	Enzyme triggered controlled release DDS	Interfacial deposition/polymerisation	[51]
Pregelatinized modified starch	Oily - Capric/caprylic triglycerides	Coumarin	Topical administration DDS	Emulsion – Solvent evaporation	[13]
Pregelatinized starch	Oily - Capric/caprylic triglycerides	Minocycline	Topical administration DDS	Emulsion – Solvent evaporation	[12]
Functionalized hyaluronic acid	Oily - Capric/caprylic triglycerides	Docetaxel	Anticancer treatment	Emulsion – Solvent displacement	[49]
Hyaluronic acid	Oily - Fatty alcohols and ethers, A-tocopherol	Ovalbumin, A-tocopherol	Needle-free vaccination	Emulsion – Solvent displacement	[4]
Cationic Poly(cyclodextrin) -Alginate	Hollow (Au template)	4-hidroxi tamoxifen	DDS with cyclodextrin mediated drug loading and release	Layer by Layer	[45]

THE ANNALS OF "DUNAREA DE JOS" UNIVERSITY OF GALATI
FASCICLE IX. METALLURGY AND MATERIALS SCIENCE
Nº. 1 - 2021, ISSN 2668-4748; e-ISSN 2668-4756
Article DOI: https://doi.org/10.35219/mms.2021.1.07

Modified mannan and dextran / PEI / mRNA	Hollow (Silica template)	mRNA	mRNA Vaccination	Layer by Layer	[70]
Dextran; Pullulan; Dextran sulfate; Hyaluronic acid; Glycogen	Oily - Capric/caprylic triglycerides	Camptotecin	Novel programable DDS with tuneable release kinetics	Layer by Layer / Nanoprecipitation	[71]
Sterculia Striata modified polysaccharides	Oily - Capric/caprylic triglycerides	Amphotericin B	Antifungal formulation	Emulsion – Solvent evaporation	[57], [72]
Chitosan/Pectin	Pectin gel	Brinzolamide	Glaucoma management	Ionotropic gelation/complex coacervation	[52]
Chitosan - Ca alginate	Organic - API	Liraglutide	Novel DDS diabetes management	Ionotropic gelation/complex coacervation	[73]

3. Nonparenteral routes of administration for polysaccharidic nanocapsules

Due to the bioadhesion properties of the polysaccharides and their capacity to hydrate and form hydrogels, the use of these polymers in nonparenteral drug delivery systems is verry attractive. In this segment the most recent drug delivery systems for nonparenteral administration are presented.

3.1. Topical administration

Many classical dermatological drug delivery systems are formulated so that a local effect is achieved at the site of administration onto the epidermal tissue. The main role of the skin, especially the stratum corneum, is to act as a barrier between the organism and the external medium. This raises specific challenges for topical delivery of drug substances. The efficiency of the pharmaceutical formulation is limited by the physico-chemical properties of the API, integrity and condition of the skin and lastly of the formulation efficiency and the penetration promoters utilised.

Nanocapsules represent a good response to some of the challenges that topical drug delivery raises.

They can achieve a good transcutaneous absorption of the APIs due to their small size and high specific surface area. The bioadhesion of polysaccharides is another advantage of these formulations because prolonged contact of the API with the skin promotes better absorption.

Marto *et al.* describe in 2016 oily core nanocapsules with modified starch shell. The capsules are synthetised through the emulsion-solvent evaporation method. The developed nanocapsules show a good stability and with no irritation or tolerability issues with topical administration [13]. In 2018, Marto *et al.* develop another nanocapsule formulation based on modified starch containing minocycline hydrochloride through a similar synthesis method. The process is optimised through a factorial design and the resulting capsules show an encapsulation efficiency of over 87% and with a distribution of particle size d(90) of 0.589 µm [12].

For the treatment of alopecia, in 2019 Lee et al. develop a nanocapsular system comprised of chitosan and Pluronic F127 fabricated through nanoprecipitation technique. The synthetised capsules have an encapsulation efficiency of the drug substance Cyclosporine A of up to 5% for the systems with a median size of under 100 nm. The formulation shows an improvement of cyclosporine A absorption and an increase of the number of hair follicles on the surface of the mouse skin that has been treated in vivo [67].

Recently, a great number of studies focus on the idea of nonparenteral vaccination through use of nanotechnology. Nanoparticles, due to their size, can penetrate the epidermal tissue, and their high specific surface can express a high quantity of antigen, sufficient for the generation of an immune response. Nanocapsules of approximately 100nm in size were synthetised by Bussio *et al.* using chitosan [20] or hyaluronic acid [4], Both systems show a good skin penetration and a good retention of the model proteins without affecting the cell viability in ex vivo studies.

3.2. Oral delivery

The oral route of administration represents one of the most often employed mode of drug administration. When a systemic effect is required, the oral route of administration is preferred due to its advantages over parenteral administration of drugs. Administration of oral formulations does not require

THE ANNALS OF "DUNAREA DE JOS" UNIVERSITY OF GALATI
FASCICLE IX. METALLURGY AND MATERIALS SCIENCE
Nº. 1 - 2021, ISSN 2668-4748; e-ISSN 2668-4756
Article DOI: https://doi.org/10.35219/mms.2021.1.07

specialised medical personnel or special drug administration devices. Due to these advantages the oral route has benefits from a great patient compliance and avoids certain complications that can occur when parenteral methods are used, especially in underdeveloped zones where the access to sterile medical equipment is a struggle.

The oral route of administration, despite its advantages, cannot be approached in medical emergencies or in the case of active substances with limited bioavailability. BCS class IV substances are notorious candidates for oral drug formulations due to their particularities. Some of the characteristics that make these substances hard to formulate into oral dosage forms are low solubility, low permeability through biological membranes, high interindividual variation in absorbance and sensibility to the conditions of the digestive system [74].

For the targeted administration of proteins at the colon level, Zhang *et al.* synthetise in 2017 nanocapsules through layer by layer technique using different modified starches with opposing charges. The study suggests that an optimal system for the controlled release of proteins at the colon level can be synthetised by carefully selecting the function parameters (degree of substitution and molar mass) of the employed polymers [15].

3.3. Transmucosal delivery

Polysaccharides represent ideal candidates for transmucosal formulations due to their bioadhesion that prolongs the contact time of the formulation with the administration site.

In 2020 Dubey *et al.* develop chitosan and pectin nanocapsules for ocular delivery of brinzolamide for the treatment of glaucoma. The system was synthetised through coacervation technique and the obtained nanocapsules have sizes in the range of 217.01±0.21 nm and up to 240.05±0.08 nm. In the in vitro studies, the system shows a superior release profile compared to a commercial drug product containing brinzolamide suspension. Ex vivo studies show an increased residence time at the substrate level of the nanocapsule formulation, and a better penetration at the superior cornea level, more efficiently reducing the intraocular pressure compared with the marketed drug formulation [52].

Abazoid *et al.* develops lipidic nanocapsules containing acyclovir and hydroxyethyl cellulose as a gelling agent. The optimised formulation contains 0.3% acyclovir and 3% HEC and presents a good stability at 4 °C without any crystallisation occurring. The ex vivo studies indicate an increased permeability of acyclovir nanoformulation compared to the available marketed cremes [8].

4. Conclusions

This review presents the progress in the last 5 years regarding the development and uses of polysaccharidic nanocapsules. The cited studies demonstrate an increase interest in the scientific community regarding the use of polysaccharides in nanoformulations with the goal of improving the pharmacologic profile of active substances. The synthesis methods of such systems are continuously evolving due to the recent implementation of quality by design principles. The technological progress allows a better process monitorisation and thus a more careful control of the critical process parameters. These improvements promote the development of more optimised synthesis processes that can better control the quality of the finished product. Because most of the studies are conducted at small scale or pilot scale in some cases, problems are expected when scale-up of the processes to industrial scale will be performed. As such, a good characterisation of the obtained product and a carefully controlled synthesis process represent a step in the direction of industrially manufacturing such nanoformulations.

Polysaccharides are ideal candidates for developing pharmaceutical formulations due to their low cost, biocompatibility and bioadhesive properties, but the most critical characteristic of these polymers is their safety. Several polysaccharides are commonly used as excipients in developing classical drug delivery systems. The quality of these excipients is strictly controlled by the product manufacturers, who offer a vast selection of materials with specific functional characteristics and low batch to batch variations. Most polysaccharides used in the pharmaceutical industry are classified as GRAS (Generally Regarded as Safe) by the FDA (Food and Drug Administration). The extensive use of these polymers in the pharmaceutical industry, as well as their recognised safety by the regulatory agencies represent a huge advantage for the development and approval of pharmaceutical nanoformulations.

References

[1]. Anselmo A. C., Mitragotri S., *Nanoparticles in the clinic: An update*, Bioeng. Transl. Med., vol. 4, no. 3, p. 1-16, doi: 10.1002/btm2.10143, 2019.
[2]. Posocco B. *et al.*, *Polysaccharides for the delivery of antitumor drugs*, vol. 8, no. 5. 2015.
[3]. Deng S., Gigliobianco M. R., Censi R., Di Martino P., *Polymeric nanocapsules as nanotechnological alternative for drug delivery system: Current status, challenges and opportunities*, Nanomaterials, vol. 10, no. 5, doi: 10.3390/nano10050847, 2020.
[4]. Bussio J. I., Molina-Perea C., González-Aramundiz J. V., *Hyaluronic acid nanocapsules as a platform for needle-free vaccination*, Pharmaceutics, vol. 11, no. 5, p. 1-14, doi: 10.3390/pharmaceutics11050246, 2019.

[5]. Tekie F. S. M. *et al.*, *Nano polyelectrolyte complexes of carboxymethyl dextran and chitosan to improve chitosan-mediated delivery of miR-145*, Carbohydr. Polym., vol. 159, p. 66-75, doi: 10.1016/j.carbpol.2016.11.067, 2017.
[6]. Chen C. K. *et al.*, *Synthesis of pH-responsive chitosan nanocapsules for the controlled delivery of doxorubicin*, Langmuir, vol. 30, no. 14, p. 4111-4119, doi: 10.1021/la4040485, 2014.
[7]. Berger J., Reist M., Mayer J. M., Felt O., Peppas N. A., Gurny R., *Structure and interactions in covalently and ionically crosslinked chitosan hydrogels for biomedical applications*, Eur. J. Pharm. Biopharm., vol. 57, no. 1, p. 19-34, doi: 10.1016/S0939-6411(03)00161-9, 2004.
[8]. Abozaid D., Ramadan A., Barakat H., Khalafallah N., *Acyclovir lipid nanocapsules gel for oromucosal delivery: A preclinical evidence of efficacy in the chicken pouch membrane model*, Eur. J. Pharm. Sci., vol. 121, no. 2017, p. 228-235, doi: 10.1016/j.ejps.2018.05.016, 2018.
[9]. Zhang H., Zhang F., Wu J., *Physically crosslinked hydrogels from polysaccharides prepared by freeze-thaw technique*, React. Funct. Polym., vol. 73, no. 7, p. 923-928, doi: 10.1016/j.reactfunctpolym.2012.12.014, 2013.
[10]. Shah N., Mewada R. K., Mehta T., *Nano-Polysaccharides at Drug Delivery Systems*, in International Conference on Multidisciplinary Research & Practice, vol. 1, no. 8, 2014.
[11]. Erdoğar N., Akkın S., Bilensoy E., *Nanocapsules for Drug Delivery: An Updated Review of the Last Decade*, Recent Pat. Drug Deliv. Formul., vol. 12, no. 4, p. 252-266, doi: 10.2174/1872211313666190123153711, 2019.
[12]. Marto J. M., Gouveia L. F., Gonçalves L. M. D., Ribeiro H. M., Almeida A. J., *Design of minocycline- containing starch nanocapsules for topical delivery*, J. Microencapsul., vol. 35, no. 4, p. 344-356, doi: 10.1080/02652048.2018.1487472, 2018.
[13]. Marto J. *et al.*, *A Quality by design (QbD) approach on starch-based nanocapsules: A promising platform for topical drug delivery*, Colloids Surfaces B Biointerfaces, vol. 143, p. 177-185, doi: 10.1016/j.colsurfb.2016.03.039, 2016.
[14]. Paleos C. M., Sideratou Z., Tsiourvas D., *Drug Delivery Systems Based on Hydroxyethyl Starch*, Bioconjug. Chem., vol. 28, no. 6, p. 1611-1624, doi: 10.1021/acs.bioconjchem.7b00186, 2017.
[15]. Zhang Y., Chi C., Huang X., Zou Q., Li X., Chen L., *Starch-based nanocapsules fabricated through layer-by-layer assembly for oral delivery of protein to lower gastrointestinal tract*, Carbohydr. Polym., vol. 171, p. 242-251, doi: 10.1016/j.carbpol.2017.04.090, 2017.
[16]. Hasani S., Ojagh S. M., Ghorbani M., *Nanoencapsulation of lemon essential oil in Chitosan-Hicap system. Part 1: Study on its physical and structural characteristics*, Int. J. Biol. Macromol., vol. 115, p. 143-151, doi: 10.1016/j.ijbiomac.2018.04.038, 2018.
[17]. Li J. *et al.*, *Chitosan-based nanomaterials for drug delivery*, Molecules, vol. 23, no. 10, p. 1-26, doi: 10.3390/molecules23102661, 2018.
[18]. Hussain R., Maji T. K., Maji T. K., *Determination of degree of deacetylation of chitosan and their effect on the release behavior of essential oil from chitosan and chitosan-gelatin complex microcapsules*, Rev. Téc. Ing. Univ. Zulia, vol. 37, p. 69-77, [Online]. Available: http://tjfeonline.com/admin/archive/719.09.20141411142742.pdf, 2014.
[19]. Miao T., Wang J., Zeng Y., Liu G., Chen X., *Polysaccharide-Based Controlled Release Systems for Therapeutics Delivery and Tissue Engineering: From Bench to Bedside*, Adv. Sci., vol. 5, no. 4, doi: 10.1002/advs.201700513, 2018.
[20]. Bussio J. I., Molina-Perea C., González-Aramundiz J. V., *Lower-sized chitosan nanocapsules for transcutaneous antigen delivery*, Nanomaterials, vol. 8, no. 9, p. 1-14, doi: 10.3390/nano8090659, 2018.
[21]. Bruinsmann F. A. *et al.*, *Chitosan-coated nanoparticles: Effect of chitosan molecular weight on nasal transmucosal delivery*, Pharmaceutics, vol. 11, no. 2, p. 1-19, doi: 10.3390/pharmaceutics11020086, 2019.
[22]. Mohammed M. A., Syeda J. T. M., Wasan K. M., Wasan E. K., *An overview of chitosan nanoparticles and its application in non-parenteral drug delivery*, Pharmaceutics, vol. 9, no. 4, doi: 10.3390/pharmaceutics9040053, 2017.
[23]. Jing Z. W. *et al.*, *Chitosan cross-linked with poly(ethylene glycol)dialdehyde via reductive amination as effective controlled release carriers for oral protein drug delivery*, Bioorganic Med. Chem. Lett., vol. 27, no. 4, p. 1003-1006, doi: 10.1016/j.bmcl.2016.12.072, 2017.
[24]. Ho T. H., Le T. N. T., Nguyen T. A., Dang M. C., *Poly(ethylene glycol) grafted chitosan as new copolymer material for oral delivery of insulin*, Adv. Nat. Sci. Nanosci. Nanotechnol., vol. 6, no. 3, p. 35004, doi: 10.1088/2043-6262/6/3/035004, 2015.
[25]. Belbekhouche S. *et al.*, *Chitosan based self-assembled nanocapsules as antibacterial agent*, Colloids Surfaces B Biointerfaces, vol. 181, no. January, p. 158-165, doi: 10.1016/j.colsurfb.2019.05.028, 2019.
[26]. Kulkarni A. D., Patel H. M., Surana S. J., Vanjari Y. H., Belgamwar V. S., Pardeshi C. V., *N,N,N-Trimethyl chitosan: An advanced polymer with myriad of opportunities in nanomedicine*, Carbohydr. Polym., vol. 157, p. 875-902, doi: 10.1016/j.carbpol.2016.10.041, 2017.
[27]. Khan M. M. *et al.*, *Lipid-chitosan hybrid nanoparticles for controlled delivery of cisplatin*, Drug Deliv., vol. 26, no. 1, p. 765-772, doi: 10.1080/10717544.2019.1642420, 2019.
[28]. Wang H., *Pectin-Chitosan Polyelectrolyte Complex Nanoparticles for Encapsulation and Controlled Release of Nisin*, Am. J. Polym. Sci. Technol., vol. 3, no. 5, p. 82, doi: 10.11648/j.ajpst.20170305.11, 2017.
[29]. Giri T. K., Ghosh B., Eds., *Polysaccharide-based Nano-Biocarrier in Drug Delivery. Taylor & Francis*, 2019.
[30]. Gopinath V., Saravanan S., Al-Maleki A. R., Ramesh M., Vadivelu J., *A review of natural polysaccharides for drug delivery applications: Special focus on cellulose, starch and glycogen*, Biomed. Pharmacother., vol. 107, no. April, p. 96-108, doi: 10.1016/j.biopha.2018.07.136, 2018.
[31]. Qing W., Wang Y., Wang Y., Zhao D., Liu X., Zhu J., *The modified nanocrystalline cellulose for hydrophobic drug delivery*, Appl. Surf. Sci., vol. 366, p. 404-409, doi: 10.1016/j.apsusc.2016.01.133, 2016.
[32]. Dai L., Si C. L., *Cellulose-graft-poly(methyl methacrylate) nanoparticles with high biocompatibility for hydrophobic anti-cancer drug delivery*, Mater. Lett., vol. 207, p. 213-216, doi: 10.1016/j.matlet.2017.07.090, 2017.
[33]. Liakos I. L. *et al.*, *Cellulose acetate - essential oil nanocapsules with antimicrobial activity for biomedical applications*, Colloids Surfaces B Biointerfaces, vol. 172, p. 471-479, doi: 10.1016/j.colsurfb.2018.08.069, 2018.
[34]. Rao Z. *et al.*, *Carboxymethyl cellulose modified graphene oxide as pH-sensitive drug delivery system*, Int. J. Biol. Macromol., vol. 107, no. Part A, p. 1184-1192, doi: 10.1016/j.ijbiomac.2017.09.096, 2018.
[35]. Roy J. C., Ferri A., Giraud S., Jinping G., Salaün F., *Chitosan–carboxymethylcellulose-based polyelectrolyte complexation and microcapsule shell formulation*, Int. J. Mol. Sci., vol. 19, no. 9, doi: 10.3390/ijms19092521, 2018.
[36]. Bekaroğlu M. G., İşçi Y., İşçi S., *Colloidal properties and in vitro evaluation of Hydroxy ethyl cellulose coated iron oxide particles for targeted drug delivery*, Mater. Sci. Eng. C, vol. 78, p. 847-853, doi: 10.1016/j.msec.2017.04.030, 2017.
[37]. Jacob J., Haponiuk J. T., Thomas S., Gopi S., *Biopolymer based nanomaterials in drug delivery systems: A review*, Mater. Today Chem., vol. 9, p. 43-55, doi: 10.1016/j.mtchem.2018.05.002, 2018.
[38]. Severino P., da Silva C. F., Andrade L. N., de Lima Oliveira D., Campos J., Souto E. B., *Alginate Nanoparticles for Drug Delivery and Targeting*, Curr. Pharm. Des., vol. 25, no. 11, p. 1312-1334, doi: 10.2174/1381612825666190425163424, 2019.
[39]. Aderibigbe B. A., Buyana B., *Alginate in wound dressings*, Pharmaceutics, vol. 10, no. 2, doi: 10.3390/pharmaceutics10020042, 2018.

[40]. Cheaburu-Yilmaz C. N., Lupuşoru C. E., Vasile C., *New alginate/PNIPAAm matrices for drug delivery*, Polymers (Basel)., vol. 11, no. 2, doi: 10.3390/POLYM11020366, 2019.
[41]. Wong T. W., *Alginate graft copolymers and alginate-co-excipient physical mixture in oral drug delivery*, J. Pharm. Pharmacol., vol. 63, no. 12, p. 1497-1512, doi: 10.1111/j.2042-7158.2011.01347.x, 2011.
[42]. Unagolla J. M., Jayasuriya A. C., *Drug transport mechanisms and in vitro release kinetics of vancomycin encapsulated chitosan-alginate polyelectrolyte microparticles as a controlled drug delivery system*, Eur. J. Pharm. Sci., vol. 114, p. 199-209, doi: 10.1016/j.ejps.2017.12.012, 2018.
[43]. Ye S., Wang C., Liu X., Tong Z., *Multilayer nanocapsules of polysaccharide chitosan and alginate through layer-by-layer assembly directly on PS nanoparticles for release*, J. Biomater. Sci. Polym. Ed., vol. 16, no. 7, p. 909-923, doi: 10.1163/1568562054255691, 2005.
[44]. Cuomo F., *et al.*, *Vesicle-templated layer-by-layer assembly for the production of nanocapsules*, Langmuir, vol. 26, no. 13, p. 10555-10560, doi: 10.1021/la100584b, 2010.
[45]. Belbekhouche S. *et al.*, *Cationic poly(cyclodextrin)/alginate nanocapsules: From design to application as efficient delivery vehicle of 4-hydroxy tamoxifen to podocyte in vitro*, Colloids Surfaces B Biointerfaces, vol. 179, no. January, p. 128-135, doi: 10.1016/j.colsurfb.2019.03.060, 2019.
[46]. Nurunnabi M., *et al.*, *Polysaccharide based nano/microformulation: An effective and versatile oral drug delivery system*, Elsevier Inc., 2017.
[47]. Collins M. N., Birkinshaw C., *Hyaluronic acid based scaffolds for tissue engineering - A review*, Carbohydr. Polym., vol. 92, no. 2, p. 1262-1279, doi: 10.1016/j.carbpol.2012.10.028, 2013.
[48]. Noh I., Kim N., Tran H. N., Lee J., Lee C., *3D printable hyaluronic acid-based hydrogel for its potential application as a bioink in tissue engineering*, Biomater. Res., vol. 23, no. 1, p. 1-9, doi: 10.1186/s40824-018-0152-8, 2019.
[49]. Cadete A. *et al.*, *Self-assembled hyaluronan nanocapsules for the intracellular delivery of anticancer drugs*, Sci. Rep., vol. 9, no. 1, p. 1-11, doi: 10.1038/s41598-019-47995-8, 2019.
[50]. Rochín-Wong S. *et al.*, *Drug release properties of diflunisal from layer-by- layer self-assembled k-carrageenan/chitosan nanocapsules: Effect of deposited layers*, Polymers (Basel)., vol. 10, no. 7, p. 1-16, doi: 10.3390/polym10070760, 2018.
[51]. Steinmacher F. R., Baier G., Musyanovych A., Landfester K., Araújo P. H. H., Sayer C., *Design of cross-linked starch nanocapsules for enzyme-triggered release of hydrophilic compounds*, Processes, vol. 5, no. 2, doi: 10.3390/pr5020025, 2017.
[52]. Dubey V., Mohan P., Dangi J. S., Kesavan K., *Brinzolamide loaded chitosan-pectin mucoadhesive nanocapsules for management of glaucoma: Formulation, characterization and pharmacodynamic study*, Int. J. Biol. Macromol., vol. 152, p. 1224-1232, doi: 10.1016/j.ijbiomac.2019.10.219, 2020.
[53]. Wajs E., Nielsen T. T., Larsen K. L., Fragoso A., *Preparation of stimuli-responsive nano-sized capsules based on cyclodextrin polymers with redox or light switching properties*, Nano Res., vol. 9, no. 7, p. 2070-2078, doi: 10.1007/s12274-016-1097-7, 2016.
[54]. Fessi H., Puisieux F., Devissaguet J. P., Ammoury N., Benita S., *Nanocapsule formation by interfacial polymer deposition following solvent displacement*, Int. J. Pharm., vol. 55, no. 1, p. 1-4, doi: 10.1016/0378-5173(89)90281-0, 1989.
[55]. Mora-Huertas C. E., Fessi H., Elaissari A., *Influence of process and formulation parameters on the formation of submicron particles by solvent displacement and emulsification-diffusion methods: Critical comparison*, Adv. Colloid Interface Sci., vol. 163, no. 2, p. 90-122, doi: 10.1016/j.cis.2011.02.005, 2011.
[56]. Quintanar-Guerrero D., Fessi H., Allémann E., Doelker E., *Influence of stabilizing agents and preparative variables on the formation of poly(D,L-lactic acid) nanoparticles by an emulsification-diffusion technique*," Int. J. Pharm., vol. 143, no. 2, p. 133-141, doi: 10.1016/S0378-5173(96)04697-2, 1996.
[57]. Sombra F. M. *et al.*, *Development of amphotericin B-loaded propionate Sterculia striata polysaccharide nanocarrier*, Int. J. Biol. Macromol., vol. 146, p. 1133-1141, doi: 10.1016/j.ijbiomac.2019.10.053, 2020.
[58]. Moise M. *et al.*, *Double crosslinked chitosan and gelatin submicronic capsules entrapping aminoacid derivatives with potential antitumoral activity*, J. Mater. Sci., vol. 47, no. 23, p. 8223-8233, doi: 10.1007/s10853-012-6719-1, 2012.
[59]. Liu Y., Loh X. J., *Polymer Capsules. Pan Stanford Publishing*, 2019.
[60]. Pinheiro A. C. *et al.*, *Chitosan/fucoidan multilayer nanocapsules as a vehicle for controlled release of bioactive compounds*, Carbohydr. Polym., vol. 115, p. 1-9, doi: 10.1016/j.carbpol.2014.07.016, 2015.
[61]. Szafraniec J., *et al.*, *Chitosan-based nanocapsules of core-shell architecture*, Polimery/Polymers, vol. 62, no. 7-8, p. 713-719, doi: 10.14314/polimery.2017.713, 2017.
[62]. Elbaz N. M., *et al.*, *Controlled synthesis of calcium carbonate nanoparticles and stimuli-responsive multi-layered nanocapsules for oral drug delivery*, Int. J. Pharm., vol. 574, p. 118866, doi: 10.1016/j.ijpharm.2019.118866, 2020.
[63]. Kamburova K., Mitarova K., Radeva T., *Polysaccharide-based nanocapsules for controlled release of indomethacin*, Colloids Surfaces A Physicochem. Eng. Asp., vol. 519, p. 199-204, doi: 10.1016/j.colsurfa.2016.05.040, 2017.
[64]. Crecente-Campo J. *et al.*, *Bilayer polymeric nanocapsules: A formulation approach for a thermostable and adjuvanted E. coli antigen vaccine*, J. Control. Release, vol. 286, p. 20-32, doi: 10.1016/j.jconrel.2018.07.018, 2018.
[65]. Rivera M. C., Pinheiro A. C., Bourbon A. I., Cerqueira M. A., Vicente A. A., *Hollow chitosan/alginate nanocapsules for bioactive compound delivery*, Int. J. Biol. Macromol., vol. 79, p. 95-102, doi: 10.1016/j.ijbiomac.2015.03.003, 2015.
[66]. Wang W. *et al.*, *pH-responsive Capsaicin@chitosan nanocapsules for antibiofouling in marine applications*, Polymer (Guildf)., vol. 158, no. August, p. 223-230, doi: 10.1016/j.polymer.2018.10.067, 2018.
[67]. Lee J. S. *et al.*, *A novel chitosan nanocapsule for enhanced skin penetration of cyclosporin A and effective hair growth in vivo*, Nano Res., vol. 12, no. 1, p. 29-31, doi: 10.1007/s12274-019-2546-x, 2019.
[68]. Ji F. *et al.*, *Engineering pectin-based hollow nanocapsules for delivery of anticancer drug*, Carbohydr. Polym., vol. 177, p. 86-96, doi: 10.1016/j.carbpol.2017.08.107, 2017.
[69]. Milosavljevic V. *et al.*, *Encapsulation of Doxorubicin in Furcellaran/Chitosan Nanocapsules by Layer-by-Layer Technique for Selectively Controlled Drug Delivery*, Biomacromolecules, doi: 10.1021/acs.biomac.9b01175, 2019.
[70]. Son S *et al.*, *Sugar-Nanocapsules Imprinted with Microbial Molecular Patterns for mRNA Vaccination*, Nano Lett., vol. 20, no. 3, p. 1499-1509, doi: 10.1021/acs.nanolett.9b03483, 2020.
[71]. Yan X. *et al.*, *Programmable Hierarchical Construction of Mixed/Multilayered Polysaccharide Nanocapsules through Simultaneous/Sequential Nanoprecipitation Steps*, Biomacromolecules, vol. 20, no. 10, p. 3915-3923, doi: 10.1021/acs.biomac.9b00990, 2019.
[72]. Matoso Sombra F. *et al.*, *Nanocapsules of Sterculia striata acetylated polysaccharide as a potential monomeric amphotericin B delivery matrix*, Int. J. Biol. Macromol., vol. 130, p. 655-663, doi: 10.1016/j.ijbiomac.2019.02.076, 2019.
[73]. Shamekhi F., *et al.*, *Development of chitosan coated calcium-alginate nanocapsules for oral delivery of liraglutide to diabetic patients*, Int. J. Biol. Macromol., vol. 120, p. 460-467, doi: 10.1016/j.ijbiomac.2018.08.078, 2018.
[74]. Ghadi R., Dand N., *BCS class IV drugs: Highly notorious candidates for formulation development*, J. Control. Release, vol. 248, p. 71-95, doi: 10.1016/j.jconrel.2017.01.014, 2017.

THE ANNALS OF "DUNAREA DE JOS" UNIVERSITY OF GALATI
FASCICLE IX. METALLURGY AND MATERIALS SCIENCE
Nº. 1 - 2021, ISSN 2668-4748; e-ISSN 2668-4756
Article DOI: https://doi.org/10.35219/mms.2021.1.08

MANUFACTURING TECHNOLOGY OF SOME IMPACT RESISTANT MATERIALS

Iulian PĂDURARU, Vasile BRIA, Adrian CÎRCIUMARU
"Dunarea de Jos" University of Galati, Romania
e-mail: iulian.paduraru@ugal.ro

ABSTRACT

In this paper impact resistance is a key parameter for composite materials. Composite structures can experience impact loads either accidentally in the designed life or in an anticipated hostile service environment. That is why the manufacturing technology is very important. For materials manufacture were established: the type of polymer matrix, the types of fabrics and additives which will be used to improve impact resistance and also analysis of mechanical properties of formed composite materials (bending and tensile tests). Knowledge of the mechanical properties of polymeric materials is necessary in all areas of their applicability. Thus, rigidity and mechanical strength are key properties for most applications in which polymeric matrix composites are used.

KEYWORDS: impact resistance, epiphen, composite materials

1. Introduction

A composite material consists of two elements: the support matrix for the second component, the reinforcement and/or the additive chosen depending on the field of use of the composite material formed and the properties it is intended to have [1]. The properties of the composite depend on the properties of the constituents, the ratios of their presence in the final material, the shapes and dimensions of the dispersed phase or phases [2]. Engineers are often required to provide impact energy data for various components. Impact resistance is the ability of a material to withstand a sudden applied load and is expressed in terms of energy. The impact involves the collision of two bodies: the impactor and the target. In a collision, the contact force develops as the impactor pushes the target [3]. Knowledge of the dynamic response of the structure and its resistance to damage is very necessary to optimize the structure that requires high safety, such as structural applications of aircraft. Under laboratory-controlled conditions, impact testing can be used to validate prototype models or to ensure that they meet the durability and safety requirements of the products.

In the last 15 years, a large number of new high-performance polymer fibres have been developed, including aramid fibers (Kevlar®, Twaron®), polyethylene fibers (Dyneema®, Specter®) and polypropylene fibers (Curv®, Tegris ®) [4].

Many analytical models that predict the impact resistance of composite materials are available. Among the authors who have contributed in this field we list Shivakumar [5], Christoforou [6, 7], Olsson [8] and, more recently, Talagani [9]. The methods they use include energy balance models to predict maximum force [10], simple models that determine the response over time, and more complex models that involve series extensions.

Low energy impact tests can be defined as events that can occur in the range of 1-50 m/s depending on the rigidity of the target, the properties of the materials, the mass and the rigidity of the projectile. A low-speed impact can occur during operation or during maintenance and can be considered one of the most dangerous [11].

Currently, no acceptable standard test procedures are available for testing the impact of composites. As a result, a wide variety of test procedures, test tube geometries and data analysis techniques are currently used. Gas guns offer representative approaches for assessing the impact response of composite materials. That is why the analysis of mechanical properties of formed composite materials (bending and tensile tests) provides precursor data for impact tests.

For the formation of materials were established: the type of polymer matrix, the types of fabrics and additives, which will be used in order to improve impact resistance, analysis of mechanical properties of composite materials (bending and tensile tests).

THE ANNALS OF "DUNAREA DE JOS" UNIVERSITY OF GALATI
FASCICLE IX. METALLURGY AND MATERIALS SCIENCE
Nº. 1 - 2021, ISSN 2668-4748; e-ISSN 2668-4756
Article DOI: https://doi.org/10.35219/mms.2021.1.08

2. Materials and methods

The following fabrics were chosen for the formation of materials: glass fabric with a density of 280 g/m^2, carbon fabric with a specific density of 240 g/m^2, low-density carbon-Kevlar fabric and high-density carbon-Kevlar fabric.

Table 1. *Characteristics of carbon fabric with specific density 240 g/m^2*

Characteristics	Nominal	Tolerance	Normative
Mass per unit area [g/m^2]	240	± 5%	ISO 4605
Fabric	simple		ISO 2113
Thickness [mm]	0.20	± 2.5%	ISO 5084

Fig. 1. *Carbon fabric with a specific density of 240 g/m^2*

Table 2. *Properties of carbon fabric with specific density 240 g/m^2*

Nominal construction	Warp	Weft
Description of fibers	HR Carbon Fiber 3K - 200 tex	HR Carbon Fiber 3K - 200 tex
Number of threads	6.0 knots/cm - ISO 4602	6.0 knots/cm - ISO 4602
Weight distribution	120 g/m²	120 g/m²
Weight rate	50%	50%

Glass fabric has mechanical properties approximately comparable to that of carbon. Although not as strong or rigid as carbon fibre, it is much cheaper and significantly less brittle when used in composites. Therefore, glass fibre is used as a curing material for many polymeric products. A solvent was used to treat the glass fabric, which was sprayed onto the fabric and can be seen in the figure below. The drying of the fabric was done in a well-ventilated space.

After treating the fabrics, the architectures of the composite materials were established. Sheets were cut from fabrics with dimensions 210 x 297 mm and the orientation of the fibres at 0°, -30°, 30°, 45°, 60° and 90° depending on the configuration of the layers.

The components of the epoxy system used in this study are: EPYPHEN RE resin with EPIPHEN DE 4020 hardener with short curing time. Clays have high elasticity, high compressibility, high swelling capacity, in-permeability and dimensional stability.

THE ANNALS OF "DUNAREA DE JOS" UNIVERSITY OF GALATI
FASCICLE IX. METALLURGY AND MATERIALS SCIENCE
Nº. 1 - 2021, ISSN 2668-4748; e-ISSN 2668-4756
Article DOI: https://doi.org/10.35219/mms.2021.1.08

Fig. 2. *Sprayer device used to treat glass fibre*

Fig. 3. *Cutting high-density carbon-Kevlar fabric at different sizes*

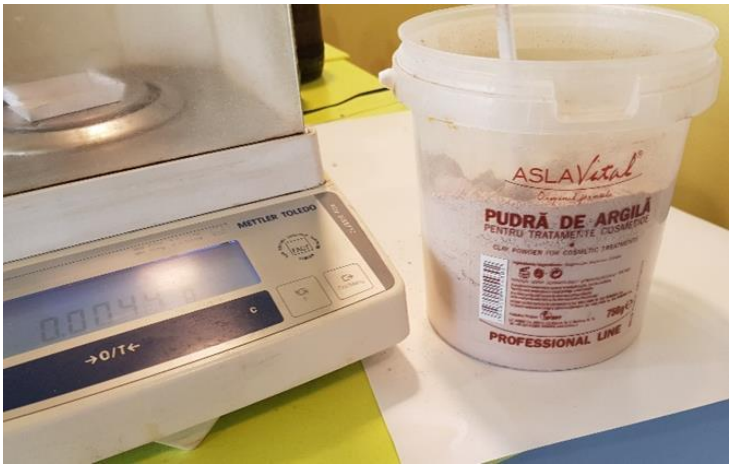

Fig. 4. *Clay powder used in the manufacture of composite materials*

THE ANNALS OF "DUNAREA DE JOS" UNIVERSITY OF GALATI
FASCICLE IX. METALLURGY AND MATERIALS SCIENCE
N°. 1 - 2021, ISSN 2668-4748; e-ISSN 2668-4756
Article DOI: https://doi.org/10.35219/mms.2021.1.08

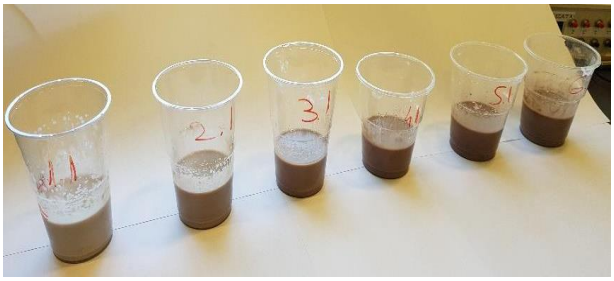

Fig. 5. *Volume percentages of clay in epoxy resin*

Table 3. *Calculation of the quantities of materials used in the formation of composite materials*

	Mixture [g]	**EPIPHEN RE 4020 [g]**	**EPIPHEN DE 4020 [g]**	**Clay [g]**	**Total [g]**
A17+1%	40	40	12	0.92	92
A9+2%	28.42	47.36	14.2	1.83	90
A1+3%	12	60	18	2.78	90
A1+4%	12	60	18	3.75	90
A1+5%	12	60	18	4.73	90
A1+6%	12	60	18	5.74	90

Two glass plates measuring 210 x 297 mm were used to form the materials. For more efficient removal of polymer composites from the mould, polypropylene foils were used between the glass plates and the material (epoxy resin does not adhere to their surface). They were arranged in the matrix layer by layer by soaking and embedding them directly in the matrix. After the introduction of all layers, the mould was closed and placed in a horizontal position to ensure the quality of the structure and surfaces of the formed materials.

3. Results

Composite materials consist of 30 layers of fabric as follows:

- the first 10 layers of low-density carbon-Kevlar fabric;
- the next 5 layers of high-density carbon-Kevlar fabric;
- the next 10 layers of glass cloth with a density of 280 g/m^2;
- the following 5 layers of carbon fabric with a specific density of 240 g/m^2.

Table 4. *Orientation of the layers in the composite material*

No. layer	**Orientation**	**No. layer**	**Orientation**
1	0°	16	0°
2	30°	17	-60°
3	45°	18	45°
4	-30°	19	30°
5	0°	20	90°
6	0°	21	-90°
7	30°	22	30°
8	45°	23	45°
9	-30°	24	60°
10	0°	25	0°
11	0°	26	0°
12	30°	27	30°
13	45°	28	45°
14	-30°	29	-30°
15	0°	30	0°

THE ANNALS OF "DUNAREA DE JOS" UNIVERSITY OF GALATI
FASCICLE IX. METALLURGY AND MATERIALS SCIENCE
Nº. 1 - 2021, ISSN 2668-4748; e-ISSN 2668-4756
Article DOI: https://doi.org/10.35219/mms.2021.1.08

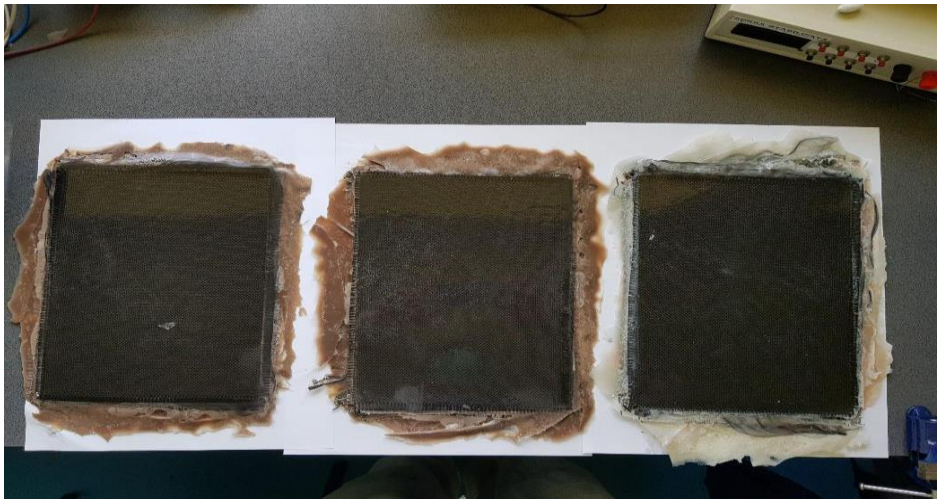

Fig. 6. *Formed composite materials*

4. Conclusions

Preparation methods of a polymeric composite material involves several steps: the amount of material required. This was determined by calculating the volume of mixture required. So, the polymeric matrix is established. This implies the polymerization time, the formation temperature and the properties of the formed materials. Another step is the choice or fixation of the modifier (modifying agent), which provides its choice to improve the properties of the material depending on its size and behaviour. The behavior of materials during mechanical stresses (produced by external forces) depends on the specific characteristics of the material from which the parts are formed.

References

[1]. Alămoreanu E., Mihai Constantinescu D., *Proiectarea plăcilor compozite laminate*, Editura Academiei Române, București, 2005.

[2]. Callister W. D., *Materials Science and Engineering*, John Wiley & Sons, 1994.

[3]. Gin B. C., Periyasamy M., *Low velocity impact response of fibre-metal laminates – A review*, Composite Structures 107, p. 363-381, 2014.

[4]. Iannucci L., Pope D., *High velocity impact and armour design*, XPRESS Polymer Letters, vol. 5, no. 3, p. 262-272, 2011.

[5]. Shivakumar K. N., Elber W., Illg W., *Prediction of impact force and duration due to low-velocity impact on circular composite laminates*, Journal of Applied Mechanics, 52(3), p. 674-680, September 1985.

[6]. Christoforou A. P., Swanson S. R., *Analysis of impact response in composite plates*, International Journal of Solids and Structures, 27(2), p. 161-170, 1991.

[7]. Christoforou A. P., Yigit A. S., *Characterization of impact in composite plates*, Composite Structures, 43, p. 14-24, 1998.

[8]. Olsson R., *Mass criterion for wave controlled impact response of composite plates*, Composites Part A: Applied Science and Manufacturing, 31(8), p. 879-887, August 2000.

[9]. Talagani M. R., *Impact analysis of composite structures. PhD thesis*, Delft University of Technology, December 2014.

[10]. Esrail F., Kassapoglou C., *An efficient approach for damage quantification in quasiisotropic composite laminates under low speed impact*, Composites Part B: Engineering, 61, p. 116-126, May 2014.

[11]. Shivakumar K. N., Elber W., Illg W., *Prediction of low velocity impact damage in thin circular laminates*, American Institute of Aeronautics and Astronautics Journal, p. 442-449. 1985.

THE ANNALS OF "DUNAREA DE JOS" UNIVERSITY OF GALATI
FASCICLE IX. METALLURGY AND MATERIALS SCIENCE
Nº. 1 - 2021, ISSN 2668-4748; e-ISSN 2668-4756
Article DOI: https://doi.org/10.35219/mms.2021.1.09

SPECTRAL CHARACTERIZATION OF MACRO-HETEROCYCLIC COMPOUND RhTMPyP / ZnTSPc

Liviu OLTEANU[1,4], Rodica Mariana ION[1,2,3], Sofia TEODORESCU[4], Raluca Maria ŞTIRBESCU[4]

[1] Valahia University of Targoviste, Doctoral School of Materials Engineering, 130105, Targoviste, Romania
[2] Valahia University of Targoviste, Materials Engineering and Mechanics Department, 130004, Targoviste, Romania
[3] National Institute for Research and Development in Chemistry and Petrochemistry - ICECHIM, "Conservation and Evaluation of Cultural Haritage" Research Group, 060021, Bucharest, Romania
[4] Valahia University of Targoviste, Institute of Multidisciplinary Research for Science and Technology, 130004, Targoviste, Romania
e-mail: olteanu.liviu@icstm.ro

ABSTRACT

Macro-heterocyclic compounds, such as porphyrins and phthalocyanines, are being studied extensively for their important physical and chemical properties. Their ability to absorb light throughout the spectrum and self-organization being adequate for the realization of several applications. Investigations of the spectral properties of the supramolecular assembly RhTMPyP/ ZnTSPc- 5,10,15,20 rhodium tetramethyl-pyridyl porphyrin / 2,9,16,23 zinc tetrasulfonated-phthalocyanine are registered by UV-Vis, FT-IR and Raman spectroscopic techniques.

KEYWORDS: porphyrins, phtalocyanines, macro-heterocyclic compound, UV-Vis, FT-IR, Raman

1. Introduction

Tetrapyrrole macrocycle based π-conjugated systems, such as porphyrin and phthalocyanine derivatives, are very famous rigid and aromatic molecular building blocks with special electronic structures [1]. Both porphyrin and phthalocyanine derivatives have distinctive photophysical, photochemical and electrochemical properties and the application of these systems have been developed in the field of photochemistry and electrochemistry [2].

As very chemically versatile compounds, both of these chemical compounds could insert different central metals, a wide range of photophysical, photochemical properties and also interesting applications could be obtained [3]. By coupling porphyrins with phthalocyanines, heterocomplexes useful for photodynamic applications could be obtained. Their association is based on „electrostatic"mixed dimers by pairing porphyrin and phtalocyanine bearing substituents with opposite charges, and have higher efficiency and stability [4].

Porphyrins are a class of macro-heterocyclic organic compounds, composed of four modified pyrrole subunits interconnected at their α carbon atoms via methine bridges [5]. In metallo-porphyrins, different metals (with bi-, tri- or tetra-valence) could be inserted into the macrocycle and for their spatial stability, halogen atoms could be attached as axially ligand, as is the case of Rh(III)TMPyP (Figure 1), where a single chlorine atom is necessary for this metallo-porphyrin stability [6].

Because Rh has a large atomic radius (1.4 Å), it cannot be included in the plane structure of porphyrin, where the macrocycle has the size of the cavity 1.3 Å and, in this sense, it can adopt a position above the porphyrin plane, with chlorine as axial ligand.

Phthalocyanines are azaporphyrins consisting of four benzoindole nuclei connected by nitrogen bridges in a 16-membered ring of alternating carbon and nitrogen atoms around a central metal atom which form stable chelates with metal cations (die or paramagnetic ion).

The molecule consists of the central metal atom, which is surrounded by four nitrogen atoms-pyrrole; four other nitrogen atoms-bridging aza; 32 carbon atoms-the pyrrole and the benzene ones (Figure 2) [7, 8].

THE ANNALS OF "DUNAREA DE JOS" UNIVERSITY OF GALATI
FASCICLE IX. METALLURGY AND MATERIALS SCIENCE
Nº. 1 - 2021, ISSN 2668-4748; e-ISSN 2668-4756
Article DOI: https://doi.org/10.35219/mms.2021.1.09

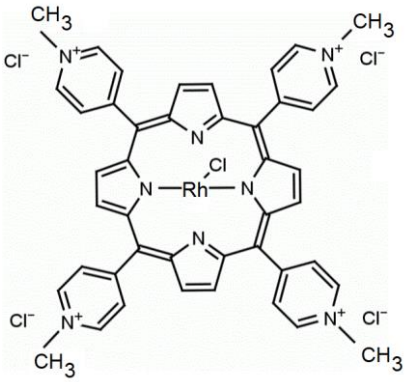

Fig. 1. *Chemical structure of RhTMPyP*

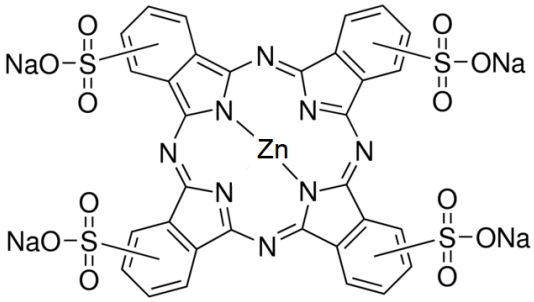

Fig. 2. *Chemical structures of ZnTSPc*

One of the most important properties of the porphyrin and phthalocyanine molecules is their ability to coordinate to metal ions, yielding to stable systems.

Stable complexes of metallo-porphyrins and metallo-phthalocyanines results from formation of four equivalent σ bonds N→M. Both of them contain a 18π electron system that contributes to their remarkable thermal and chemical stability [9, 10].

In this work, the spectral properties of the macro-heterocyclic compound: rhodium-tetramethyl-pyridyl porphyrin (RhTMPyP) with zinc-tetra-sulphonated phthalocyanine (ZnTSPc) has been studied through UV-Vis, FT-IR and Raman analysis.

2. Materials and Methods

2.1. Materials

Rh (III)TMPyP and ZnTSPc have been used as pure materials, without any supplementary procedures from Aldrich company, while their heteroaggregate has been prepared in the laboratory after the following method: Rh (III)TMPyP has been converted into their chloride salts by passing them through the VIONIT AS-14 ion-exchange column in the chloride form. Then, the phthalocyanine was transformed into its sodium salt. A 0.088 g sample of ZnTSPc was dissolved on a stoichiometric amount (1:4) of NaOH (3.9 mL, 0.1 M). The solution was filtrated, and the filtrate was dried under a stream of air overnight. A 0.05 g amount of this product was dissolved in 30 mL of water.

In another beaker, an equimolar mass of Rh (III)TMPyP (0.05 g) was dissolved in the same amount of water and the two solutions were mixed.

The final solutions were left for three weeks to ensure complete precipitation and then filtered by gravity [11].

2.2. Methods

The UV–VIS spectra were recorded with a SPECORD M 400 Carl Zeiss Jean spectrophotometer with microprocessor and double beam.

Infrared spectra were measured using an FT-IR spectrometer (VERTEX 80), in the following conditions: range 4000 cm^{-1} to 580 cm^{-1}, 32 scan, resolution 4 cm^{-1}. FT-IR spectra were achieved using Attenuated Total Reflectance (ATR) accessory with diamond crystal. ATR spectroscopy usually requires little to no sample preparation.

Raman spectra were recorded with a portable Xantus-2 TM Raman analyzer (Rigaku, Boston, United States of America) equipped with two laser sources (i.e., 785 nm and 1064 nm) and two detectors (i.e., TE cooled CCD and TE cooled InGaAs).

3. Results and discussions

Porphyrins and phthalocyanines, are compounds with great potential for serving as components of molecular materials that possess unique electronic, magnetic and photophysical properties, due to a large number of these chromophores, and for this reason it is of importance to construct arrays in which the molecules are organized in well-defined geometries with respect to their neighbours.

The phthalocyanine exhibit UV–Vis absorption spectra with an intense π-π transitions, usually referred to as Q-bands, in the range 660–799 nm with associated higher energy vibrational components in the range 600-660 nm [12].

Also, the phthalocyanines have a B Soret band in the range 420-320 nm, an N-band around 330-285 nm and an L-band at 270-230 nm. The UV-Vis spectra of the phthalocyanines are highly solvent and concentration-dependent. At high concentration in liquid protic solvent in water, for example, phthalocyanines could form aggregates [11].

During this study the spectra of phthalocyanine and porphyrin were carried out in DMSO solutions because DMSO prevents aggregation of each entity.

THE ANNALS OF "DUNAREA DE JOS" UNIVERSITY OF GALATI
FASCICLE IX. METALLURGY AND MATERIALS SCIENCE
Nº. 1 - 2021, ISSN 2668-4748; e-ISSN 2668-4756
Article DOI: https://doi.org/10.35219/mms.2021.1.09

In general, the UV–VIS spectra of phthalocyanine free base shows a Q absorption band at 718 nm with a shoulder at 689 nm. As metallic complex with Zn, and with sulphonated substituents, the phthalocyanine shows blue shifts [13].

In the porphyrin free base spectra, could be registered a Soret band (around 414 nm) and four Q bands from 500 to 700 nm.

By metallation, the Soret band support a red shift, while the Q bands are reduced to only two bands (around 560 and 650 nm).

The existence of heterodimers and heterotrimers between the porphyrin and the phthalocyanine has been demonstrated by titration using spectrophotometric methods, such as absorption spectroscopy.

The heteroaggregate between Rh(III)TMPyP and ZnTSPc can adopt a close-contact, face-to-face mutual configuration, in order to optimize the π-π interactions between aromatic cores. The spectral evolution of a solution of Rh(III)TMPyP in DMSO upon addition of ZnTSPc is shown in Figure 3.

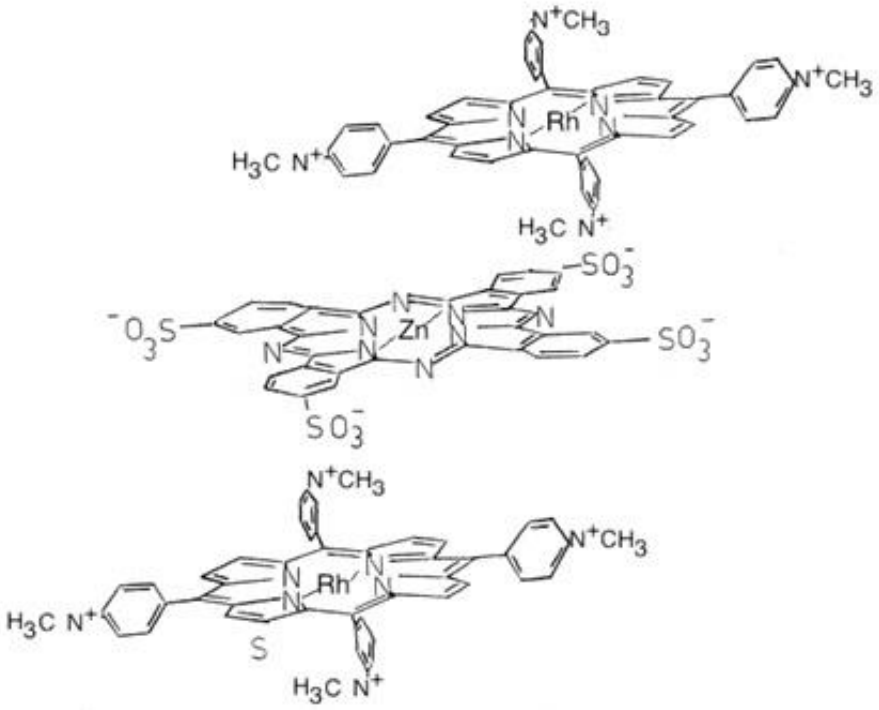

Fig. 3. *The structure of the heteroaggregate Rh(III)TMPyP/ZnTSPc*

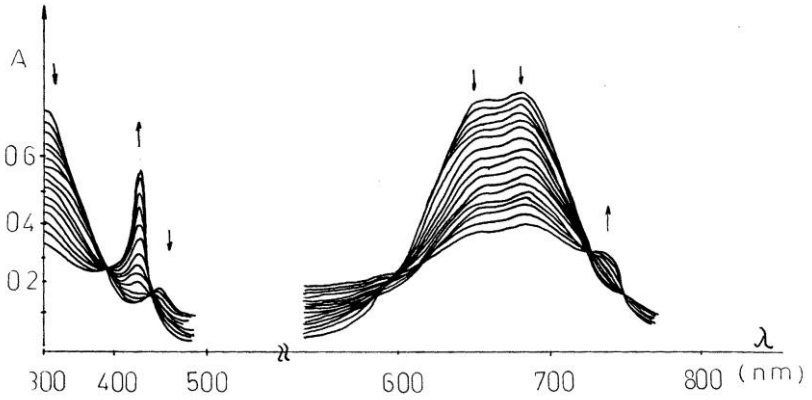

Fig. 4. *The spectral changes of UV-Vis for Rh(III)TMPyP/ZnTSPc*

THE ANNALS OF "DUNAREA DE JOS" UNIVERSITY OF GALATI
FASCICLE IX. METALLURGY AND MATERIALS SCIENCE
N°. 1 - 2021, ISSN 2668-4748; e-ISSN 2668-4756
Article DOI: https://doi.org/10.35219/mms.2021.1.09

During the titration, the Q-band of the phthalocyanine from 717 nm will become less intense and broader until its disappearance. A heteroaggregate with shorter distances between the components exhibits a larger shift of the porphyrinic Q 0,0 -band.

The heteroaggregation will occur only between N+ substituents from the porphyrine and the sulfonated phtalocyanine from the meso-positions (Figure 4).

Infrared (IR) spectroscopy is the most suitable method for identifying the presence of polar functional groups in the molecule structure of organic compounds.

To determine the structure of organic compounds, only the middle IR domain is used, and the characterization is achieved by using wavenumbers in the range 400-4000 cm^{-1}.

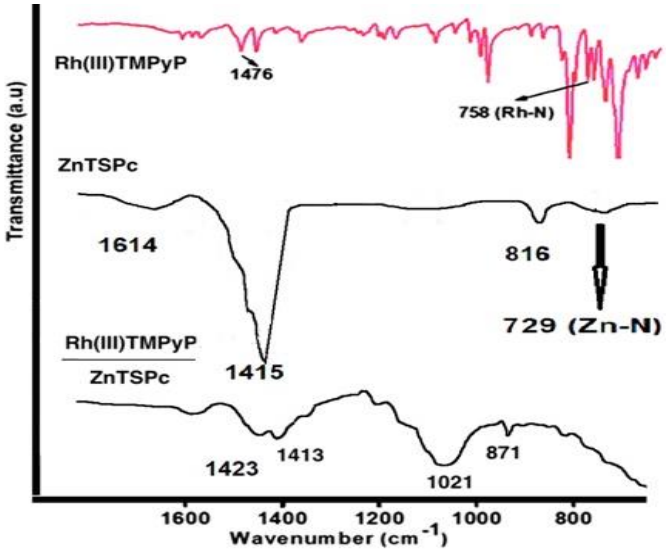

Fig. 5. *IR spectra of RhTMPyP / ZnTSPc and individual components*

The IR spectra of aromatic condensed benzene rings of metal phthalocyanines and porphyrins include the most extensive set of stretching and bending vibration bands: stretching vibrations of C-H bonds (3046-3060 cm^{-1}).

Relatively low intensity and skeletal C-C vibrations (1580-1610 cm^{-1}) with intensities are varying from moderate to very low. The frequency of 1580 cm^{-1} is caused by stretching vibrations of the C-C bond condensed with the pyrrole cycle.

Intense vibrations in the region of 947 cm^{-1} are totally symmetric stretching vibrations of C-C bonds of the aromatic ring. Plane bending vibrations of C-H are in the ranges of 1283–1289, 1158–1167, 1091–1096, and 1033–1060 cm^{-1}. Out-of-plane bending vibrations of C–metal bonds of metal phthalocyanines and porphyrins appear in the range of 720–780 cm^{-1}.

The complexity of the metallo-porphyrin molecule and the strong interaction of the ligand and metal ion could be responsible for the coupling of the ligand and metal-ligand vibrations [14, 15]. The high stability of the metallo-porphyrins suggests a somewhat higher frequency for the metal-nitrogen stretching mode. The far-infrared spectra of the metallo-porphyrins show a series of metal-dependent ligand absorption bands. The broad, medium intensity porphyrin deformation band at 500 cm^{-1} is shifted to a higher frequency in the metallo-porphyrins.

The most intense band in the far-infrared spectra of the metalloporphyrins appears at 350 cm^{-1}, and the adjacent weaker band at 380 cm^{-1}, can be attributed to the metal-free ligands and metal-nitrogen bond.

Vibrations of the –C=C–N= group (pyrrole fragment and nitrogen meso-atoms) appear as a low intensity band at 1396–1407 cm^{-1} and a very strong (characteristic of all phthalocyanines) band at 1320–1365 cm^{-1} [16].

At porphyrins, a high-intensity band at 1500–1530 cm^{-1} corresponds to vibrations of nitrogen bridging atoms (meso-atoms –N=). Stretching vibrations including vibrations of the pyrrole and benzene residues are in the range of 1420–1480 cm^{-1}; the band intensity varies from low to very high. The bands at 1594-1608 cm^{-1} and 1573-1582 cm^{-1} can be assign to C-N stretching vibrations, see Figure 5.

Different from the IR spectroscopic method which only depends on the chemical composition and phase of the samples, the resonance Raman spectral features also depend on the excitation wavelengths.

THE ANNALS OF "DUNAREA DE JOS" UNIVERSITY OF GALATI
FASCICLE IX. METALLURGY AND MATERIALS SCIENCE
Nº. 1 - 2021, ISSN 2668-4748; e-ISSN 2668-4756
Article DOI: https://doi.org/10.35219/mms.2021.1.09

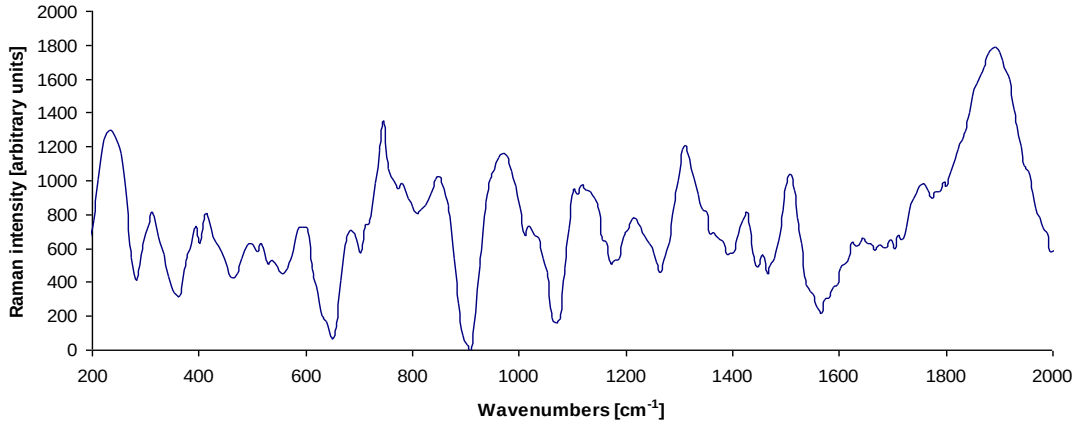

Fig. 6. *Raman spectra of RhTMPyP / ZnTSPc*

The obtained Raman spectrum shows prominent peaks whose Raman displacements are characteristic of the vibrational frequencies of the atoms in the molecules in which they are found, see Figure 6. The Raman spectra of analysed macro-heterocyclic compound shows some specific bands for these compounds at 1527 and 1538 cm^{-1}. They have been collected using laser excitation sources emitting at 632.8 and 785 nm. Under excitation at 632.8 nm, the most intense Raman band appears at 1598 cm^{-1} which is assigned to the isoindole stretching.

Typical Raman marker bands of the monoanion radical Pc.- were observed at 1499–1512 cm^{-1} as a medium band and at 1521−1538 cm^{-1} as a band whose intensity increases with the aggregation, resulting from the coupling of N^+ with SO_3^{-2} respectively.

In the context of surface chemistry, porphyrins, phthalocyanines and their metal complexes stand out from other organic molecules because of their, in relation to size and complexity, remarkable stability, their specific ligand-functionality and reactivity towards metals, as well as the planar structures of their parent macrocyles [17].

4. Conclusions

To develop new sensitizers based on macro-heterocyclic compounds, in this paper were studied the RhTMPyP/ ZnTSPc compound. Spectral properties of the studied materials indicated that these could be perspective for many applications, due to their versatility to change their central metal valence and to attach new substituents.

Under this context, RhTMPyP/ ZnTSPc is a special compound with proper properties. Their capacity of association has been identified by UV-Vis, FT-IR and Raman spectral techniques, which identified their internal bonds, their capacity to add new axial ligand and to create larger and versatile spatial structures.

Acknowledgements

The research leading to these results has received funding by Executive Agency for Higher Education, Research, Development and Innovation Funding (UEFISCDI) under the project PN-III-P1-1.2-PCCDI2017-0476 "New diagnosis and treatment technologies for the preservation and revitalization of archaeological components of the national cultural heritage", ctr. no 51PCCDI/2018.

References

[1]. Buchler J. W., Ng D. K. P., *Metal Tetrapyrrole Double- and Triple-Deckers with Special Emphasis on Porphyrin Systems*, New York, NY: Academic Press, 2000.

[2]. Bian Y., Zhang Y., Ou Z., Jiang J., *Chemistry of sandwich tetrapyrrole rare earth complexes*, in Handbook of Porphyrin Science, Singapore: World Scientific Publishing Co. Pte. Ltd., p. 249-460, 2011.

[3]. Ion R.-M., Yilmaz I., Bekaroglu O., *Supramolecular assemblies of pyridyl porphyrin and diazadithia phthalocyanine*, Journal of the Serbian Chemical Society, 64(7-8), p. 453-458, 1999.

[4]. Agirtas S., Ion R.-M., Bekaroglu O., *Spectral study of the supramolecular assemblies porphyrins-phthalocyanines*, Materials Science and Engineering: C, 7(2), p. 105-110, 1999.

[5]. Cook L. P., Brewer G., Wong-Ng W., *Structural aspects of porphyrins for functional materials applications*, Crystals, 7(7), p. 223-244, 2017.

[6]. Thompson S. J., Brennan M. R., Lee S. Y., Dong G., *Synthesis and applications of rhodium porphyrin complexes*, Chemical Society Reviews, 47(3), p. 929-981, 2018.

[7]. Suslick K. S., Rakow N. A., Kosal M. E., Chou J. H., *The materials chemistry of porphyrins and metalloporphyrins*, Journal of Porphyrins and Phthalocyanines, 4, p. 407-413, 2000.

[8]. de Toledo M., *et al.*, *Zinc phthalocyanine tetrasulfonate-loaded polyelectrolytic PLGA nanoparticles for photodynamic therapy applications*, Photodiagnosis and Photodynamic Therapy, 32, 2020.

[9]. Collman J. P., Garner J. M., Woo L. K., *The chemistry of rhenium and tungsten porphyrin complexes in low oxidation states. Synthesis and characterization of rhenium and tungsten porphyrin*

dimers containing metal-metal multiple bonds, Journal of the American Chemical Society, 111 (21), p. 8141-8148, 1989.

[10]. Imahori H., Umeyama T., Kurotobi K., Takano Y., *Self-assembling porphyrins and phthalocyanines for photoinduced charge separation and charge transport*, Chemical Communications, 48(34), p. 4032-4045, 2012.

[11]. Pop S. F., Ion R.-M., Corobea M. C., Raditoiu V., *Spectral and thermal investigations of porphyrin and phthalocyanine nanomaterials*, Journal of Optoelectronics and Advanced Materials, 13(7), p. 906-911, 2011.

[12]. Logunov S. L., Rodgers M. A. J., *Self-assembled ion-pair complexes between porphyrins and bipyridinium species: picosecond dynamics of charge recombination*, The Journal of Physical Chemistry, 96(22), p. 8697-8700, 1992.

[13]. Giovannetti R., *The use of spectrophotometry UV-Vis for the study of porphyrins*, In: Jamal Uddin (Eds.), Macro to Nano Spectroscopy, p. 87-108, 2012.

[14]. Pratiwi R., Ibrahim S., Tjahjono D. H., *Reactivity and Stability of Metalloporphyrin Complex Formation: DFT and Experimental Study*, Molecules, 25, p. 4221-4228, 2020.

[15]. Olteanu L., Ion R. M., Teodorescu S., Ştirbescu R. M., Dulamă I. D., Bucurică A. I., *New metallo-porphyrins for solar energy conversion*, Bulletin of the Transilvania University of Brasov, 10 (59), Series I, p. 47-54, 2017.

[16]. Aydin M., Akins D. L., *Infrared and Raman Spectroscopic Characterization of Porphyrin and its Derivatives*, In: Applications of Molecular Spectroscopy to Current Research in the Chemical and Biological Sciences, IntechOpen, 2016.

[17]. Georgescu R., Boscornea C., Calinescu I., State R., *Raman IR and UV-Vis Spectroscopic Investigations of Some Substituted Phthalocyanines*, Revista de Chimie (Journal of Chemistry), 66(10) p. 1554-1560, 2015.

MANUSCRISELE, CĂRŢILE ŞI REVISTELE PENTRU SCHIMB, PRECUM ŞI ORICE CORESPONDENŢE SE VOR TRIMITE PE ADRESA:

MANUSCRIPTS, REVIEWS AND BOOKS FOR EXCHANGE COOPERATION, AS WELL AS ANY CORRESPONDANCE WILL BE MAILED TO:

LES MANUSCRIPTS, LES REVUES ET LES LIVRES POUR L'ECHANGE, TOUT AUSSI QUE LA CORRESPONDANCE SERONT ENVOYES A L'ADRESSE:

MANUSCKRIPTEN, ZIETSCHRITFTEN UND BUCHER FUR AUSTAUCH SOWIE DIE KORRESPONDENZ SID AN FOLGENDE ANSCHRIFT ZU SEDEN:

After the latest evaluation of the journals by the National Center for Science Policy and Scientometrics (**CENAPOSS**), in recognition of its quality and impact at national level, the journal will be included in the B^+ category, 215 code (http://cncsis.gov.ro/userfiles/file/CENAPOSS/Bplus_2011.pdf).

The journal is already indexed in:

DOAJ: https://doaj.org/

SCIPIO-RO: http://www.scipio.ro/web/182206

EBSCO: http://www.ebscohost.com/titleLists/a9h-journals.pdf

Google Academic: https://scholar.google.ro

Index Copernicus: https://journals.indexcopernicus.com

Crossref: https://search.crossref.org/

The papers published in this journal can be viewed on the website: http://www.gup.ugal.ro/ugaljournals/index.php/mms

Name and Address of Publisher:
Contact person: Elena MEREUȚĂ
Galati University Press - GUP
47 Domneasca St., 800008 - Galati, Romania
Phone: +40 336 130139
Fax: +40 236 461353
Email: gup@ugal.ro

Name and Address of Editor:
Prof. Dr. Eng. Marian BORDEI
"Dunarea de Jos" University of Galati, Faculty of Engineering
111 Domneasca St., 800201 - Galati, Romania
Phone: +40 336 130208
Phone/Fax: +40 336 130283
Email: mbordei@ugal.ro

AFFILIATED WITH:

- THE ROMANIAN SOCIETY FOR METALLURGY
- THE ROMANIAN SOCIETY FOR CHEMISTRY
- THE ROMANIAN SOCIETY FOR BIOMATERIALS
- THE ROMANIAN TECHNICAL FOUNDRY SOCIETY
- THE MATERIALS INFORMATION SOCIETY (ASM INTERNATIONAL)

Edited under the care of the FACULTY OF ENGINEERING

Annual subscription (4 issues per year)

Fascicle DOI: https://doi.org/10.35219/mms

Volume DOI: https://doi.org/10.35219/mms.2021.1

Editing date: 15.03.2021
Number of issues: 200
Printed by Galati University Press (accredited by CNCSIS)
47 Domneasca Street, 800008, Galati, Romania